
Scanning near-field optical microscopy: from single-tip to dual-tip operation

Angela E. Klein

Jena 2014

Scanning near-field optical microscopy: from single-tip to dual-tip operation

Dissertation
zur Erlangung des akademischen Grades
doctor rerum naturalium (Dr. rer. nat.)

vorgelegt dem Rat der Physikalisch-Astronomischen Fakultät
der Friedrich-Schiller-Universität Jena

von Dipl. Phys. Angela E. Klein
geboren am 26.02.1984 in St. Wendel

Gutachter:

1. Prof. Dr. Thomas Pertsch, Friedrich-Schiller-Universität Jena
2. Prof. Dr. Bert Hecht, Julius-Maximilians-Universität Würzburg
3. Prof. Dr. Olivier Martin, École Polytechnique Fédérale de Lausanne, Schweiz

Tag der Disputation: 27.01.2015

Contents

1	Introduction	1
2	Aperture SNOM	8
2.1	Introduction to aperture SNOM	8
2.2	Experimental setup for aperture SNOM measurements	11
2.3	Far-field characterization of aperture tips	14
2.4	Near-field emission of aperture tips observed with a circular grating	19
3	Scanning thermocouple-probe microscopy	22
3.1	Measurement principle and setup	22
3.2	Temporal resolution	25
4	Instrumentation for Dual-SNOM	27
4.1	Dual-SNOM setups	29
4.2	Distance control	32
4.2.1	Theoretical model	33
4.2.2	Mechanical interaction in the “parallel” Dual-SNOM configuration	35
4.2.3	Mechanical interaction in the “mixed” configuration	37
4.3	Optical emission and detection characteristics	40
5	SNOM mapping of Airy plasmons	49
5.1	Generation and near-field mapping of Airy plasmons	52
5.2	Interference of Airy plasmons: plasmonic hot-spots	57
6	Mapping whispering-gallery modes in fused silica microresonators	61
6.1	Introduction	61
6.2	Collection-mode SNOM	62
6.3	Scattering-based SNOM	65
6.4	Thermal SPM	67
6.4.1	Measurements	67
6.4.2	Simulations	70

7	Characterization of plasmonic waveguides by Dual-SNOM	74
7.1	Observation of leaky modes in gold strip waveguides	74
7.2	Investigation of the excitation process	79
8	Summary and Outlook	85
A	Zusammenfassung	89
B	Lebenslauf	92
C	Publications	94
D	Acknowledgements	98
E	Ehrenwörtliche Erklärung	100

Chapter 1

Introduction

Sight is the most important human sense and dominates our perception of the world. Correspondingly, the nature of light and colors and the process of seeing have been the subjects of uncountable theories, speculations and investigations since ancient times. After craftsmen developed methods to machine and grind transparent materials, like rock crystal, beryl and glass, first lenses were produced. By using lenses as magnifying glasses, the human vision could be enhanced, thereby enabling machining and investigation of fine structures, like engravings and seals[1–4]. In the modern era, the combination of several precisely fabricated lenses into microscopes permitted to observe structures on the micrometer scale, which paved the way for entirely new research fields - like cell biology, microbiology and optical mineralogy - and vastly contributed to today's scientific view of the world[5–8].

Until recently, the sizes, length-scales and periodicities of man-made structures have, with very few exceptions, been much larger than the wavelengths of visible light (400 nm to 700 nm). The interaction of light with such structures can essentially be described by ray optics. Chemical bond lengths and periodicities of natural crystalline materials, on the other hand, lie in the ångström (0.1 nm) range and are thus much smaller than the wavelengths of visible light. The structure of such materials cannot be resolved by light, and their optical properties can be described by averaged material properties, like the refractive index.

Advanced fabrication technologies, which were developed primarily for microelectronics, have now made it possible to fabricate structures with feature sizes and periodicities in the sub-micrometre range. The interaction of light with artificial structures which are as small as the light wavelength or even smaller gives rise to a multitude of fascinating effects which were not accessible without micro- and nano-structuring.

As metals feature quasi-free electrons which move freely within the volume of the metallic body, they have unique optical properties which show, e.g., in the typical metallic luster. In small metallic particles and structures, the electron gas is spatially confined, which limits the movement of electrons and gives rise to plasmonic resonances[9]. By assembling many subwavelength building blocks, it is possible to create artificial materials – metamaterials – with novel, tailored optical properties such as negative refraction[10–13].

In plasmonic circuits, light can be concentrated and guided within small volumes, which could make them valuable tools for optical information processing in miniature optical circuits[14–18]. In solar cells, nanostructures can increase the efficiency by trapping photons[19]. To understand and investigate all these phenomena, high-resolution microscopy is needed which allows one to study the electromagnetic fields on subwavelength scales.

In conventional far-field microscopy, an objective is used to collect light which is emitted or scattered by the sample under investigation. The objective’s numerical aperture (NA) specifies the opening angle of the objective’s collection cone. This angular range determines the range of k -vectors which eventually contributes to the image, and this determines the microscope’s resolving power, as it is expressed in the Abbe diffraction limit[20].

Features which are less than approximately half a wavelength apart can therefore not be distinguished by far-field microscopes. This can be understood in terms of the corresponding k -spectrum: The transverse component of the wavevector of propagating waves is limited by the wavenumber. Only evanescent waves, with complex propagation constants, can have larger transverse wavenumbers, which represent higher spatial frequencies associated with small features. Importantly, though the diffraction limit prohibits the distinction of two closely spaced objects, the position of a single object, e.g., a point-like light source, can in principle be determined to any desired precision.

A number of microscopy techniques have been developed to circumvent the Abbe diffraction limit. Especially in biology, it is often the spatial distribution of fluorescing molecules in a stained sample which one wants to uncover. Some super-resolution microscopy techniques specifically address this issue and are based on distinct properties of fluorescent dyes.

Super-resolution microscopy techniques can be divided into two main categories, based on the strategy which is used to circumvent the Abbe limit:

In structured illumination microscopy (SIM)[21–23], the sample is illuminated by a series of sinusoidal stripe patterns with different orientations and lateral shifts. In analogy to the Moiré effect, this shifts the spatial frequencies of the sample along the k -vector of

the stripe pattern. For each pattern orientation, some high spatial frequency response of the sample is thereby shifted to lower frequencies, i.e., smaller transverse wavenumbers, which can be detected by the microscope. The interference patterns recorded for different orientations and shifts of the stripe pattern are processed in Fourier space to eventually obtain an image of the sample with increased resolution.

In contrast to SIM, which is based on a systematic extension of the accessible k -space, other super-resolution microscopy methods circumvent the Abbe limit by serialization. It is not possible to distinguish two sample features - e.g., fluorescent molecules - which are less than half a wavelength apart by collecting and processing their emission in the far-field. However, a number of techniques have been developed to distinguish optical signals of such closely spaced features by not looking at both of them at the same time. This asynchronous observation of closely-spaced features can either be implemented by systematically scanning the sample with a sub-wavelength light source or a sub-wavelength light collector, or by exploiting the randomized blinking of light emitters.

In photoactivated localization microscopy (PALM)[24], a low power activation laser is used to activate only a small percentage of fluorescent dye molecules in the sample. These activated molecules emit photons for a limited time before they return to their dark state or photobleaching occurs. A standard microscope with a camera is used to capture highly resolved images in which each activated molecule appears as a circular spot, determined by the microscope's point spread function. By fitting a gaussian shape to each spot, the centroids of the spots and therefore, the positions of the fluorescing molecules can be determined with high accuracy. By repeating this procedure for many sets of molecules, the distribution of dye molecules can be accurately mapped. Stochastic optical reconstruction microscopy (STORM)[25] and fluorescence photoactivation localization microscopy (FPALM)[26] have been synchronously developed and rely on a similar principle as PALM.

Another prominent super-resolution microscopy technique which utilizes the properties of fluorescent dyes is stimulated emission depletion (STED) microscopy[27]. Here, a laser spot is focused onto the sample to selectively activate fluorescent molecules. A second, ring-shaped laser spot at a red-shifted wavelength serves to deplete most activated molecules by stimulated emission, so that only the molecules in a small central spot remain active. This small spot is scanned over the surface to obtain an image.

All these super-resolution microscopy techniques rely on fluorescent dyes and/or specific illumination conditions. The techniques are therefore well suited for biology, where staining is

routinely used to highlight structures and to enhance contrast in images. When investigating materials, technical objects or fundamental excitations, label-free techniques are necessary. To investigate light-matter interaction on subwavelength scales, or to observe optical phenomena involving evanescent waves, we need to probe the optical near-fields of samples, i.e., they have to be converted to observable signals in the immediate vicinity of the sample surface.

Scanning near-field optical microscopy[28–34] (SNOM, sometimes also called NSOM, for near-field scanning optical microscopy) implements this concept by using a sharp tip which is brought into the sample’s near field zone and which scatters light from the near-field into radiation fields in free space or into fiber modes. Images are obtained by scanning this tip across the sample surface and assembling the detected signals into 2-dimensional maps. By SNOM, optical phenomena on sample surfaces can be observed with high resolution, within a large spectral range.¹ No modification of the sample surface, e.g., by fluorescent dyes, is necessary. As typically no dyes are involved, bleaching or uneven distribution of dye molecules can’t occur. The illumination conditions can be chosen almost arbitrarily. The collected light can be further analyzed for its spectral[36] and polarization[37, 38] properties, or phase measurements can be realized by an inteferometric setup[39–41]. By using a series of short pulses for illumination, even time-resolved SNOM measurements have been reported[39, 42–44].

Like in scanning tunneling microscopy[45] and atomic force microscopy[46], the tip of a SNOM is scanned along the sample surface at very close distance with the help of piezo actuators, which permit precise positioning of the tip and thus make highly resolved surface mapping possible. The distance between the tip and the sample is controlled by a feedback mechanism which keeps the forces between the oscillating tip and the sample constant, thus making the tip follow the sample topography. Some SNOM setups employ the same feedback mechanism as atomic force microscopes, i.e., the deflection of a microscopic silicon cantilever is detected via a laser which is reflected off the back of the cantilever onto a position-sensitive detector. In fiber SNOM, it is more common to attach the tip to a piezoelectric tuning fork whose oscillation properties are influenced by forces between the tip and the sample.

Already in 1928, Synge suggested a new type of microscope with increased optical resolution[47], based on an opaque film with a subwavelength hole which is placed on

¹In fiber SNOM, the spectral range is only limited by the availability of suitable light sources, detectors and optical fibers. In scattering SNOM, no fibers are used, and measurements in the THz and microwave regimes are possible[35].

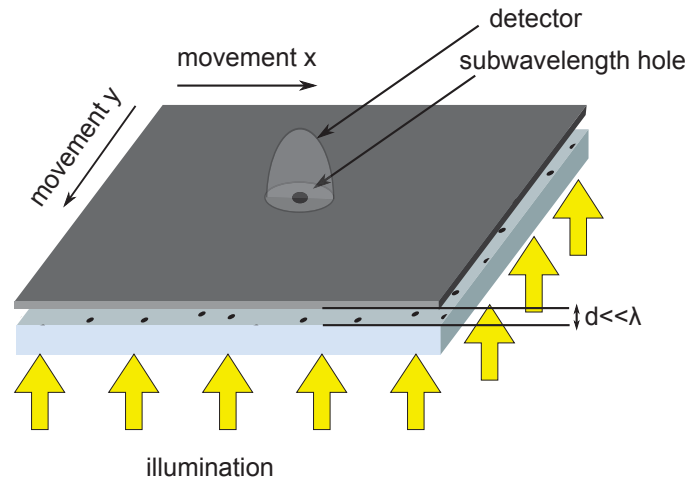


Figure 1.1: Schematic representation of Syngé's idea (1928) of a device capable of recording optical images with a resolution better than the diffraction limit: A thin, opaque screen with a subwavelength hole is scanned over the sample at a distance much smaller than the light wavelength. Either a detector is placed behind the hole, or the sample is illuminated through the hole (not shown).

a sample so that the hole is less than 10 nm away from the sample surface. The hole could then either be illuminated and act as a highly localized light source, or it could be positioned between the illuminated sample and a detector, so that only light from the small area below the hole could reach the detector (see Fig. 1.1). In 1944, Bethe developed a theoretical model for diffraction through such small holes in perfectly conducting metal films[48], which was later refined by Bouwkamp[49]. Due to technological limitations, the concept was not experimentally implemented until 1972[50], when scanning near-field optical microscopy with a resolution of $\lambda/60$ was demonstrated in the microwave regime. In the optical frequency range, scanning near-field microscopy was independently developed by two groups in the mid-1980s. In their pioneering experiments, Pohl et al.[51] used a metal-coated crystalline quartz tip with an aperture formed by carefully pushing the tip onto a flat sample. Lewis et al.[52] performed some pre-studies on light transmission through lithographically formed apertures in planar metal films and later used aperture tips in their application-oriented experiments[53]. These aperture tips were fabricated by first melting and pulling a glass pipette until it broke apart and then covering the hollow tip with metal. Today, most probes used in aperture SNOM are either fiber probes (see Chapter 2) or hollow-pyramid probes.

A hollow-pyramid SNOM probe has the shape of an inverted pyramid with a subwave-

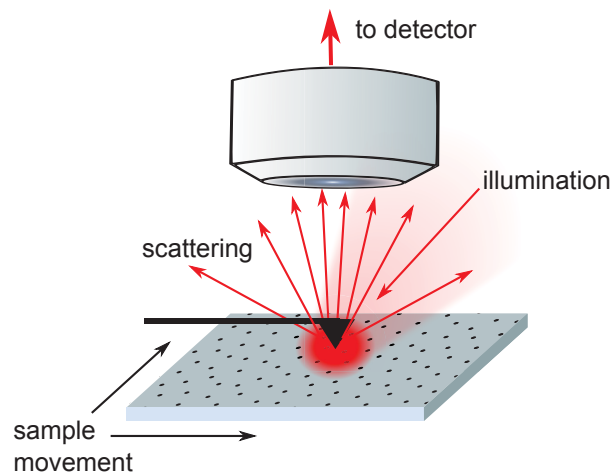


Figure 1.2: Schematic representation of scattering SNOM: The sample is illuminated from the far-field. A sharp scanning probe microscope tip is scanned over the surface and scatters light from the sample towards a collection objective.

length aperture at the apex, which is either fabricated from a dielectric material with a metal coating[54, 55], or as a metallic hollow pyramid[56–59]. The aperture is placed in the focus of a microscope objective (above the tip) for collection or illumination.

Apart from aperture tips, other SNOM techniques have been established: In scattering SNOM[60–65] (or s-SNOM), a sharp, oscillating tip is used to scatter light from a small volume defined by the tip’s position on the sample surface (see Fig. 1.2). The tip can simultaneously act as an antenna and concentrate light in this volume[66–68]. The sample is illuminated by a focused laser beam, and the scattered light is collected by an objective. To discriminate the actual signal, which originates from scattering of the sample’s near-field by the tip, from the large background of light scattered by the sample or the tip itself, the intensity signal is demodulated by lock-in techniques. As the evanescent fields decay exponentially away from the surface, the scattering signal created by the sinusoidally oscillating tip is strongly modulated at higher harmonics of the oscillation frequency, so that demodulation at such higher harmonics can be used to discriminate between the near-field signal and the background.

Besides these rather well-established methods there are some alternative methods which bear particular advantages. Tips which contain localized light sources at the apex are used to locally illuminate the sample, e.g., by using fluorescent dyes[69–71] or color centers[72, 73], or by exploiting the luminescence of a gold nanotip[74]. Potentially, sharp, fully metalized fiber tips could be used as efficient and ultra-small near-field light sources. If a radially

polarized fiber mode is excited in such a tip, a conical surface plasmon polariton (SPP) mode can be excited on the outer surface of the coating by resonant coupling between the fiber mode and the SPP mode[75–80]. The conical geometry then leads to superfocusing of the SPP, which results in field enhancement at the tip apex[75, 80–86]. This concept promises a very advantageous SNOM tip with high resolution, high throughput and background-free illumination. So far, technical difficulties, especially in guiding a radially polarized mode within the taper, have prevented its application in SNOM measurements.

The aim of this thesis was to integrate two SNOMs into a Dual-SNOM which permits simultaneous near-field excitation and near-field detection, to study the image formation in SNOM and Dual-SNOM, and to apply these techniques for the near-field characterization of optical micro- and nanostructures. This thesis is structured as follows: While Chapters 1-4 are mainly concerned with basic concepts and instrumentation aspects of the different single- and dual-tip scanning probe microscopy techniques used in this thesis, Chapters 5-7 present application examples of these techniques. In Chapter 2, a general introduction to aperture SNOM is given. The specific setups used throughout this thesis are presented, and two methods to characterize the aperture tips in terms of their polarization properties are discussed. In Chapter 3, an alternative method for mapping optical near-fields is presented, where the aperture tip connected to an optical detector is replaced by a micro-thermocouple probe which is heated by optical absorption and thus converts the optical signal into an electrical signal directly at the measurement location. In Chapter 4, instrumentation aspects of the integration of two aperture SNOMs into a Dual-SNOM setup are discussed. This chapter also includes a set of Dual-SNOM measurements, the near-field mapping of plasmonic aperture emission. These measurements allow inference on the convolved emission and collection properties of both tips and therefore, on the instrument's optical properties and on image formation in SNOM and Dual-SNOM measurements. In Chapter 5, as an application example of aperture SNOM, near-field mapping of plasmonic Airy beams and of plasmonic hot-spots generated by interference of two plasmonic Airy beams is demonstrated. In Chapter 6, scanning thermocouple-probe microscopy is applied to map whispering-gallery modes in dielectric microresonators. This study is complemented by two additional methods to map whispering-gallery modes, namely aperture SNOM and a tailored scattering technique. In Chapter 7, Dual-SNOM measurements on plasmonic stripe waveguides are presented. The excitation of different waveguide modes as a function of the excitation tip's position and the near-field mapping of the resulting beating patterns showcase the unique characterization possibilities of Dual-SNOM.

Chapter 2

Aperture SNOM

2.1 Introduction to aperture SNOM

This thesis is mainly focused on fiber-based aperture SNOM. The utilized fiber tips are produced by tapering optical fibers and subsequently coating them with metal. By evaporating the metal at a defined angle and rotating the tip during evaporation, a round aperture is formed at the apex. Uncoated fiber tips are used in SNOM as well, but depending on the illumination conditions, lateral coupling of light from the free space into the fiber taper can deteriorate the contrast, and their optical resolution is lower than that of metal-coated tips[87].

By coupling the end of the optical fiber to a laser source (illumination mode) or to a detector (collection mode), fiber tips can be used either as subwavelength light sources or as near-field light collectors. Scattering processes at the aperture lead to coupling between the fiber modes and the modes of the sample via the near-fields of the sample and the aperture. By introducing a beam splitter, the tip can also be used as a light source and collector at once[88, 89]. This operation mode is called illumination collection mode or sometimes reflection mode. An overview of SNOM operation modes is given in Fig. 2.1 and in Ref. 90. In all operation modes except illumination collection mode, microscope objectives are commonly used to either illuminate the sample (in collection mode) or to collect light from the sample (in illumination mode).

Regardless of the specific operation mode in which a fiber SNOM is used, it is not straightforward to interpret the obtained images. Let us consider image formation in an illumination-mode SNOM. Here, the measurement can in principle be regarded as a four-step process:

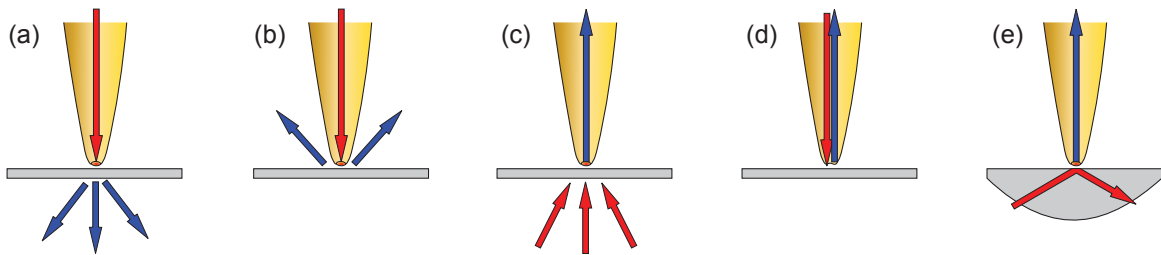


Figure 2.1: Some of the most common operation modes of aperture SNOM: (a) transmission illumination mode (b) reflection illumination mode (c) transmission collection mode (d) illumination-collection mode (e) photon scanning tunneling microscopy (PSTM) with total internal reflection illumination.

1. light propagates through the tapered, metal-coated fiber towards the aperture,
2. the aperture diffracts and scatters light,
3. modes in the sample are excited via the tip's near-field,
4. light emanating from the sample is detected in the far-field, usually via a microscope objective.

The image formation in collection-mode is not fundamentally different[91, 92], i.e., findings and considerations on illumination mode can often be transferred to collection mode and vice versa.

Importantly, this four-step model doesn't account for the tip-sample interaction, i.e., for the fact that the metal-coated aperture tip constitutes a rather large object within the sample's near-field region, which leads to field modifications and damping. An accurate model has to take into account both the tip and the sample as a coupled system[29, 93]. Numerically, this is often hard to realize because of the diverse length scales and refractive indices in typical experimental configurations, and the position of the tip with respect to the sample is different for each image pixel. Also, one should keep in mind the most prominent sources of artefacts in aperture SNOM images, faulty tips[94] and topographical artefacts[95–98]. Topographical artefacts arise as the exact path of the aperture influences the optical image, which constitutes a mixture of optical and topographic information. For the studies presented in Chapters 5 and 6, topographic artefacts are only marginally important because the samples had mostly flat surfaces.

While the fourth step in the simplified model (far-field detection of light emanating from the sample) is highly dependent on the specific experimental configuration, each of the

other three steps, as well as possible artefacts, remain the subject of extensive theoretical and experimental research[38, 99–106].

When light propagates from the unperturbed optical fiber towards the tip, the propagation constant of each waveguide mode changes within the metalized, tapered region. As the taper diameter decreases, the modes eventually become evanescent[103, 107]. This cutoff happens at different taper diameters for the different modes. The fundamental mode HE_{11} is the last mode to run into cutoff, so that it is generally the only relevant mode carrying information to (or from) the aperture’s near-field[103, 108, 109].

The aperture diffracts light, constituting a source of evanescent as well as propagating waves. A multitude of methods have been employed to model this process[48, 49, 110–113]. The methods start from Bethe and Bouwkamp’s analytical model of diffraction by a circular aperture in an infinitely thin, perfectly conducting metal screen[48, 49], and range to large finite-difference time-domain (FDTD) simulations of SNOM tips[103, 113]. Generally, diffraction by the aperture can change the polarization state of transmitted light[114]. The exact shape of the aperture can significantly influence the tip’s near-fields, and a variety of optimized aperture shapes have been proposed to control the polarization of emitted light, to increase the transmission or to improve the resolution[115, 116]. Such specially designed tips are often fabricated by focused ion beam (FIB) milling. Apertures in the form of split-rings[41], “short-cut double C-shaped” apertures[117], elliptical apertures[118], bowtie-shaped apertures[119, 120] and even “campanile”-shaped apertures[121] with very high transmission have been developed, to mention a few. While these tip designs can enhance the transmission significantly, they require elaborate and time-consuming structuring of the individual tips.

The polarization properties of the tips also influence the coupling between the tip modes and the sample modes, which is related to the question which components of the electromagnetic fields contribute to a (collection mode) SNOM image, or, in other words, the coupling to sample modes. There is some consensus that typical aperture SNOM tips with circular, subwavelength apertures probe only the vector components of the electromagnetic field which are transverse to the tip axis, i.e., parallel to the aperture plane[38, 41, 101]. In contrast, bare fiber tips[122], scattering tips[123–125], split-ring type aperture tips[41, 126] and tips with apertures measuring approximately a full wavelength in diameter[103] can probe longitudinal field components as well. The relative contributions of electric and magnetic field components are still actively discussed[38, 41, 100, 101, 108, 127]. Recent theoretical results suggest that the impedance of the fundamental guided mode in

the tip determines the ratio between the contributions of the electric and the magnetic field[108, 128]. In illumination SNOM, the image can be related to the (partial) local density of states (LDOS)¹ of the sample[129–131].

In this thesis, aperture SNOM is used to map Airy plasmons (Chapter 5) and whispering-gallery modes in fused silica microresonators (Chapter 6.2). Selected aspects of image formation are covered in Chapters 2 (this chapter), 4 and 7: In Chapters 2.3 and 2.4, the far-field polarizations of light emitted by bent fiber SNOM tips, as well as their coupling to SPPs on a gold film, are studied. When mapping the surface plasmon polaritons (SPPs) excited by a first SNOM tip with a second tip in a Dual-SNOM setup (Chapter 4.3), both the excitation and detection characteristics of the tips come into play. The inherent polarization characteristics of the tips are shown to play an important role in image formation. The relation between the excitation tip’s position and mode excitation in a sample is studied in Chapter 7, where a Dual-SNOM setup is used to excite and map plasmonic modes in gold strip waveguides.

2.2 Experimental setup for aperture SNOM measurements

In our measurements, we used commercial fiber tips (Nanonics Imaging Ltd.) manufactured by heating and pulling an optical fiber and subsequently coating the taper by a few nanometer thin chromium adhesion layer. On top of the adhesion layer, a 200 nm to 300 nm thick gold layer is evaporated, leaving a round aperture at the tip apex. A commercial SNOM head (MV-4000, Nanonics Imaging Ltd.) serves to scan the tip over the sample surface by piezo scanners while maintaining a mean tip-sample distance of a few tens of nanometers. This is achieved by attaching the tip to a resonantly oscillating quartz tuning fork[132–134]. The oscillation frequency is usually chosen so that the tuning fork’s first mechanical eigenmode is excited, which corresponds to a frequency in the range of 32 kHz to 45 kHz. The tip features a 60° bend within the tapered region, so that the fiber runs horizontal and the tip itself is tilted by 30° with respect to the vertical axis. As the tuning fork oscillates, the tip performs a tapping motion (see Fig. 2.2). Interaction forces between the tip and the sample surface affect the amplitude and phase of the tuning fork’s oscillation. A feedback loop keeps the oscillation phase constant by regulating the tip’s vertical position while the tip is scanned over the surface. In this way, the mechanical

¹Each partial LDOS corresponds to a specific orientation of a dipolar emitter.

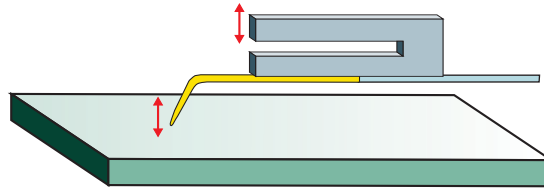


Figure 2.2: Sketch of a bent, metalized aperture SNOM tip attached to a tuning fork. Due to the tuning fork's oscillation, the tip performs a tapping motion used for controlling the tip-sample distance with a feedback-loop.

tip-sample interaction is kept constant and the tip follows the sample topography. The piezo scanner of the MV-4000 SNOM head has open-loop position control and scanning. In addition to the piezo scanners, which provide scanning within a cube of around $(30\ \mu\text{m})^3$, three stepper motors allow for coarse positioning of the tip.

The flat piezo scanner, the tuning fork and the tip form a cantilever arm which extends sideways from a cylindrical tower containing amplifying electronics and the stepper motors (see the photo in Fig. 4.2 and the schematic drawings in Fig. 4.1). The cantilever design permits optical access from above and the integration of several SNOM heads into a multi-probe setup. At the same time, the system is prone to undesired vibrations originating from air movement or vibrations of the table. In order to reduce the influence of solid-bound vibrations, the whole setup was assembled on an active vibration isolation table. A foam-lined cubicle serves to isolate the setup from air movement.

The sample can be laterally scanned by an xy piezo stage (PI 542.2) with a travel range of $200\ \mu\text{m} \times 200\ \mu\text{m}$ and closed-loop position control with sub-nanometer resolution. Additionally, the sample can be coarse-positioned by a custom-made stage based on piezo slip-stick positioners (Smaract SL-17).

The SNOM head and sample stage are mounted on an inverted optical microscope (Zeiss AxioObserver.D1) with the help of a custom-made aluminum adapter plate (fabricated in the department's mechanical workshop). With this adapter plate, two SNOM heads can be used at the same time. The adapter plate permits different configurations. Such Dual-SNOM configurations and experiments are described in Chapter 4. The possibility to simultaneously excite and detect light in the near-field opens up exciting new possibilities for the optical characterization of various samples, as the emission of the excitation tip and the excited sample modes can be directly observed.

In the experimental setup, a second optical microscope (Zeiss AxioScope.A1) provides optical access from above. It can be translated along x , y and z via manual translation

stages. Both optical far-field microscopes are equipped with CCD cameras and with white-light illumination. Additional optical ports are available for light incoupling, cameras or detectors. Several studies described in this thesis use the SNOM in collection mode. In this configuration, the sample is illuminated either via a microscope objective from below (Chapter 5), or via the evanescent fields of a tapered fiber loop (Chapter 6). The fiber tip serves to collect light and guide it to a sensitive detector, which in turn is connected to the SNOM controller. The intensity signals of the individual pixels are assembled into 2D “SNOM” images via the scanning probe microscopy (SPM) software.

We observed that tips fabricated from multi-mode (MM) fiber (Newport F-MSD, core diameter: $50\ \mu\text{m}$, $\text{NA}=0.2$) had a considerably higher collection efficiency than those fabricated from single-mode (SM) fiber (Newport F-SV, $\text{NA}=0.1$ to 0.14). We suppose that this difference in collection efficiency is due to the different coupling in the transition region where the core becomes so thin that the guided modes are not confined to the core, but the fields extend far into the cladding and even into the metal coating, within the conical part of the tip. In the transition region between the single-mode fiber with its well-defined core and quasi-lossless guiding properties, and the taper where the core is thinned and/or mixed with the cladding, some of the light which has been collected through the aperture couples to higher-order fiber modes. Those are not guided by the fiber core and eventually radiate out of the fiber. Only the light coupled to the fundamental fiber mode reaches the detector. In the MM fiber, as it supports a large quantity of guided modes and has a large acceptance angle (expressed by the NA), the overlap of the incident field with the modes which are guided to the detector is larger. Furthermore, the larger refractive index contrast between core and cladding, which can also be deduced from the NA, may lead to reduced bending loss in the metalized, tapered bend. We estimate that these factors lead to dramatically reduced loss. To illustrate the different structure of both fiber types, Fig. 2.3 shows schematic representations of both types of SNOM tips.

Generally, the exact relation between the detected intensities and the vectorial electromagnetic field at the aperture’s position is not trivial and has to be known prior to interpreting SNOM images. In this chapter, we present studies on the collection and emission properties of the tips in our experimental configuration, which predefine the imaging properties of the setup.

A perfectly rotationally symmetric aperture tip, positioned perpendicular to the sample surface, is expected to collect in-plane components of the electric and magnetic field without any orientation bias. If additionally the polarization is preserved in the fiber, polarization-

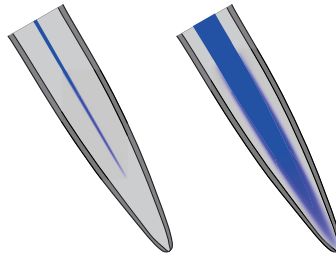


Figure 2.3: Schematic representation of the inner structure of aperture SNOM tips, fabricated from single-mode fiber (left) and from multi-mode fiber (right) by heating and pulling the fiber. The longitudinal section shows the fiber core (dark blue), the cladding (bright grey) and the metal coating (dark grey).

resolved SNOM measurements[38, 135] are possible. For such measurements, however, uncoated fiber tips[37, 136–138] or highly polarization-sensitive, asymmetric aperture designs which transmit only a single polarization direction[117, 118, 139, 140] are preferably used. Nevertheless, even without employing a special tip design, polarization-sensitivity can occur as soon as the symmetry is broken, e.g., by an asymmetric aperture or, as it is the case in our measurements, if the tip is tilted with respect to the surface normal and there is a bend in the tapered region of the fiber. As this symmetry breaking could lead to polarization-sensitive detection properties, we experimentally characterized the polarization characteristics of cantilevered SNOM tips[141].

2.3 Far-field characterization of aperture tips

In order to quantify the polarization sensitivity of tips in collection mode, we used a diode laser with a free-space wavelength of $\lambda_0 = 663 \text{ nm}$ to illuminate the cantilevered aperture tips from below. The experimental setup is shown in Fig. 2.4(a). The expanded, collimated laser beam first passed a half-wave plate and was then focused by a 20x-objective (NA=0.22) of the inverted microscope. The fiber tip, mounted in a SNOM head, was placed with the apex on the microscope’s optical axis and a few tens of μm above the focal plane to guarantee a homogeneous illumination of the aperture plane. The collection signal was measured by a fiber coupled avalanche photo diode (Perkin Elmer SPCM-AQR). By rotating the polarization direction ϕ of the laser beam in steps of 10° and recording the corresponding collection signal, the polarization-resolved collection efficiency of the tip was determined. Fig. 2.4(b) shows the result of a typical measurement. The two-lobe pattern indicates that the collection efficiency is indeed polarization-dependent.

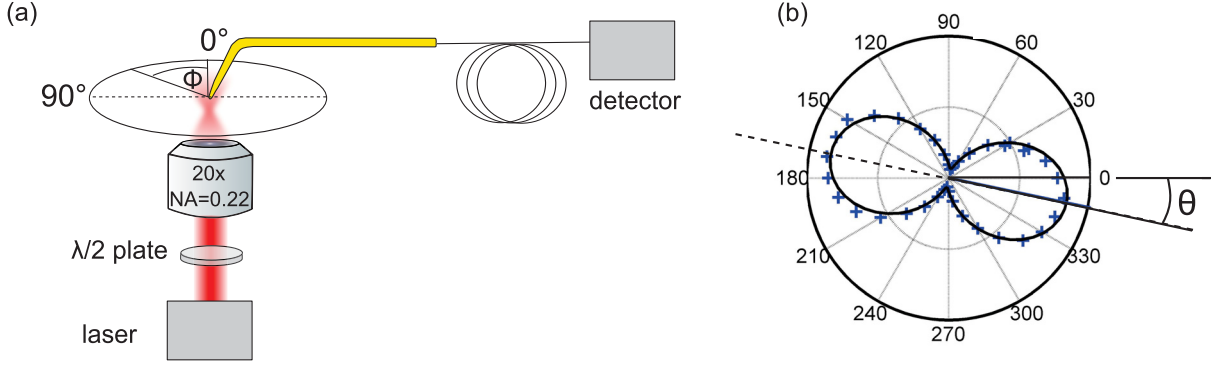


Figure 2.4: (a) Schematic drawing of the experimental setup used to measure the polarization sensitivity of aperture SNOM tips. A laser beam passes a half-wavelength plate and is then focused by a microscope objective. The tip is positioned above the laser focus. The polarization direction ϕ of the beam is rotated stepwise, and the collected light intensity is recorded by a detector. (b) Polar plot of the measured intensities (blue crosses) and the fitted curve according to equation (2.1), for a particularly polarization-sensitive tip, which was later used in near-field experiments. The angle θ denotes the polarization direction of light which is collected most efficiently by the tip.

We denote the polarization direction of light which is collected most efficiently with θ . The electrical field of the illuminating light can be decomposed into the components E_a , along θ , and E_b , orthogonal to θ . The collected signal is then given by

$$I(\phi) = a \cos^2(\phi - \theta) + b \sin^2(\phi - \theta), \quad (2.1)$$

where a and b are positive, real numbers and stand for the maximum and minimum collection efficiency, multiplied by the illumination intensity, respectively. Formula 2.1 is valid as long as no significant polarization mixing occurs within the tip or the fiber, which could lead to interference between components of the field which were originally orthogonally polarized.

We fitted expression (2.1) to the measured values (corrected for the detector's dark count) in order to obtain a , b and θ for each tip [see the drawn-out black line in Fig. 2.4(b)]. In analogy to the definition of the degree of polarization,[142] we define the polarization sensitivity $Q_c = \frac{a-b}{a+b}$, which can take values between 0 (polarization-insensitive collection efficiency) and 1 (detection of a single polarization component, complete suppression of the other). We determined the polarization sensitivities Q_c and the polarization directions θ (which are most efficiently collected) for 14 tips, 7 of which were fabricated from SM fiber and 7 from MM fiber. Figure 2.5(a) shows a plot of θ and Q_c obtained from the fitting

procedure, along with the 95% confidence bounds of the fit. Each tip is represented by a data point. The polarization sensitivities Q_c lie between 0.33 and 0.86, which translates to extinction ratios ($b : a$) between 1:2 and 1:13.

It is striking that with the exception of a single SM fiber tip, the SM tips feature higher polarization sensitivities Q_c than the MM tips. This becomes evident in the histogram of the polarization sensitivities in Fig. 2.5(c), to the right of the scatter plot. The red bars representing the number of MM tips are stacked to the right of the blue bars representing the number of SM tips, so the total length of the bars corresponds to the total number of tips/data points in each bin. The mean values of Q_c , calculated separately for SM fiber based tips and MM fiber based tips, are plotted in Fig. 2.5(d), along with their statistical standard deviations (error bars). The mean polarization sensitivity of the 7 SM fiber based tips is 0.7, whereas the 7 MM fiber based tips have a mean polarization sensitivity of only 0.4. In terms of the angles θ , no differences between SM tips and MM tips are evident. For both types of fiber, angles θ spanning the complete range between -90° and 90° occur. However, independently of the fiber type, a clustering of counts around 0° (center) and $\pm 90^\circ$ (edges of the plot) is found in the stacked histogram of the angles θ in Fig. 2.5(b). This clustering suggests that the polarization directions which are detected most efficiently are not randomly distributed, but that preferred directions exist.

Three possible sources of polarization sensitivity have been identified: (1) asymmetric aperture shapes, (2) the inclination of the aperture with respect to the horizontal plane, and (3) polarization-dependent loss, mode coupling and birefringence induced by the fiber bend. As the apertures of most of the tips used in this study appear symmetric and round in SEM micrographs, we could not ascribe the observed polarization effects to asymmetric aperture shapes, which would constitute an obvious source of a polarization bias in the collection efficiency. Some tips utilized in our study indeed exhibit asymmetric aperture shapes. However, a simple correlation between the aperture shapes and polarization sensitivities of the tips was not observed. To corroborate this claim, micrographs of some tips, along with their positions in the θ/Q_c plot, are shown in Fig. 2.5(e). For some of the tips, the polarization sensitivity has been measured after they had been used for scanning. The micrographs show the tips in the same conditions at which the θ/Q_c measurements were taken. The tip with the most asymmetric aperture is tip h, which exhibits a relatively high polarization sensitivity of 0.77. However, the tip with the highest observed polarization sensitivity, tip f, exhibits an aperture which looks perfectly symmetric in the micrograph. Moreover, the individually different aperture shapes could not explain the clustering of

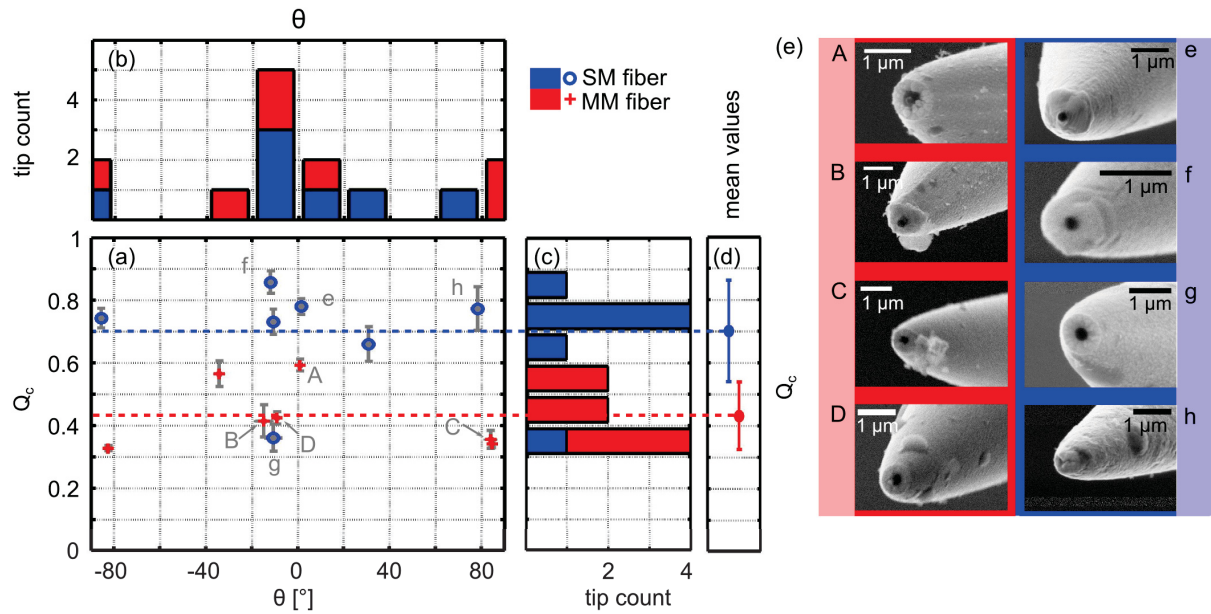


Figure 2.5: Statistical analysis of θ and Q_c values for 14 different aperture SNOM tips. (a) Plot of the polarization directions θ of light which tips detect most efficiently, and Q_c (polarization sensitivity) values. The error bars represent the 95% confidence bounds of the numerical fit. SM fiber tips are represented by blue circles, MM fiber tips by red crosses. The dashed lines represent the mean Q_c values of SM fiber based tips and MM fiber based tips, respectively. (b) Stacked histogram of the angles θ , where the blue and red bars represent SM and MM tips, respectively. (c) Stacked histogram for the polarization sensitivities Q_c . (d) Mean polarization sensitivities for SM and MM tips, and their standard deviations (error bars). (e) Scanning electron micrographs of selected tips and assignment to their respective θ and Q_c values [in panel (a)]. The tips labeled by the upper case letters A-D, shown in the right column, have been fabricated from MM fibers, whereas the tips labeled by the lower case letters e-h have been fabricated from SM fibers.

θ values around 0° and $\pm 90^\circ$. To study the influence of the aperture's inclination, the polarization sensitivities of several tips were measured when the illuminating beam was tilted by $\pm 30^\circ$ with respect to the vertical direction. The measurement results suggest that eliminating the aperture's inclination does not significantly reduce the polarization sensitivity.

Generally, fiber bends can lead to birefringence, bend-induced mode coupling and to polarization-dependent loss[143–146]. It has been shown that either the TE or the TM mode can exhibit stronger loss in a fiber bend, depending on the bend radius[144]. These observations have been made in untapered fibers with large bend radii in the cm range, whereas our tip geometry with a metal-coated, tapered fiber bend (diameter at the bend: approximately $50\ \mu\text{m}$) constitutes a rather extreme case. Still, it is well imaginable that similar effects lead to the observed polarization filtering in the SNOM tips. Moreover, as we can deduce from the fibers' numerical apertures, the refractive index contrast in the MM fibers is higher than in the SM fibers. This could explain why the bend loss, and consequently, the polarization filtering, are less pronounced in MM fiber tips. Polarization-dependent loss in the bend could also explain why the observed preferential directions of 90° and 0° coincide with the characteristic directions of the symmetry break induced by the fiber bend. Therefore, we attribute the observed polarization filtering to polarization-dependent loss introduced by the fiber bend.

For two of the tips, we additionally studied the polarization of light emitted from the apertures into the far-field. The laser beam first passed a half-wavelength plate, which allowed us to turn its polarization, and was then coupled into the fiber with the help of an aspheric lens. The tip apex was imaged onto a detector by the 20x-objective of the lower microscope. An analyser was inserted in the detection path and allowed us to determine the degree of polarization $Q_e = \frac{I_\theta - I_{\theta+90^\circ}}{I_\theta + I_{\theta+90^\circ}}$ of emitted light. Here, θ denotes the main polarization direction of emitted light.

For the first tip, tip f [cf. Fig.2.5(e)], which was fabricated from a SM-fiber, we had previously determined the polarization sensitivity $Q_e=0.86$ and $\theta = -12^\circ$ [see the measurement data in Fig. 2.4(b)]. When analyzing the light emitted by this tip, we found that independently of the polarization direction of the incoupled beam, the light emitted from its aperture was polarized primarily around $0^\circ \pm 10^\circ$. Depending on the polarization direction of the input beam, the degree of polarization varied between 0.81 and 0.96. This strengthens our assumption that the bend within the tapered region of the fiber, with a bending radius of around $100\ \mu\text{m}$ and a bending angle of 60° , acts as a polarization filter.

For comparison, we performed the same measurement with a tip fabricated from a MM fiber [tip C in Fig. 2.5(e)]. It had a polarization sensitivity Q_c of only 0.35. When analyzing the light emitted from the aperture at different settings of the half-wavelength plate, we found that the total intensity of light emitted from the aperture strongly depended on the polarization direction of the in-coupled beam. The emitted intensity changed by more than a factor 5 for different input polarizations. At the maximum output intensity, we measured a degree of polarization Q_e of only 0.33. In contrast to the degree of polarization of a SM-fiber based tip, the “polarization-filtering” effect was much less pronounced in this MM-fiber based tip, which might be attributed to coupling between different modes within the bent region of the the MM-fiber taper. Both tips feature similar bending angles and bending radii.

The large spread of θ and Q_c values suggests that for future SNOM experiments, it may be beneficial to routinely pre-characterize the tips to be used. By determining the values θ and Q_c for each tip, the most advantageous orientation of the sample to efficiently excite and detect the desired modes and a polarization-sensitive or polarization-insensitive tip can be chosen, depending on the particular measurement task. In collection-mode measurements, the values θ and Q_c can furthermore help to interpret the obtained images. The measurements presented in Chapters 2.4 (probing the propagation directions of SPPs excited by an aperture tip with a “bull’s eye” grating) and 4.3 (near-field mapping of plasmonic aperture emission by Dual-SNOM) suggest that the far-field polarization properties (i.e., Q_e, Q_c and θ) are related to the orientation of the tips’ near-fields and their near-field polarization sensitivity. In illumination-mode measurements, three retarding elements, either waveplates or fiber-loops ($\lambda/4, \lambda/2, \lambda/4$), can potentially be used to tune the polarization state in the fiber to achieve a high degree of polarization of emitted light. The polarization state of emitted light could be further specified by determining the Stokes parameters.

2.4 Near-field emission of aperture tips observed with a circular grating

It has been reported that the polarization in the near-field emission of an aperture tip can differ from the far-field polarization[147]. Therefore, we separately investigated the aperture’s near-field characteristics via the excitation of surface plasmon polaritons (SPPs) on a planar gold film. As the propagation directions of SPPs excited by a point source

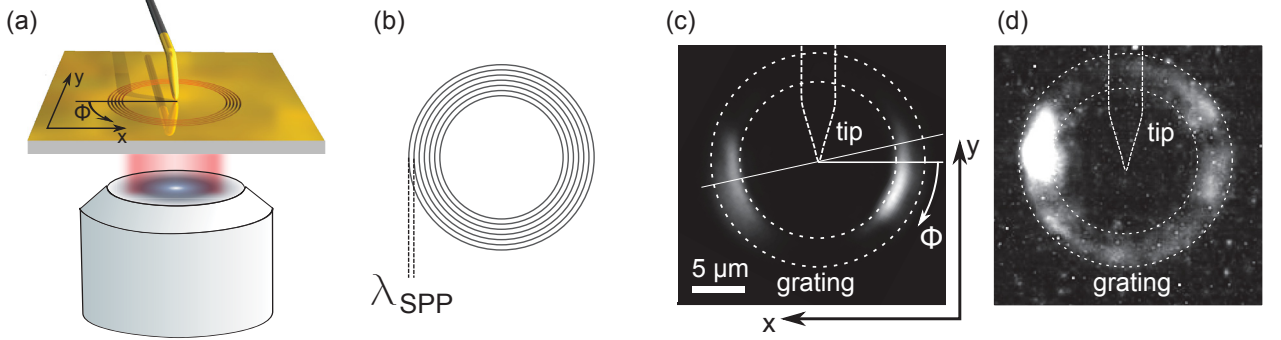


Figure 2.6: (a) Sketch of the “bull’s eye” setup to determine the angular characteristics of SPP excitation by an aperture SNOM tip. The tip is placed in the middle of a circular diffraction grating. The diffracted light is collected by a microscope focused on the sample plane from below. (b) Sketch of the grating. The width of the trenches and ridges is half the SPP wavelength (λ_{SPP}) each, leading to a radial “periodicity” of λ_{SPP} . (c) Resulting microscope image for the SM tip with $Q_e = 0.96$. The positions of the tip and the grating are indicated by dashed lines. (d) Resulting microscope image for the MM tip with $Q_e = 0.33$.

depend on the field orientations of the source, the propagation directions of SPPs excited by an aperture tip allow us to gain insight into the polarization of the aperture’s near-field. The laser with 663 nm wavelength was coupled to the fiber of a SNOM tip, and the tip was placed in the center of a circular grating resembling a bull’s eye [see Fig. 2.6(b)] to probe the SPPs’ propagation directions. The grating consisted of 7 concentric slits that had been milled through a 150 nm thick homogeneous gold film on a glass substrate. The diameter of the inner circle was $15 \mu\text{m}$ whereas, the SPP decay length is $35 \mu\text{m}$ (calculated on the basis of permittivity data from Ref. 148.) The periodicity of the grating corresponded to the SPP wavelength (639 nm, so that SPPs which were excited in the center of the structure and which propagated outwards were diffracted perpendicularly out of the sample plane. The diffracted light was collected by the objective of the inverted microscope, which was focused onto the grating. A sketch of the setup is shown in Fig. 2.6(a). Figure 2.6(c) shows the bottom view of the grating, which is illuminated by tip f, i.e., a tip fabricated from an SM fiber with a degree of polarization of emitted light (in the far-field) $Q_e = 0.96$. The far-field polarization of emitted light is along the x axis. In this bottom view of the bull’s eye grating [Fig. 2.6(c)], light emission from two regions, along the x -axis, can be seen. This directionality of SPP propagation matches the excitation by an electrical dipole along the x -axis[149, 150]. We conclude that the near-field polarization corresponds to the far-field polarization of light emitted by the aperture tip.

The same experiment was repeated with tip C, the tip fabricated from a MM fiber with low polarization sensitivity in collection mode ($Q_c = 0.35$) and a low degree of polarization of emitted light ($Q_e = 0.33$). The bottom-view image of the bull's eye grating is shown in Fig. 2.6(d). Weak light emission from the grating is observed from the whole ring, indicating that SPPs propagate from the tip's position into all directions. A clear maximum appears to the left of the tip, but no corresponding feature on the opposite side occurs. The whole ring appears as a blurred light source. This result can be understood as a further indication of a close relation between the polarization-dependent emission or collection of a tip which is observed in the far-field and its near-field properties.

The aperture SNOM setup described in this chapter has been used to map Airy plasmons (Chapter 5) and to map whispering-gallery modes in microdisk resonators (Chapter 6.2). Furthermore, the setup was extended to a Dual-SNOM setup (Chapter 4). For such Dual-SNOM measurements, the polarization properties of the fiber tips strongly affect the measurement results. The polarization-resolved near-field mapping of plasmonic aperture emission (Chapter 4.3) underlines this property. At the same time, it can be understood as an extension of the "bull's eye" experiment, which was also aimed at characterising a tip's near-field properties via the SPPs it excites.

Chapter 3

Scanning thermocouple-probe microscopy

3.1 Measurement principle and setup

The working principle of SNOM is to scatter the optical near-fields, so that they are partially converted into propagating waves, either in free-space (scattering SNOM) or in an optical fiber (aperture SNOM). These propagating waves eventually reach a photo-detector, which typically converts the optical intensity signal into an electrical signal. Often, the ratio between the near-field intensity and the light which reaches the detector is very low, e.g., due to the low transmission through a small aperture.

Here, an alternative near-field mapping method was developed which is based on absorptive heating of a thermocouple probe[151]. The near-field intensity is converted into a thermovoltage directly at the sample surface. This approach is related to other indirect mapping methods which employ non-optical detectors to map optical fields. In particular, it has been shown that properties of electromagnetic fields can be quantified by exploiting the optically induced forces on a scanning tip[152, 153]. Recently, near-field imaging of a semiconductor laser by means of the heat-induced resonance shift of an AFM probe has been demonstrated [154]. The method was based on measuring the bending of a cantilever due to absorptive heating[155, 156]. An advantage of such absorption-based mapping methods is that they work in a very broad spectral range which is determined by the absorptive properties of the tip's material. In contrast, the detection bandwidth in aperture SNOM is determined by the dispersive properties of the whole detection path, including the aperture tip, the optical fiber, the optical detector and often some bulk optical elements.

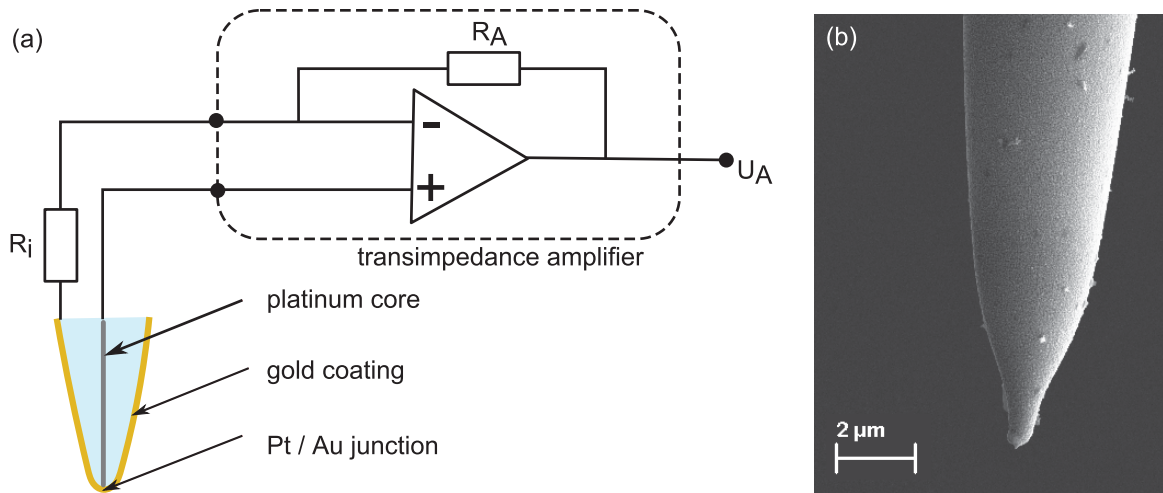


Figure 3.1: (a) Schematic of the circuit and tip for scanning thermocouple-probe microscopy. Heating of the Pt/Au contact at the tip apex generates a Seebeck voltage. The corresponding current (linked via the tip's resistance R_i) is amplified by a transimpedance amplifier to generate the output voltage U_A , which is recorded by the SPM controller. (b) Scanning electron micrograph of a microthermocouple probe.

To map optical near-fields via absorptive heating of a scanning probe, commercially available thermocouple probes (Nanonics Imaging Ltd.) were used, which are fabricated by heating and pulling a micropipette filled with a platinum wire. The resulting tip with the protruding platinum stub is then coated with gold, so that a sub- μm contact between platinum and gold is formed in the apex region of the probe[157] (see schematic drawing in Fig. 3.1) Temperature changes at the tip apex result in a voltage drop between both metals due to the Seebeck effect[158]. The Seebeck voltage generates a current which is measured with a sensitive trans-impedance amplifier (FEMTO DLPCA-200). The Seebeck voltage, and consequently the temperature change of the tip, can be calculated via the probe's resistance R_i and the Seebeck coefficient ($7 \mu\text{V/K}$). As the resistance of most probes is in the order of 100Ω , a temperature difference of 1 K typically creates a current of 50 nA to 100 nA. The absorption efficiency of the metallic tip is related to its size and to the permittivity of the metal at the wavelength that is used in the experiment. The temperature increase at the tip apex is furthermore dependent on heat dissipation. Heat conduction by the surrounding air and by the tip itself are suspected to be the most effective dissipation channels. The dissipation rate strongly depends on the exact tip geometry, including its inner structure. To get a first idea how the the sensitivity changes across the spectral range and for varying tip sizes, the relationship between the tip's material and size and its

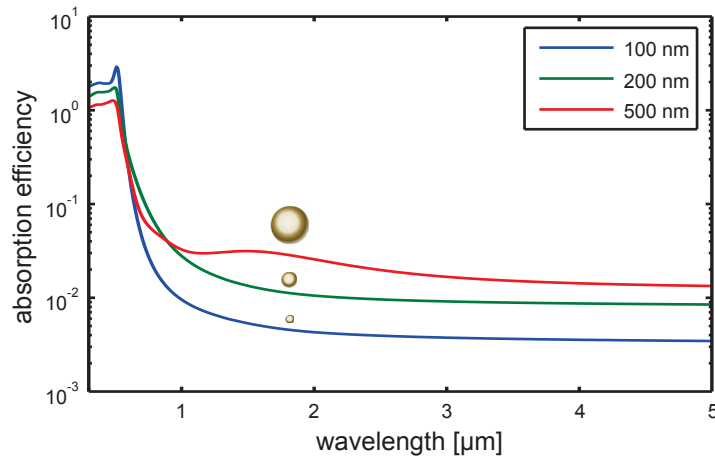


Figure 3.2: Absorption efficiencies (absorption cross section divided by the geometric cross section πr^2) of gold spheres of different diameters (100 nm, 200 nm, 500 nm) in the visible and near-infrared spectral range.

absorption efficiency was approximately modeled by Mie theory[159, 160], by treating the tip as a solid metallic sphere. This model neglects the actual geometry of the tip and the heat conduction towards the tip shaft, so that the results can only give a very rough, qualitative estimate of the actual characteristics. Fig. 3.2 shows the absorption efficiencies (absorption cross section divided by the geometric cross section) of gold spheres with different diameters (permittivity data from [148, 161]). The absorption efficiency dramatically increases for wavelengths below ≈ 500 nm due to the bulk absorption properties of gold, which are governed by intraband transitions in this spectral range[9, 158]. Still, the measurements at wavelengths around 1550 nm (see Chapter 6.4) showed a satisfactory signal-to-noise ratio. Potentially, the method could be even more effective at shorter wavelengths.

In comparison to aperture SNOM tips, which - according to Bethe's theory[48] - exhibit a decrease of the transmission proportional to the fourth power of the aperture diameter, the scaling behaviour of the metal spheres' absorption is expected to be more advantageous. According to Mie theory, the absorption efficiency for short wavelengths even increases when the size of the absorbing sphere is reduced (cf. Fig. 3.2). If this also holds for the much more complex, non-spherical shape of the tip, this effect might permit to achieve higher resolution at a comparatively good signal level by using smaller tips. Also, it might be worthwhile to structure a thermocouple tip so that it exhibits a plasmonic resonance, which is associated with enhanced absorption, at the light wavelength used in the respective experiment.

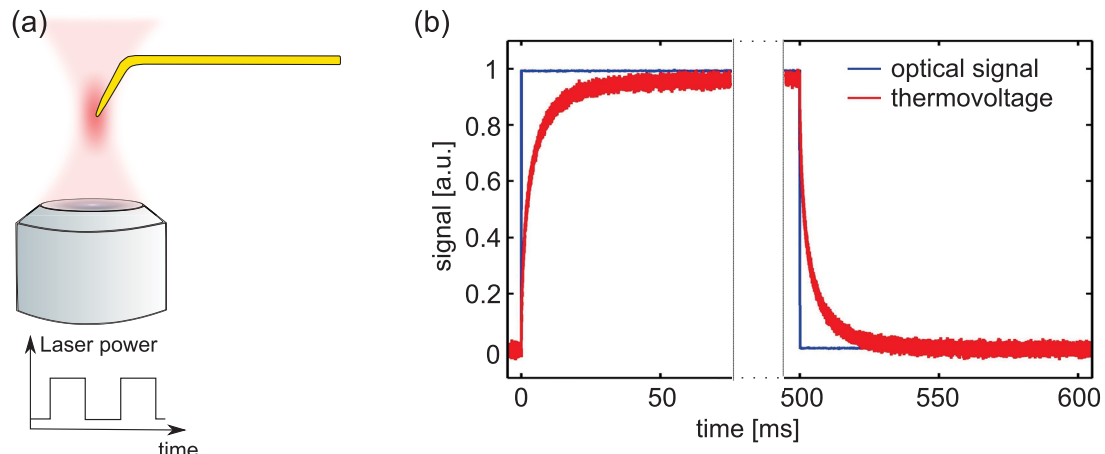


Figure 3.3: (a) Schematic of the experimental setup used to measure the thermal relaxation time of the microthermocouple tips. An infrared laser is focused onto the thermocouple probe by a 50x-objective. The laser is switched on and off with the help of an acousto-optic modulator. (b) Measured thermovoltage signal (red curve) as a function of time, compared to the optical signal (blue curve).

3.2 Temporal resolution

The temporal resolution of the measurement method determines its applicability for time-resolved measurements, e.g., relaxation-time measurements, and it may limit the scanning speed. Provided that the response time of the electronics is sufficiently fast, the achievable temporal resolution is determined by the thermal relaxation of the tip. The most relevant relaxation channels are heat transport within the metallic coating (as opposed to the local heating of a small region at the tip apex inside an optical near-field), conductive heat transport by the surrounding medium (e.g., air) and heat dissipation in the sample on which the tip is placed. This means that the experimental conditions influence the thermal relaxation time. Specifically, the localization of the optical fields, the surrounding medium and the sample's thermal properties are important factors. Also, the tip geometry has an influence on the relaxation into the metallic tip coating and into the surrounding medium.

The temporal response of a thermocouple tip was experimentally determined with the setup sketched in Fig. 3.3(a). The tip was placed in a laser focus [$\lambda=1550$ nm, 50x objective (Mitutoyo), NA=0.65] in air. The laser was switched on and off repeatedly with the help of an acousto-optic modulator (AOM). The thermovoltage signal was recorded using a high-frequency oscilloscope. The response time of the electronics and of the AOM were checked separately and were both below 100 μ s. Fig. 3.3(b) shows the relaxation curve of

a specific thermocouple tip. After the laser was switched off, the recorded temperature dropped exponentially with a relaxation time of around 10 ms. This is a very slow tip relaxation in comparison to a previous publication[157] which claims a response time of a few microseconds for similar probes, measured in water.

The difference between these results can be explained by the different measurement conditions and tip shapes. In our experiment, a few μm -long section of the tip is inside the focal volume and it is irradiated for several ms, leading to heating of a larger portion of the metallic coating of the shaft. In contrast, the reported short relaxation times were measured for irradiation of the tip apex by a sub-ps pulse, meaning that the heating of the metallic coating of the shaft could serve as a relaxation channel. Furthermore, the differences in heat capacity and heat conductivity can lead to shorter relaxation times in water than in air. In near-field measurements, only a small tip volume is illuminated, so that the relaxation time in near-field measurements is expected to be shorter than the times measured in our far-field experiment.

An application of scanning thermocouple-probe microscopy is presented in Chapter 6.4, where a thermocouple probe was successfully used to map whispering-gallery modes in microdisk resonators. In principle, the tip might also detect local variations of the sample's surface temperature induced by light absorption in the sample. In Chapter 6, we show that in this specific measurement the recorded "thermovoltage" actually reflects the optical intensity, rather than the sample surface temperature. Generally, the relative contributions of conductive and radiative heat transfer between the sample and the tip, on the one hand, and optical absorption, on the other hand, have to be estimated for the specific experimental configuration in which scanning thermocouple-probe microscopy is used.

The tips absorb propagating and evanescent waves to the same extent, which may be detrimental if one is primarily interested in the evanescent fields. Therefore, the method is particularly suited in situations where the near-field under investigation is not superposed by a strong propagating field, e.g., the illuminating field.

Chapter 4

Instrumentation for Dual-SNOM

As presented in Chapter 2, the aperture tip of a SNOM is commonly used either to locally illuminate the sample or to collect light at the sample surface: The fiber constitutes a convenient way to guide the light from the source to the location of interest at the sample surface (illumination mode) or from the sample to the detector (collection mode). With the exception of illumination-collection mode, the respectively other path is realized differently, for example by far-field illumination through a microscope objective, or through a fixed, tapered optical fiber. Sometimes the sample or the phenomenon under investigation predefines this path. Two examples, the excitation of Airy plasmons by a specially designed grating and the excitation of whispering-gallery modes in microresonators by evanescent coupling from a tapered fiber loop, are presented in detail in Chapters 5 and 6, respectively. However, in some systems the modes of interest can either not be excited in a straightforward way, or the utilization of the widely-used far-field illumination through a microscope objective would generate unwanted background signals.¹ Illumination-mode SNOM maps can reveal the optical LDOS of samples [129–131, 163], but contain little information on the specific modes which eventually add up to the LDOS. Collection-mode SNOM maps, on the other hand, give insight into the cumulated near-field distribution of the specific set of modes which is excited under the given illumination conditions. The illumination is usually restricted by the limitations of far-field optics, i.e., the illumination spot is, in the best case, diffraction limited.

Here, a Dual-SNOM system is presented which combines two aperture SNOM tips, of which one is used for near-field excitation and the other for simultaneous near-field collection.

¹An example of such a system are particle-chain waveguides[162], in which it is difficult to observe waveguiding because the decay length is shorter than the diffraction limit.

As both tips can be freely positioned on the sample, this technique opens up a multitude of new options for near-field optical investigations and allows one to get rid of bulky far-field illumination schemes. If one assumes that both tips constitute point-like emitters / detectors, such a setup paves the way to mapping near-field Green's functions of almost arbitrary samples. However, for a complete measurement of the Green's function, one would have to measure the amplitudes and phases of all components of the electromagnetic fields for three different polarizations of the excitation source. Recently, approaches to access the complete vectorial electromagnetic near-field by collection-mode aperture SNOM, utilizing an interferometric setup and polarizers in the detection path, have been described[38, 126]. The contributions of different field components to the intensity maps recorded in our SNOM measurements are investigated in section 4.3. Apart from using the setup as a Dual-SNOM, one of the tips could be replaced by a different type of fiber-based SPM probe, giving access to other properties of the sample which may be affected by near-field illumination, e.g., electrical properties, surface temperature, or topography.

The Dual-SNOM setup is particularly useful for the investigation of transport or propagation phenomena, like light guiding in plasmonic waveguides (see Chapter 7). While previous studies on plasmonic waveguides relied on extended pads[164–167] for excitation, we can use an aperture tip to selectively excite a single waveguide in a waveguide array, and, by varying the tip's position, the relative excitation strength of different modes can be tuned.

Dual-SNOM setups have recently been used by other research groups to visualize the propagation of SPPs on metallic surfaces and waveguides [168–170], modes on plasmonic metasurfaces[109] or the carrier dynamics in quantum wells[171, 172]. However, a number of challenges have to be overcome to successfully conduct and understand Dual-SNOM measurements: As the length-scales of the structures of interest and of the investigated phenomena lie in the nanometer or micrometer range, the illuminating and the collecting tip have to be brought within close distances of each other. Collisions between the tips can lead to damage of the metallic tip coatings or to breaking of the tip. Therefore, it is necessary to avoid collisions by controlling the distance between both tips during Dual-SNOM measurements. We developed a mechanism which prevents the two tips of a Dual-SNOM from colliding during a scan, thereby establishing an important prerequisite for Dual-SNOM measurements (Chapter 4.2).

Furthermore, two of the main difficulties in SNOM are aggravated in Dual-SNOM: First, as the transmission through SNOM apertures is low, signal levels are typically extremely

weak. When two aperture tips are involved, this decreases the overall transmission, so that it is difficult to collect signals with sufficient signal-to-noise ratio. New tip designs with enhanced throughput, e.g., fully coated fiber probes employing SPP nano-focusing at the apex,[81, 82, 173] have the potential to resolve this issue. Second, the interpretation of recorded images becomes even more involved than for standard aperture SNOM measurements. In a scalar model, one could potentially relate the measured signal to a (scalar) Green's function of the sample, i.e., one can obtain a relation to the response to a point source. However, the electromagnetic field is in reality vectorial, and polarization effects can play an important role in the measurement. Collection-mode SNOM measurements are often designed to map components of the electromagnetic fields which are perpendicular to the tip's axis, without discriminating different field orientations. In contrast, when using a fiber tip for illumination, the tip's near fields have particular orientations, which may depend on a multitude of parameters, like the polarization of the beam that is coupled into the fiber, and bend-induced birefringence in the fiber. The orientations of electric and magnetic fields influence the coupling to modes of the sample under investigation. Furthermore, each of the tips can influence the local fields in its vicinity and disturb the sample's modes.

In the first part of this chapter, the different Dual-SNOM configurations that have been realized in the course of this study are described. In the second part, a technique to prevent collisions by detecting acoustic and mechanical interactions between both tips is introduced. The third part of this chapter analyzes the properties of our Dual-SNOM system in terms of near-field emission and detection characteristics of both tips. As an application, Chapter 7.2 presents Dual-SNOM measurements on plasmonic stripe waveguides, which employ the methods and findings of this chapter.

4.1 Dual-SNOM setups

In the course of this thesis, three different Dual-SNOM configurations have been implemented, using two different commercial single-SNOM systems. The first system is the Nanonics MultiView 4000 SNOM system, which has been described in detail in Chapter 2.2 [see Figures 2.2, 4.2, and 4.1(a) and (b)]. Its cantilever design permits optical access from above and the integration of several SNOM heads into a multi-probe setup. The tip position is not closed-loop controlled. As in Dual-SNOM measurements, drifting or inaccurate positioning of the illumination-probe could strongly affect the experimental

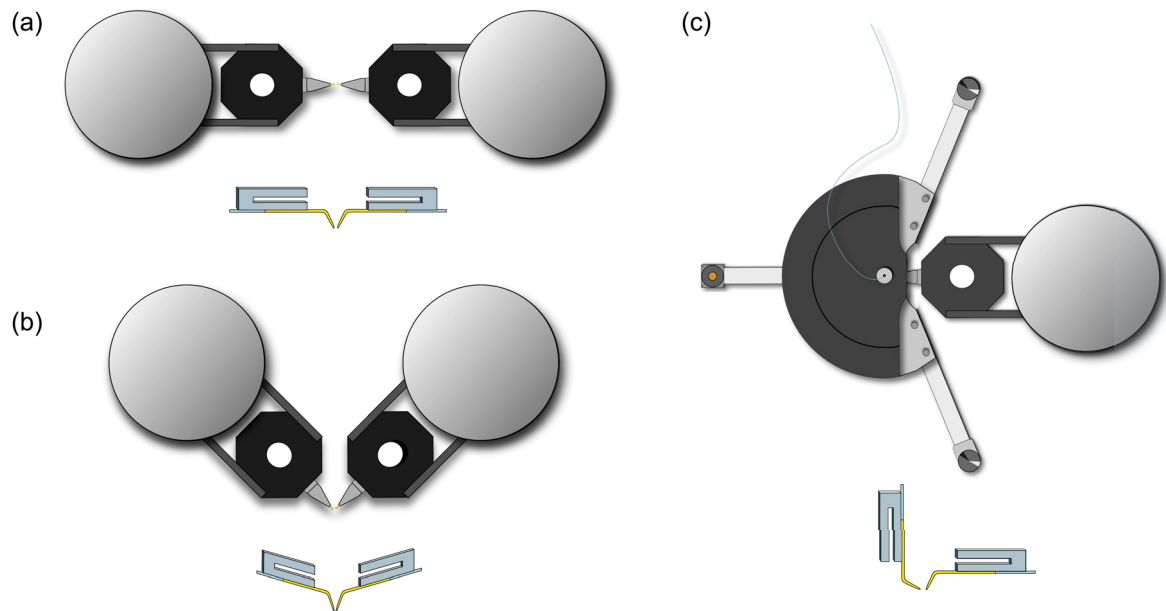


Figure 4.1: Three different realizations of Dual-SNOM (top views and tuning fork / tip orientations): (a) Two Nanonics heads in “parallel” configuration. (b) Two Nanonics heads in “perpendicular” configuration. (c) A Nanonics head and a NT-MDT head combined into a “mixed” Dual-SNOM setup.

results, we mostly kept the illumination tip at the center of its xy -scanning range during our Dual-SNOM experiments to reduce tip drifting. At the center position, no voltage was applied to the scanning piezos, and the sample scanner, equipped with closed-loop control, was used to position the structure under investigation relative to the illumination tip. Thus, piezo drift of the illumination tip with respect to the sample could not affect the measurements, and we could not find any signs of drift in our measurement results.

Two different Dual-SNOM configurations (“parallel” and “perpendicular”) were realized with two identical Nanonics SNOM heads, as shown in Fig. 4.1(a) and (b). The third SNOM configuration [see Fig. 4.1(c)] employs the NT-MDT NTEGRA Solaris head, in which the tip is fixed to an upright tuning fork.

In the NT-MDT SNOM head, the prongs of the tuning fork and the tip oscillate parallel to the sample surface, so that shear-forces occur between tip and sample, reducing the oscillation amplitude. A feedback mechanism keeps the tip-sample distance constant by maintaining a constant oscillation amplitude[132, 174]. A 3D piezo scanner with a movement range of $100 \times 100 \times 6 \mu\text{m}^3$ is integrated in the NT-MDT SNOM head, which is supported by three legs. To integrate the head with the large piezo stage used for sample scanning, the

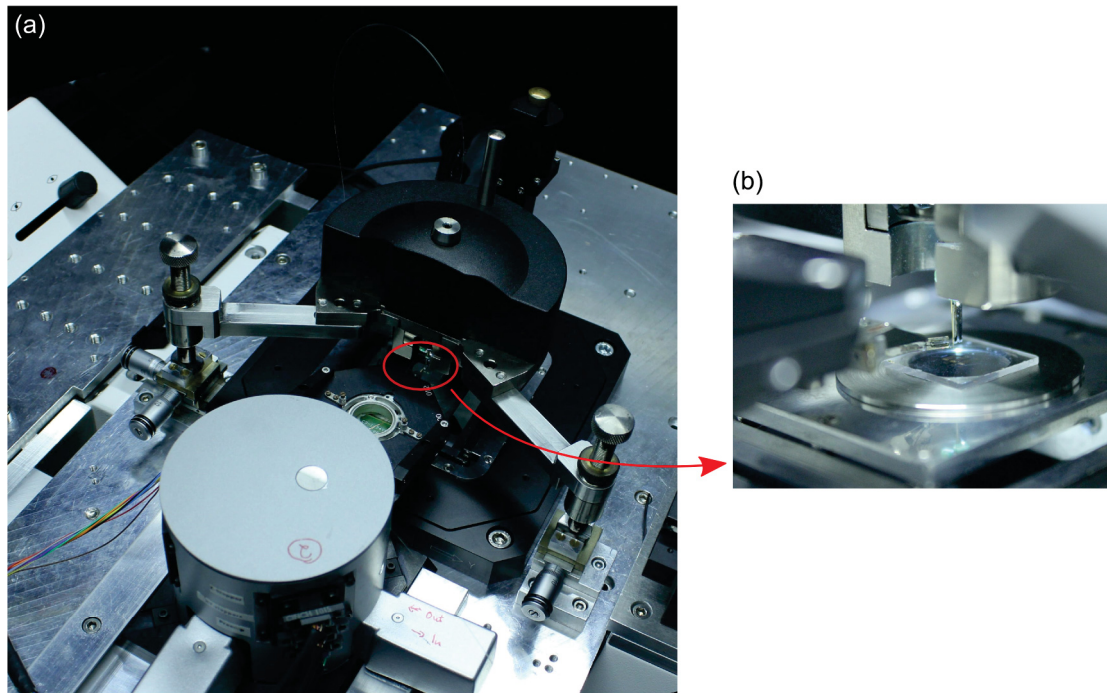


Figure 4.2: (a) Photograph of two SNOM heads combined into a “mixed” Dual-SNOM setup [cf. Fig. 4.1(c)]. (b) Side-view of the two tuning forks and the sample.

legs were extended with custom-made steel insets. Coarse positioning of the head is possible via manual translation stages. Due to its sturdy design, this SNOM head is less susceptible to vibrations, and the tip position is closed-loop controlled. The closed-loop position control is particularly advantageous for precise positioning of the probe for localized illumination of the sample in a Dual-SNOM experiment using this SNOM head. Due to the geometry of this SNOM head, optical access from above is restricted, and two such heads cannot be integrated into a Dual-SNOM setup.

We succeeded in combining the NT-MDT SNOM head with a Nanonics SNOM head into a “mixed” Dual-SNOM system [see Fig. 4.1(c) and Fig. 4.2]. In order to permit the two tip apices to be positioned at sub- μm distances of each other without the tip shafts touching, we glued a bent tip (from Nanonics) to the upright tuning fork [see Fig. 4.1(c)]. We used this setup to develop a collision-prevention mechanism (see Chapter 4.2). However, it turned out that without optical access from above, the operation of the Dual-SNOM system was quite difficult. The collision-prevention mechanism helps to avoid tip collisions during scanning, but for coarse alignment of the sample and both tips, the observation through a microscope with moderate magnification (e.g., 20x) is very helpful. In the Dual-SNOM

configuration with the NT-MDT head, such a microscopic observation was only possible through a microscope from below and with an (at least partially) transparent sample. However, when illuminated through the same objective, i.e., in far-field reflection mode, the tips are hardly visible and difficult to find. The visibility in dark-field mode was better than in bright-field mode. The tips are easily visible in transmission-mode or in reflection-mode from above, when the light that is reflected by the sample illuminates the tips. As we could not install a light source or a reflector above the tips, their visibility in the inverted microscope was so poor that this setup was difficult to work with and we performed our Dual-SNOM measurements reported in Chapters 4.3 and 7 with the Dual-SNOM setups consisting of two Nanonics SNOM heads [Fig. 4.1(a) and (b)].

Each SNOM head is controlled by a computer via a SNOM controller. The sample scanning stage is equipped with its own voltage amplifier and control electronics, which permit closed-loop controlled positioning of the scanning stage either via turning knobs on the controller, via digital input signals, or via control voltages. For performing a stage scan, we use the SNOM's computer and software (commercial SPM software NWS11, Nanonics Imaging Ltd.) to generate low voltage outputs which encode the scanner's x and y positions. These low voltages are used as control voltage inputs of the stage controller, so that the stage performs the desired two-dimensional scanning motion and signals (e.g., topography signals from both tips and optical signals) can be acquired via the SNOM controller's signal inputs. Thus, two-dimensional maps for each of the signals can be assembled by the SPM software.

4.2 Distance control

As collisions between both tips can lead to damage of the tips, we established a distance monitoring method, based on mechanical interactions between both tips, which oscillate at different frequencies [175]. In the two configurations with two similar SNOM heads operating in tapping-mode [Fig. 4.1(a) and (b)], the tips oscillate vertically and therefore parallel to each other. In contrast, the "mixed" configuration in Fig. 4.1(c) employs a tip which oscillates horizontally, along the sample surface. These different oscillation directions lead to differences in the mechanical interaction between the two tips. Therefore, we treat two configurations separately: The "parallel" configuration, as shown in Fig. 4.1(a), and the "mixed" configuration, as shown in Fig. 4.1(c). In terms of mechanical interaction

between the two scanning tips, the “perpendicular” configuration [Fig. 4.1(b)] resembles the “parallel” one and is therefore not separately discussed.

To detect mechanical interactions between both oscillating tips, we make use of the fact that both tips generally oscillate at different frequencies. If, coincidentally, the two tips used in a Dual-SNOM experiment exhibit approximately the same resonance frequency in their first mechanical eigenmode (which is in the range of 32 kHz to 45 kHz), one of them can be driven at the frequency corresponding to its second mechanical eigenmode, which is usually between 210 and 240 kHz.

Due to its piezoelectricity, each oscillating tuning fork generates a voltage signal which is related to the deflection of its prongs. This response signal is used by the feedback loop of the SNOM controller which keeps the oscillation phase, and therefore the tip-sample distance, constant during scanning. We analyze the tuning fork response signal of the first, “sensing” tuning fork, which oscillates at its resonance frequency f_1 with a lock-in amplifier locked at the oscillation frequency f_2 of the second tuning fork. We call the amplitude output of the lock-in amplifier “cross-talk”. It contains information about the interaction force between the two tips.²

4.2.1 Theoretical model

In the following, a mathematical model of the cross-talk signal is developed. It applies to all three Dual-SNOM setups described above. We regard each of the tuning forks as a mechanical oscillator with a set of eigenmodes. Only the first two eigenmodes α and β , with the eigenfrequencies $f_{j,\alpha} \approx 37$ kHz and $f_{j,\beta} \approx 190$ kHz, play a role in the experiment. The index $j = 1, 2$ denominates the individual tuning forks. We now describe each of the four eigenmodes as an individual oscillator. We assume that the four oscillators are

²It should be mentioned that a similar mechanism to control the distance between two tips in a Dual-SNOM setup was independently developed by Kaneta et al.[172]. In their setup, in addition to the resonant oscillations of the tuning forks employed for sensing the tip-sample distance, an additional, non-resonant oscillation of one tuning fork is excited. By demodulating the other tuning fork’s deflection at this non-resonant frequency, the distance between both tips is monitored.

weakly coupled and that they oscillate harmonically. The oscillator deflections x_{jk} are then described by the following equations:

$$\ddot{x}_{1\alpha} + 2\gamma_{1\alpha}\dot{x}_{1\alpha} + \omega_{1\alpha}^2 x_{1\alpha} + \sigma_{12}(x_{2\alpha} + x_{2\beta}) + \sigma_{11}x_{1\beta} = F_1 e^{i\omega_1 t}, \quad (4.1)$$

$$\ddot{x}_{1\beta} + 2\gamma_{1\beta}\dot{x}_{1\beta} + \omega_{1\beta}^2 x_{1\beta} + \sigma_{12}(x_{2\alpha} + x_{2\beta}) + \sigma_{11}x_{1\alpha} = F_1 e^{i\omega_1 t}, \quad (4.2)$$

$$\ddot{x}_{2\alpha} + 2\gamma_{2\alpha}\dot{x}_{2\alpha} + \omega_{2\alpha}^2 x_{2\alpha} + \sigma_{12}(x_{1\alpha} + x_{1\beta}) + \sigma_{22}x_{2\beta} = F_2 e^{i\omega_2 t}, \quad (4.3)$$

$$\ddot{x}_{2\beta} + 2\gamma_{2\beta}\dot{x}_{2\beta} + \omega_{2\beta}^2 x_{2\beta} + \sigma_{12}(x_{1\alpha} + x_{1\beta}) + \sigma_{22}x_{2\alpha} = F_2 e^{i\omega_2 t}, \quad (4.4)$$

where γ_{jk} are the damping constants, and ω_{jk} are the (angular) eigenfrequencies of tuning fork j in the oscillation mode $k = \alpha, \beta$. The coupling constant between both tuning forks is σ_{12} , σ_{jj} is the coupling constant between the two oscillation modes of the same tuning fork j . F_1, F_2 and ω_1, ω_2 are the amplitudes and (angular) frequencies of the external driving forces, respectively. Each driving frequency ω_j may slightly differ from the respective eigenfrequency ω_{jk} . It should be noted that by introducing the total deflections $x_j = x_{j\alpha} + x_{j\beta}$ in the coupling terms between both tuning forks, we have presumed that the deflections associated with the two oscillation modes occur along the same direction. As only two oscillation frequencies occur, we can solve the system of equations by the ansatz

$$x_{jk} = A_{jk} e^{i\omega_1 t} + B_{jk} e^{i\omega_2 t}. \quad (4.5)$$

for the steady-state case.³ A_{jk} and B_{jk} are complex coefficients describing the response of the tuning forks at the frequencies ω_1 and ω_2 , respectively. Again, we express the total deflection of each oscillator as the sum of the deflections corresponding to the two oscillation modes, $x_{j\alpha}$ and $x_{j\beta}$:

$$x_j = x_{j\alpha} + x_{j\beta}. \quad (4.6)$$

The cross-talk signal (*CT*), which is measured by the lock-in amplifier, is the oscillation amplitude of the first tuning fork at the frequency f_2 , which is the driving frequency of the second tuning fork. In our mathematical framework, this corresponds to the oscillation amplitudes $B_{1\alpha}$ and $B_{1\beta}$:

$$CT = |B_{1\alpha} + B_{1\beta}|, \quad (4.7)$$

³Based on typical quality factors in the order of 500, the settling time of the oscillation can be estimated to be at most 15 ms, which is of the same order as the sampling time per pixel. Therefore, the transient case is not discussed here.

where $B_{1\alpha}$ and $B_{1\beta}$ are the oscillation amplitudes of the first tuning fork's oscillation modes α and β at the frequency f_2 .

In order to obtain a simple analytic expression for the cross-talk CT , several approximations were made: First, as the resonance frequencies $\omega_{j\alpha}$ and $\omega_{j\beta}$ are much further apart than the relevant resonance bandwidths, terms which describe the excitation of a tuning fork's first oscillation mode at the frequency ω_2 and vice versa were neglected. With this approximation, equation 4.7 reduces to $CT = |B_{1\beta}|$. Second, higher-order coupling terms, i.e., terms containing several factors of σ_{ij} , were neglected. With these approximations, we obtain the following expression:

$$CT \approx |B_{1\beta}| \approx |\sigma_{12}| \frac{F_2}{(\omega_{2\beta}^2 - \omega_2^2 + 2i\gamma_{2\beta}\omega_2)} \frac{1}{(\omega_{1\beta}^2 - \omega_2^2 + 2i\gamma_{1\beta}\omega_2)} \propto |\sigma_{12}| \quad (4.8)$$

The cross-talk amplitude is proportional to the coupling coefficient $|\sigma_{12}|$, which describes the interaction cross section between both oscillators, and which encodes the distance-dependence of the cross-talk signal. The first fraction in equation 4.8 represents the oscillation amplitude of the second oscillator, and the second fraction describes the response of the first, "sensing" tuning fork at the driving frequency ω_2 of the second tuning fork.

Clearly, in order to achieve a high cross-talk signal - and therefore a high sensitivity of the distance-sensing method - this response should be as high as possible. Ideally, the frequencies $\omega_{1\beta}$, $\omega_{2\beta}$ and ω_2 should be close. Of course one might drive the second oscillator at the first oscillator's eigenfrequency $\omega_{1\beta}$ to maximize the second fraction, even if the two tuning forks' eigenfrequencies $\omega_{1\beta}$, $\omega_{2\beta}$ are not identical. On the other hand, if the driving force was kept constant, the oscillation amplitude of the second tip would be low (the first fraction in equation 4.8). Additionally, as the second tuning fork would not be resonantly driven, this might deteriorate the quality of the feedback.

In the following, experimental investigations of the cross-talk in two different Dual-SNOM setups are presented. The tuning forks used in these experiments were not specifically selected to have matching eigenfrequencies. Therefore, the difference between the eigenfrequencies $\omega_{1\beta}$ and $\omega_{2\beta}$ was several kHz in both cases.

4.2.2 Mechanical interaction in the "parallel" Dual-SNOM configuration

Fig. 4.3(a) and (b) show maps of the topography and the cross-talk signal, recorded with the "parallel" Dual-SNOM setup [see Fig. 4.1(a)] on an unstructured quartz substrate. As we

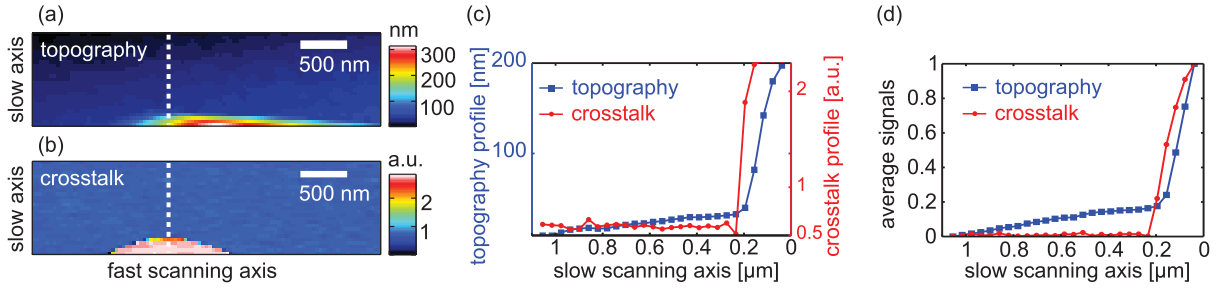


Figure 4.3: Variations in the “topography” and “cross-talk” signals as the scanning tip approaches the stationary tip in the “parallel” Dual-SNOM configuration [cf. Fig. 4.1(a)]. (a) and (b) show the simultaneously acquired maps of the topography and cross-talk signals, respectively. The stationary tip is located at the center of the bottom edge of the images. (c) Profiles of the topography and the cross-talk signals along the dashed lines in (a) and (b). (d) Average signal values along each horizontal scanning line (fast scanning axis) of the topography and cross-talk signals. Both signals have been normalized. The zero of the x axis indicates the position where the scan was stopped.

will see, this “bare” substrate gives little or no contribution to the signals of interest. Tip 1 (the “sensing” tip) was kept stationary. Its height was controlled by its feedback mechanism, and it oscillated at $f_1 = 37$ kHz, corresponding to the fundamental mechanical eigenmode of its tuning fork. Its position was near the center of the bottom edge of the images. Tip 2 was used to scan the sample surface, gradually approaching the first, stationary tip. Its oscillation frequency was $f_2 = 210$ kHz, which corresponds to the second mechanical eigenmode of its tuning fork. After the first observable mechanical interaction between the tips occurred, as clearly observed in the cross-talk signal, the scan was continued for a few scanning lines before it was manually stopped (lower edge of the images).

In the topographic image [Fig. 4.3(a)], the stationary tip is visible as a smeared-out feature at the bottom edge of the image, with a lateral extension of over $2\ \mu\text{m}$ and a maximum height of around 300 nm. The stationary tip hence appears as a topographic feature for the second, scanning one. The cross-talk signal [Fig. 4.3(b)] is at noise level when both tips are far apart. It sharply increases when the scanning tip approaches the stationary one and shear forces between both tips occur. In contrast to the topography signal, the cross-talk signal exhibits a clear step between the noise level and a significant signal. The region of strong interaction forms a sharply delimited circle segment, which apparently corresponds to the area where shear-force interactions between both tips occur. The step-like increase in the cross-talk signal occurs at least one scanning line - i.e., several tens of nanometers - earlier than in the topography signal, as can be seen from the profiles

of both signals [Fig. 4.3(c)]. Consequently, by using the cross-talk signal as a closeness indicator, the scan can be stopped before the tips would collide and suffer damage.⁴

With regard to an automated collision-prevention scheme, it might be preferable to make use of the line-averaged cross-talk signal, i.e., the average of the cross-talk signal along each (horizontal) scanning line. This signal is less noisy than the original signal, it is easily accessible during the scan and the amount of data which has to be processed by the algorithm is significantly reduced. Fig. 4.3(d) shows the line-averaged cross-talk and topography signals. For better comparison, both curves have been linearly rescaled. While the averaged topography signal increases monotonically, due to drift or a slight tilt of the sample, the cross-talk signal is constant, with very little noise, until it sharply increases. Again, a significant increase in the integrated cross-talk signal occurs earlier than in the topography signal. The increase strongly surpasses the noise level. Therefore, the averaged cross-talk signal is suited as a reliable indicator of the shear-force interactions between both tips, which occur without damage.

We found that if the resonance frequencies of the first eigenmodes of both oscillators, $\omega_{1\alpha}$ and $\omega_{2\alpha}$, are at least 1 kHz apart, it is also possible to drive both oscillators at their first eigenmode and detect the cross-talk with the lock-in time constant set to 20 ms. If the eigenfrequencies are less than 1 kHz apart, the time constant has to be larger to allow for the lock-in to separate the two frequencies. At the same time, the “background” level of the cross-talk signal (when both tips are far apart) rises, which makes the method less reliable for such small frequency differences.

4.2.3 Mechanical interaction in the “mixed” configuration

The same kind of measurement was performed with the “mixed” Dual-SNOM configuration sketched in Fig. 4.1(c).

The first, vertically oscillating tip was kept stationary, and its oscillation frequency was $f_1 = 37$ kHz. The second tip was attached to an upright, horizontally oscillating tuning fork. We usually operate this tuning fork at its second mechanical eigenmode. In the measurement presented here, its frequency f_2 was 190 kHz, and it was used to scan the sample surface. Shear forces between the tip and the sample were used to sense the sample topography. While scanning the sample with the second tip, the response signal of the first

⁴By investigating used tips in a scanning-electron microscope (SEM), it was confirmed that the interaction which leads to the sharp increase of the cross-talk signal does not cause visible damage to the tip.

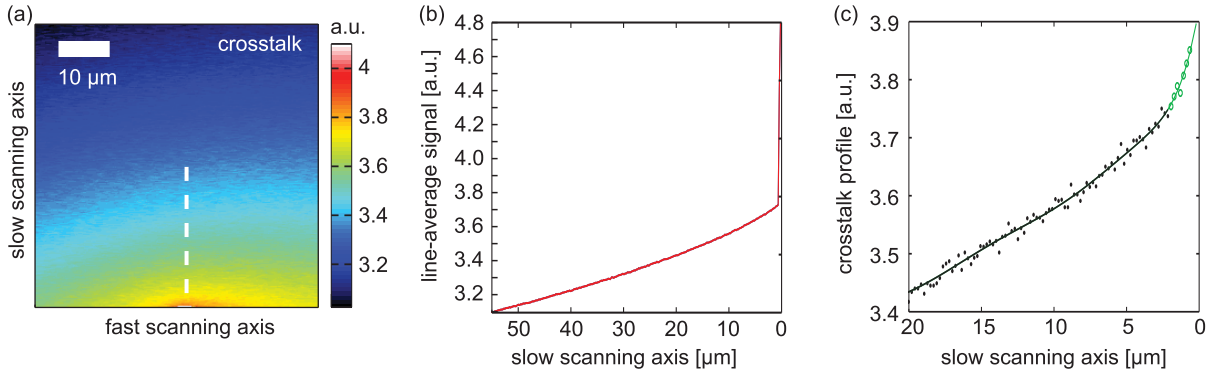


Figure 4.4: Variations in the cross-talk signal as the scanning tip approaches the stationary tip in the “mixed” Dual-SNOM configuration [cf. Fig. 4.1(c)]. (a) Maps of the cross-talk signals. The stationary tip is located at the center of the bottom edge of the image. (b) Average cross-talk signal along each horizontal scanning line (fast scanning axis). The zero of the x axis indicates the position where the scan was stopped. (c) Profile of the cross-talk signals along the dashed line in (a). The different markers indicate different interaction regimes. The drawn-out line is a polynomial fit of the measured values and serves as a guide to the eye.

tuning fork was demodulated at the reference frequency f_2 to obtain the cross-talk signal, as before.

The cross-talk image is shown in Fig. 4.4(a). Again, the stationary tip was located near the center of the bottom edge of the image. The scanning tip oscillated horizontally, along the direction of the slow scanning axis. Unlike in the previous measurement with two tips oscillating vertically, the cross-talk signal now showed spatial variations even when both tips were several tens of micrometers apart, indicating a long-range interaction between both tips. As the scanning tip approached the stationary tip, the cross-talk signal monotonously increased. For the specific combination of tips used in this measurement, the interaction could be detected even when both tips were several hundreds of micrometers apart (not shown here). When we exchanged the vertical tip for another, similar one, the range in which interaction between both tips could be detected was reduced. However, some long-range interaction between the tips at distances of few μm to tens of μm could always be observed in the “mixed” configuration.

Due to the large scale of the image in Fig. 4.4(a), the region where both tips touch is not well visible. However, similar to the previous measurements, the onset of shear forces between the tips leads to a sharp increase of the cross-talk signal. The color scale has been chosen to show the long-range signal variations. The actual maximum of the signal was by

a factor of 5 higher than the maximum of the color scale. In Fig. 4.4(b), the average of the cross-talk signal along the (horizontal) scanning lines is shown. Apart from the slow increase due to long-range interaction between both tips, a sharp and step-like increase indicates shear force interaction between both tips and can be used as a warning signal to prevent collisions and the resulting tip damage.

The cross-talk signal [Fig. 4.4(a)] seems to be radially symmetric with respect to a virtual center lying outside of the recorded image, i.e., it does not coincide with the stationary tip's position at the bottom edge of the image. This could be caused by contributions to the observed long-range signal beyond interactions between the two tips. Interactions between the two tuning forks, or between the tips and the tuning forks, could explain this feature.

The long-range forces between both oscillators could be due to electrostatic charges, acoustic interactions transmitted through the sample or acoustic interactions transmitted through the air. By retracting both tips from the sample for a comparative scan, the transmission of vibrations through the sample could be ruled out as the main interaction mechanism. Likewise, the influence of electrostatic charges has been experimentally ruled out by using metal-coated tips and a metalized, grounded sample. Strong long-range interaction was observed in a control experiment with the same tuning forks, but without the fiber tips. This suggests that interaction between both tuning forks is the main source of long-range interaction at distances above a few micrometers. As electrostatic forces have been ruled out, we attribute the observed long-range interactions to acoustic interaction transmitted by the air between both tuning forks: When the horizontally oscillating tuning fork vibrates at its frequency f_2 , it generates a sound wave, i.e., the air pressure oscillates. This generates a dynamic force which acts on the other tip and tuning fork. The first, “sensing” tip and tuning fork then perform an additional oscillation at the frequency f_2 of the second tuning fork, which is linearly superimposed on its vibration at its own eigenfrequency f_1 (see section 4.2.1).

We consider the profile of the cross-talk signal along the dashed line in Fig. 4.4(a) in order to investigate the distance-dependence of the interaction between both oscillators [Fig. 4.4(c)]. In this graph, the region of shear force interaction between the tips with a sharp increase of the signal (few tens of nanometers) is omitted. Two different regions with different slopes are discernible, distinguished by different markers in Fig. 4.4(c). The signal increases significantly faster when both tips are less than around $2\ \mu\text{m}$ apart [green circles in Fig. 4.4(c)], indicating a pronounced tip-tip interaction at short distances. We suppose that while the interaction between both tuning forks is observable in the entire scanning

region and leads to the moderate slope of the profile at large distances between the tips, tip-tip interaction with a shorter range becomes observable above this background when both tips are only few micrometers apart. We suppose that similarly to the interaction mechanism between both tuning forks suggested above, aerodynamic processes mediate the tip-tip interaction. Its range is short because the oscillating tip, which generates the air movement and air pressure variations, is small in comparison to the tuning fork considered above.

To summarize, three interaction mechanisms with different ranges have been identified by analyzing the cross-talk signal in the “mixed” Dual-SNOM configuration: While acoustic interactions between both tuning forks can be observed at distances of up to several hundred micrometers, acoustic (or aerodynamic) tip-tip interactions are observed when both tips are few micrometers apart. Finally, when the tips touch, shear forces lead to a drastic increase of the cross-talk signal.

In contrast, in the “parallel” Dual-SNOM configuration with two cantilevered tips, the air oscillation mainly occurs in vertical direction. We assume that due to the different directional characteristics, aerodynamic interaction between the oscillators is not high enough to be detected. This would explain why in the “parallel” configuration, no interaction between the two tips is observed when they are more than a few tens of nanometers apart.

4.3 Optical emission and detection characteristics

The warning mechanism presented above constitutes an important prerequisite for performing Dual-SNOM measurements. Another prerequisite to successfully apply Dual-SNOM is to understand the inherent optical characteristics of this technique. While it is straightforward to regard the excitation tip as a point-source of SPPs on a metal film[168–170], or, more generally, as a point-source of electromagnetic radiation, different models have been employed in the past to describe the polarization characteristics of the excitation tip, which was either regarded as a point dipole[168] or as a “randomly polarized” source,[170] i.e., the dipole orientation was assumed to fluctuate randomly. By comparing the Dual-SNOM measurements to intensity distributions, polarization-insensitive detection was so far implicitly assumed.

Here, we build on the findings on the far-field polarization characteristics (Chapters 2.3 and 2.4) of the bent fiber tips to systematically investigate the image formation process

in Dual-SNOM.⁵ The results also provide valuable insights into excitation and detection properties of standard SNOM with aperture tips.

In Chapter 2.3, it was found that the collection efficiency of bent aperture SNOM tips is polarization dependent. For each tip, a preferential direction θ exists. Free-space light polarized along θ is detected more efficiently than light polarized perpendicular to θ . Generally, tips fabricated from SM fiber are more polarization-sensitive than tips fabricated from MM fiber. A specific tip was shown to emit light with a high degree of linear polarization $Q_e = \frac{I_\theta - I_{\theta+90^\circ}}{I_\theta + I_{\theta+90^\circ}} = 0.96$. It was also shown in Chapter 2.4 that the near-field polarization corresponds to the far-field polarization.

The Dual-SNOM setup consisting of two identical SNOM heads in the “parallel” configuration [Fig. 4.1(a)], was used for a first Dual-SNOM experiment. In this experiment, the SPPs excited by this particular tip’s near-field emission were directly mapped [see Fig. 4.5]. The experimental configuration is depicted in Fig. 4.5(a). The light emitted into the far-field by this tip is mostly polarized along the x direction (corresponding to 0° , see Chapter 2.3). The excitation tip was placed on an unstructured, 55 nm thick gold film on which SPPs can be excited, and a collection-mode SNOM measurement was performed with the collection tip in the region around the excitation tip. The unstructured gold film constitutes a highly symmetric sample, so that any asymmetries in the obtained image originate from the measurement setup itself.

As MM tips exhibit a higher collection-efficiency than SM tips, a MM tip was used to collect the plasmonic near-fields. The collection tip had a far-field polarization sensitivity (cf. Chapter 2.3) of 0.42 and was most sensitive to light polarized along $\theta = -9^\circ$, which is close to the polarization of light emitted by the excitation tip. Inside the MM fiber which guides the collected light to the detector, the polarization is not well preserved due to mode mixing and bend-induced birefringence. Therefore, we did not attempt to analyze the polarization of collected light by placing an analyzer in the detection path.

Both tips’ distances from the sample surface were controlled by their respective tuning-fork based feedback mechanism, and the collision-warning mechanism described in Chapter 4.2 was used to prevent collisions between the two tips. The power coupled into the illuminating tip was below 15 mW to avoid melting of the metal coating.

The resulting SNOM image is shown in Fig. 4.5(c). Although the ratio between the power coupled into the excitation tip and the detected power from the collection tip is below 10^{-12} , the count rates allowed for scanning at moderate speed (around 10 ms/point) to get a

⁵These results were published in Ref. [141].

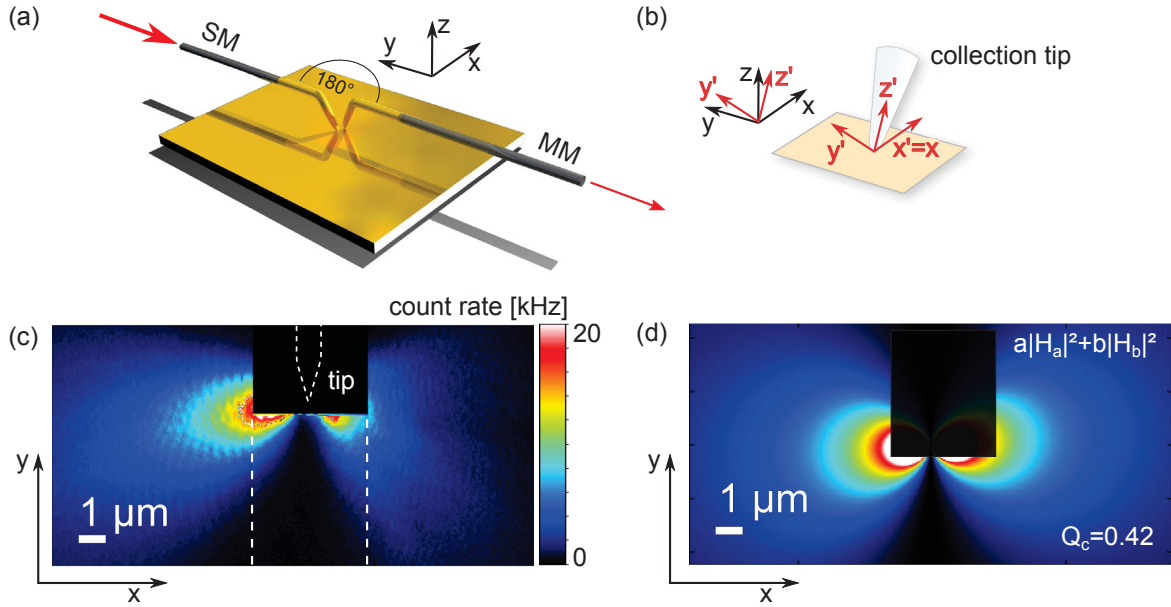


Figure 4.5: (a) Dual-SNOM setup in the “parallel” configuration, for measuring the SPP excitation pattern of an aperture tip. The two bent SNOM tips are placed above an unstructured gold film, on which SPPs propagate from the excitation tip to the collection tip. (b) Visualization of the collection tip’s coordinate system (x, y', z') , which is tilted versus the sample coordinate system by 30° in the $y - z$ -plane, so that z' is parallel to the tip axis. (c) Measured collection-mode SNOM image of the SPPs excited on the homogeneous gold film by the excitation aperture SNOM tip. The excitation tip is located in the region indicated by the black rectangle near the upper edge of the image, and its fiber axis is along the y -axis of the image (see the dashed outline). The image is assembled from several smaller scans, as indicated by the white dashed lines. (d) Simulated Dual-SNOM image, assuming that the excitation tip acts as a point dipole source for SPPs and the collection tip (with MM fiber) is sensitive to the components of the magnetic field which are perpendicular to the tip axis, i.e., $H_{x'}$ and $H_{y'}$. The experimentally determined polarization sensitivity Q_c and angle θ have been used to calculate the relative contributions a and b of the field components H_a (corresponding to a polarization along θ) and H_b (corresponding to the polarization orthogonal to θ ; see text for details). The shadowed rectangle symbolizes the area not accessible to scanning in Fig. 4.5(c).

good contrast in the images. The two lobes in the image clearly resemble a plasmonic dipole pattern. This finding corresponds to the plasmonic aperture emission patterns recorded by leakage radiation microscopy by Hecht et al.[149].

For comparison, a simulated corresponding SNOM image is shown in Fig. 4.5(d). To calculate its intensity distribution, the electromagnetic fields of SPPs excited by a magnetic point dipole oriented along the y direction were calculated using a formula derived by Rotenberg et al. in Ref. 150, thus modeling the excitation process. In a second step, the collection process was modeled, by assuming that the polarization sensitivity of the collection tip is the same for the previously measured far-field case and the near-field case here. This way, also the relative contributions of the different polarization components in the near-field measurement process can be obtained. In the model, the electromagnetic field components E_a, H_a , which correspond to light polarized along θ , contribute more strongly to the image than the field components E_b, H_b which correspond to light polarized perpendicular to θ . The intensity was calculated according to $I \propto a|H_a|^2 + b|H_b|^2$. The relative contributions a and b were derived from the known polarization sensitivity $Q_c = 0.42$.⁶

The resemblance of the calculated image [Fig. 4.5(d)] to the measurement [Fig. 4.5(c)] suggests that the excitation tip can indeed be modeled as a dipole source which excites SPPs. The dipole orientation matches the far-field polarization of light emitted by the tip. Fig. 4.5 constitutes the first published near-field mapping of the unperturbed dipole emission pattern of an aperture SNOM tip.⁷

Another Dual-SNOM measurement of SPPs excited by an aperture tip was performed with the “perpendicular” setup [cf. Fig. 4.1(b)] depicted in Fig. 4.6(a)]. In this configuration, only three “quadrants” can be scanned by the collection tip, since the fourth quadrant is obstructed by the illumination tip. For this measurement, a different tip, but also fabricated from a MM fiber, was used for collection. Unfortunately, the polarization sensitivity and the preferential direction θ of this tip have not been measured during the lifetime of the tip. The measured signal [Fig. 4.6(c)] exhibits three visible lobes which extend diagonally from the excitation tip’s location towards three corners of the image. Although the fourth quadrant could not be mapped due to the geometric constraints of the setup, it is reasonable to assume a fourfold symmetry of the pattern.

At first sight, this result does not match the dipole interpretation of Fig. 4.5. However,

⁶The spatial distributions of the transverse magnetic fields match the electric ones, i.e., H_x could be replaced by E_y and H_y by E_x without changing the resulting images.

⁷In a similar experiment with straight silver-coated aperture tips on a planar silver film, Fujimoto et al.[170] observed a radially symmetric emission pattern. They explained this result by describing the tip as a “randomly polarized” source.

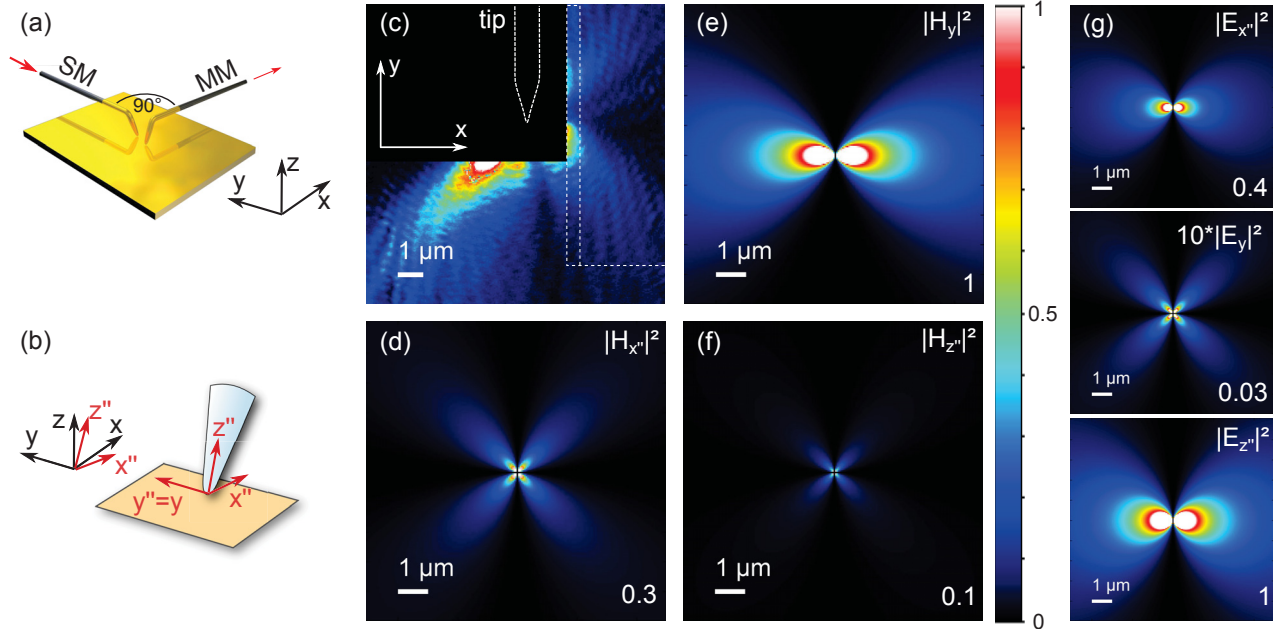


Figure 4.6: (a) Dual-SNOM setup in “perpendicular” configuration with a single-mode fiber tip for excitation, a multi-mode fiber tip for collection, and an in-plane angle of 90° between the tips. (b) Visualization of the collection tip’s coordinate system (x'', y, z'') , which is tilted versus the sample coordinate system by 30° in the xz -plane, so that z'' is parallel to the tip axis. (c) Measured collection-mode SNOM image of SPPs excited by an aperture SNOM tip on a homogeneous gold film. The excitation tip is located in the black rectangle near the top edge of the image, its fiber axis is along the y -axis of the image (see dashed outline). The shown image is assembled from several smaller images, indicated by white dashed lines. The maximum of the color scale corresponds to a photon count rate of approximately 10 kHz. (d)-(f) Simulated intensity maps, assuming that the excitation tip acts as a point dipole, visualize the different magnetic field components with respect to the collection tip’s coordinate system. The three images share the same color scale. (g) Simulated intensity maps visualizing the different components of the electric fields. The three images share a common color scale. The field component along y' is so weak that the corresponding intensity map has been multiplied by 10 to make the pattern visible. The numbers in the lower right corners of all simulated images (e)-(g) are mean intensities (on relative scales) corresponding to the respective field component.

this is only an apparent mismatch. This cleared by comparing the measured image to near-field distributions of the different components of the H -field with respect to the collection tip's coordinate system (x'', y, z'') , which is rotated around the y -axis such that the z'' -axis is parallel to the collection tip's axis. In Fig. 4.6(d)-(f), calculated intensity images are shown assuming the same excitation dipole as in Fig. 4.5(d). Each panel shows an intensity distribution, assuming that only a single component of the magnetic field contributes to the detection process. It becomes apparent that the x'' - and z'' -components of the calculated magnetic field show a fourfold symmetry like the measurement, whereas the y -component shows a two-fold symmetry. The common color scale of the three panels and the relative intensities indicated by the numbers in the lower right corners illustrate that the y'' -components is considerably stronger than the other two components. It should be noted that while the SPPs don't possess a magnetic field along z (perpendicular to the sample plane), the projection of the x -component onto the tilted z'' -direction results in the non-vanishing z'' -component. The total intensity $I = |H_{x''}|^2 + |H_y|^2 + |H_{z''}|^2$ (not shown) is dominated by the y -component and has a two-fold symmetry [cf. Fig. 4.6(e)]. Therefore, the fourfold symmetry in the measured pattern can only be understood as a result of polarization filtering by the collection tip, whose inherent polarization sensitivity appears to act as a polarization filter in the detection path and eliminates the strong influence of the H_y -component, so that the four-fold symmetry of $H_{x''}$ shows in the measured image.

Unlike the magnetic field, the electric field of the SPPs has a strong z -component. As it contributes to both $E_{z''}$ and $E_{x''}$ in the tilted coordinate system, the polarization-filtering effect becomes even more evident when considering the electric field components [Fig. 4.6(g)].

To summarize this finding, the three-lobe pattern in the SNOM image [Fig. 4.6(c)] indicates that practically only the field components $E_{y''}$ and $H_{x''}$ contribute to the detected image. These field components correspond to a single linear polarization. It appears that the specific tip used for collection constitutes an efficient polarization filter in the detection path, such that the measured image constitutes a cross-polarization measurement of the plasmonic dipole pattern. More specifically, we claim that the metalized bend of the tapered fiber acts as an analyzer (cf. Chapter 2.3.)

While the polarization-filtering is an additional effect which has to be taken into account when interpreting SNOM images obtained with a bent tip, and which makes the interpretation more complex, it could also be advantageously used for polarization-resolved measurements. In comparison to the insertion of a polarizer in front of the detector, an

advantage of the proposed technique is the fact that here, the filtering occurs close to the aperture. Therefore, polarization-mixing in the fiber does not lead to a degradation of the polarization contrast.

On the other hand, our far-field measurements of polarization sensitivity (Chapter 2.3) revealed that the mean polarization sensitivities are relatively low, with $\langle Q_c \rangle = 0.4$ for the 7 MM tips and with $\langle Q_c \rangle = 0.7$ for the 7 SM tips that were characterized. As these measurements were done in the far-field regime, one cannot directly conclude that exactly the same values determine the near-field characteristics of the tips. However, several experimental results presented in this thesis suggest a strong correlation between the near-field and far-field polarization properties of the tips. Specifically, the experiments of probing the plasmonic aperture emission with a bull's eye grating (Chapter 2.4) and of directly mapping the SPPs with a second aperture tip (Figures 4.5 and 4.6) corroborate this assumption.

In Chapter 7, as an application example, we present Dual-SNOM measurements of plasmonic modes on gold strip waveguides. In measurements using several different excitation tips, with angles θ either close to 0° or 90° , it turned out that in order to excite the plasmonic modes, the orientation of the waveguides had to be such that the dominant orientations of the waveguide modes' electric and magnetic fields matched the field orientations corresponding to the preferential far-field polarization along θ .

To complement the two measurements displayed in Figures 4.5 and 4.6, which exhibit clear symmetries, two additional measurement results are shown in Fig. 4.7(b) and (c), again obtained with the “parallel” Dual-SNOM configuration. The sample consisted again of an unstructured, planar gold film. In contrast to the earlier experiments, MM tips were now used both for illumination and for collection. None of the tips has been characterized in the far-field, which makes this a “blind” experiment to test the dipole hypothesis. The two images (b) and (c) have been obtained with the same tips and in the same configuration, the only difference in the setup being the polarization of the incoupled beam, which was turned by 45° between both measurements. Even though the measured images look quite different and don't exhibit any obvious symmetry, they can nevertheless be reproduced by slightly expanding the simple dipole model.

In contrast to the calculations presented above, the excitation tip is now represented by two superposed dipoles which are orthogonal to each other and lie in the aperture plane of the excitation tip. The inclusion of a second dipole accounts for the fact that light emitted

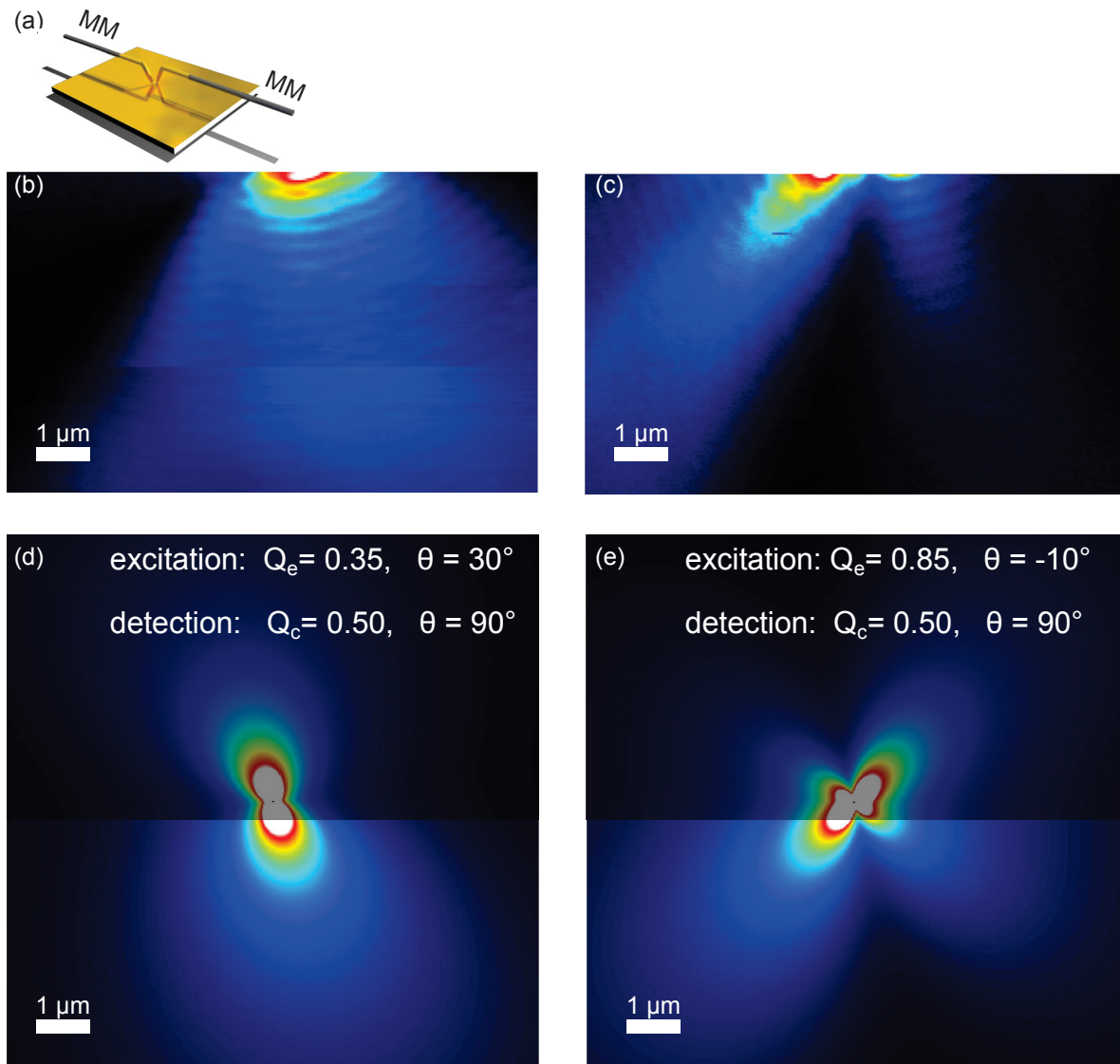


Figure 4.7: (a) Dual-SNOM setup used for recording the images shown in (b) and (c). (b) Dual-SNOM image recorded with a particular polarization of the beam coupled into the excitation tip. (c) Dual-SNOM image recorded with the same setup and the same tips, with a different polarization of the incoupled beam. (d) Calculated image, based on a dipole model. The (assumed) polarization parameters used for the calculation are indicated in the upper half of the image. These parameters have been chosen so that the resulting image resembles that in (b). The shadowed area symbolized the area which was not mapped in (b). (e) Calculated image, assuming only different parameters for the excitation, as indicated, to be compared to the image in (c).

by MM fiber tips is generally elliptically polarized [cf. Chapters 2.3 and 2.4]. The strength and the relative phase of the dipoles determine the values θ and Q_e of the excitation tip.

After calculating the electromagnetic fields of SPPs excited on the gold surface by these dipoles, the detection process is modeled in the same way as above (Fig. 4.5), i.e., the collection tip is sensitive to the magnetic fields which are parallel to its aperture plane. The component of the H -field along a preferential direction θ contributes more strongly to the detected signal than the component perpendicular to θ . This polarization sensitivity is described by the value Q_c .

By iteratively trying different values of the excitation dipole strengths (and their relative phase), of the polarization sensitivity Q_c of the collection tip and of its preferential direction θ , parameter sets were found which qualitatively reproduce the measured images. The calculated images, along with the tip parameters used in the calculations, are shown in Fig. 4.7(d) and (e). With the exception of the value $Q_e = 0.85$ used to generate the pattern in Fig. 4.7(c), the assumed values of Q_e and Q_c are consistent with the values determined in the far-field in Chapter 2.3. The MM tip whose far-field emission was studied in Chapter 2.3 achieved a degree of polarization of only 0.35. The relative large degree of polarization $Q_e=0.85$ can be seen as a further indication of the large differences between individual tips.⁸ The collection tip's parameters are the same for both images, while the excitation tip's parameters differ between both images. This reflects the fact that by changing the polarization of the incoupled beam, the excitation conditions were changed, whereas the detection path remained unchanged.

The experiments presented here, utilizing a planar gold film as one of the simplest conceivable samples, highlight the strong influence of polarization properties on SNOM and Dual-SNOM measurements. Even with such a simple sample, surprisingly complex results were achieved. The inherent polarization sensitivity differs from tip to tip and can be influential enough to permit mapping of selected components of the near-field. The analysis of the intrinsic polarization characteristics of the measurement process, as well as the development of a collision-prevention mechanism, form important prerequisites for the use of Dual-SNOM to characterize other structures, as we have shown here in detail.

⁸It should be noted that collection-mode measurements of the polarization sensitivity Q_c , which was statistically studied in chapter 2.3, generally don't permit inference on the degree of polarization of emitted light, which depends on the polarization of the incoupled beam.

Chapter 5

SNOM mapping of Airy plasmons

An interesting example of aperture SNOM, as introduced in Chapter 2, is the mapping of Airy plasmons by collection-mode SNOM.

Airy plasmons are beams of surface plasmon polaritons (SPPs) with transverse profiles resembling an Airy function. They have a number of remarkable properties: They represent a diffraction-free solution to the paraxial Helmholtz equation, which means that the transverse intensity profile is preserved and does not broaden within a certain propagation distance. Furthermore, the beam follows a parabolic trajectory, which is often described as “self-accelerating” behavior. If an obstacle is introduced into the beam’s path, the intensity profile reconstructs itself (“self-healing”). These properties make Airy plasmons fascinating research subjects and promising candidates for a multitude of applications, e.g., in optical signal processing or in particle manipulation on metallic surfaces. Being SPPs, the electromagnetic fields of Airy plasmons decay exponentially away from the surface, so they cannot be observed by far-field microscopy. By collection-mode SNOM, we succeeded in mapping and quantitatively analyzing the properties of Airy plasmons.

It is well known that generally, optical beams undergo diffractive spreading as they propagate. For a free-space Gaussian beam, the divergence angle is proportional to the ratio between the wavelength and the diameter of the beam waist. For non-broadening propagation, the beam waist diameter would have to approach infinity - effectively, one would obtain a plane wave. Indeed, plane waves are diffraction-free solutions of the wave equation, because their transverse “profile” remains constant upon propagation. By the interference of two plane waves, a \cos^2 transverse intensity pattern is created which also remains constant upon propagation[176]. However, apart from being an idealized theoretical

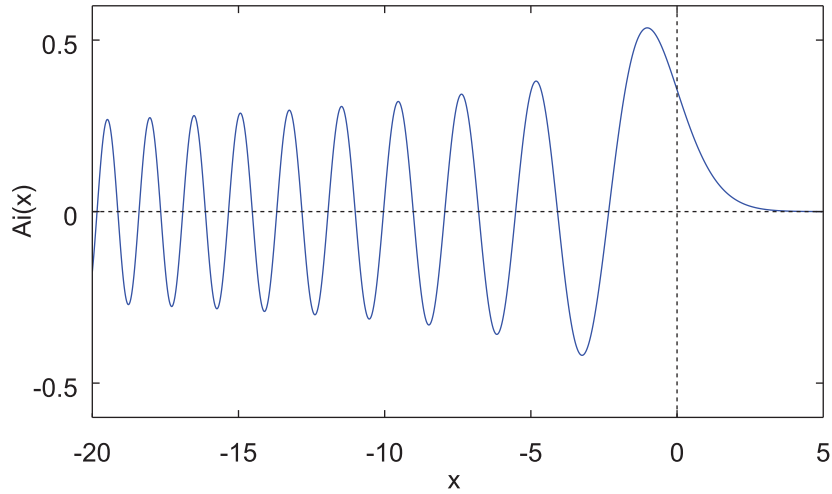


Figure 5.1: The Airy function $Ai(x)$ in the interval $[-20\ 5]$.

concept, plane waves don't qualify as beams, because they don't exhibit a narrow central maximum.

The first - and probably most prominent - realization of diffraction-free optical beams were Bessel beams, which were proposed and experimentally realized by Durnin et al. in 1987[177, 178]. The intensity profile of an ideal Bessel beam corresponds to a zero-order Bessel function of the first kind. As the Bessel function is not square-integrable, such an ideal Bessel beam, like an ideal plane wave, carries infinite energy and is therefore not experimentally accessible. It has been shown, however, that even a Bessel beam which has been truncated by an aperture closely resembles an ideal Bessel beam over a certain propagation distance[177, 178].

In (2+1)D, several classes of non-diffracting beams have since been found[176, 179–186], e.g., Mathieu beams, Weber beams and Airy beams. Like Bessel beams, most of these beams are inherently three-dimensional. Therefore, they cannot be realized in the form of a (1+1)D SPP beam (also called “plasmonic beam”), which is restricted to a metal surface and therefore has to have a one-dimensional transverse profile. In 2010, Salandrino and Christodoulides proposed the Airy plasmon as a non-diffracting surface wave[187]. Already in 1979, Berry and Balazs had recognized that the Airy function describes the only non-spreading wavepacket solution of the one-dimensional, potential-free Schrödinger equation:[188]

$$i\hbar\frac{\partial}{\partial t}\Psi(x, t) = \frac{-\hbar^2}{2m}\nabla^2\Psi(x, t) \quad (5.1)$$

As the potential-free Schrödinger equation (equation 5.1) and the paraxial Helmholtz equation (equation 5.2) are isomorphic, Airy plasmons are diffraction-free as long as the paraxial approximation holds.

$$ik \frac{\partial}{\partial z} A(x, y, z) = -\frac{1}{2} \nabla_T^2 A(x, y, z) \quad (5.2)$$

∇_T is the transverse Nabla operator. The time t in the Schrödinger equation corresponds to the z coordinate in the paraxial Helmholtz equation.

As the Airy function is infinitely extended and not square-integrable, it has to be exponentially apodized or truncated in experimental realization. This reduces the diffraction-free propagation to a limited propagation range, in analogy to the characteristics of a truncated Bessel beam. Salandrino and Christodoulides[187] found the following analytical expression for the amplitude $A(x, z)$ of the apodized Airy plasmon in xz -plane:

$$\begin{aligned} A(x, z) = & Ai \left[\frac{x}{x_0} - \left(\frac{z}{2k_z x_0^2} \right)^2 + i \frac{az}{k_z x_0^2} \right] \exp \left[i \left(\frac{x + a^2 x_0}{2x_0} \frac{z}{k_z x_0^2} - \frac{1}{12} \left(\frac{z}{k_z x_0^2} \right)^3 \right) \right] \times \\ & \times \exp \left[a \frac{x}{x_0} - \frac{a}{2} \left(\frac{z}{k_z x_0^2} \right)^2 \right]. \end{aligned} \quad (5.3)$$

Here, a defines the exponential apodization of the beam profile, $2x_0$ is the width of the main lobe, k_0 is the wave number in free space, $k_z = k_0(\varepsilon_d \varepsilon_m / (\varepsilon_d + \varepsilon_m))^{1/2}$ is the z -component of the SPP's wave vector, and ε_d and ε_m are relative permittivities of dielectric and metal, respectively. This solution is valid as long as the paraxial approximation holds, i.e., as long as $x_0 \gg \lambda$. For $a = 0$, i.e., for a (hypothetical) Airy plasmon without apodization, equation 5.3 reduces to

$$A(x, z) = Ai \left[\frac{x}{x_0} - \left(\frac{z}{2k_z x_0^2} \right)^2 \right] \exp \left[i \left(\frac{x}{2x_0} \frac{z}{k_z x_0^2} - \frac{1}{12} \left(\frac{z}{k_z x_0^2} \right)^3 \right) \right]. \quad (5.4)$$

The argument of the Airy function in equation 5.4 indicates that the main lobe follows a parabolic trajectory in the xz -plane.

Almost simultaneously with two other groups, we were able to generate and observe¹ Airy plasmons for the first time, in 2011[189–191]. Our experimental results are re-described in Chapter 5.1. We used a specially designed grating for excitation of the Airy plasmon and

¹idea and simulations: A. Minovich, D. Neshev; experiment: A. E. Klein, N. Janunts

collection-mode SNOM for near-field imaging. Li et al.[190] generated Airy plasmons by first exciting a SPP plane wave by a periodic grating and then using a non-periodic nanocave array, which diffracts the SPP wave so that two Airy plasmons are formed by interference on both sides of the nanocave array. The Airy plasmons were analyzed by leakage radiation microscopy. Zhang et al.[191] first created a one-dimensional free-space Airy beam with the help of a spatial light modulator, which acted as a cubic phase mask, and an objective which acted as a Fourier transformer. The Airy beam was then transformed into a plasmonic beam by a grating coupler. By varying the positions of the Gaussian input beam, the objective or the spatial light modulator, they were able to dynamically modulate the path of the Airy plasmons. Like Li et al.[190], they used leakage radiation microscopy to observe the Airy plasmons. The collection-mode SNOM mapping of an Airy plasmon allowed us to quantitatively compare its properties to simulated values.

In another publication[192], we demonstrate the generation of a bright plasmonic “hot-spot” by two interfering Airy plasmons excited by two diffraction gratings, which may be useful for applications like surface optical tweezing or biosensing. A review on Airy plasmons is given in Ref. [193].

Beyond the paraxial approximation, different non-broadening, self-bending beams have been found in the recent years[184, 185, 194]. Also, by the superposition of two SPP plane waves, plasmonic interference patterns which do not broaden over a certain propagation distance have been demonstrated[195, 196].

5.1 Generation and near-field mapping of Airy plasmons

For generating Airy plasmons, two main obstacles have to be overcome: free-space light has to be coupled to surface plasmons, and the transverse profile of the plasmonic wave has to match an Airy function. As the momentum of SPPs of a given frequency ω is larger than that of free-space light at that frequency (i.e., the dispersion relation of SPPs lies to the right of the light line), an index mismatch has to be compensated to excite SPPs[9]. This can be achieved by using a prism in the Kretschmann[197] or Otto[198] configuration. The illuminating beam undergoes total internal reflection inside the prism, and at a specific reflection angle the evanescent wave at the prism surface excites SPPs on the interface between a metal film and air. The metal film is either evaporated onto the prism (Kretschmann configuration), or it is separated from the prism by a narrow air

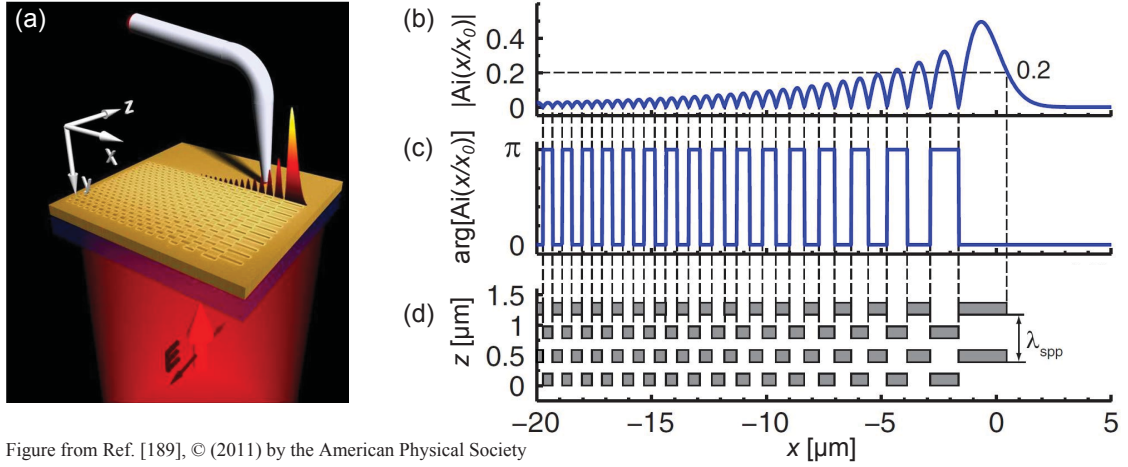


Figure from Ref. [189], © (2011) by the American Physical Society

Figure 5.2: (a) Schematic of the experimental setup for excitation and near-field mapping of Airy plasmons. A broad, polarized laser beam illuminates a specially designed diffraction grating, which generates plasmonic beams with Airy-like profiles propagating along the $+z$ and $-z$ directions. The near-field at the sample surface is mapped with a cantilevered aperture SNOM tip. (b) Amplitude of the Airy function $Ai(x/x_0)$ with $x_0=0.7 \mu\text{m}$. (c) Phase of the Airy function. (d) Layout of the diffraction grating. $\lambda_{\text{SPP}} = 764 \text{ nm}$ denotes the SPP wavelength.

gap (Otto configuration). Another method is to use a grating which provides the required momentum for plasmon excitation[199].

By the use of a specially designed grating, we can excite SPPs and imprint the required phase distribution at the same time[189]. The grating [see Fig. 5.2(d)] was fabricated on a 150 nm thick gold film deposited on a glass substrate by DC sputtering. A focused ion beam (FIB FEI Helios 600) was used to completely remove the gold layer from the areas of the rectangular slits which form the diffraction pattern. In z direction, the pattern has a periodicity of $\lambda_{\text{SPP}} = 764 \text{ nm}$, which corresponds to the SPP wavelength at a free-space wavelength of 784 nm. The filling factor is 0.5. Thus, SPPs propagating along the z direction are excited when the grating is illuminated by a laser with a free-space wavelength of 784 nm under normal incidence. In x direction, the grating is divided into columns, the edges of which are determined by the zeros of the Airy function $Ai(x/x_0)$ with a main lobe half width x_0 of 700 nm (cf. equation 5.3). As the Airy function asymptotically approaches zero for positive arguments, another criterion had to be applied to determine the x -dimension of the widest (=first) column. Numerical tests showed that the optimum output is generated when this slit is truncated at the 0.2 level of the Airy function. Every second column is shifted by half a period ($\lambda_{\text{SPP}}/2$) along the z direction, which corresponds to a phase delay

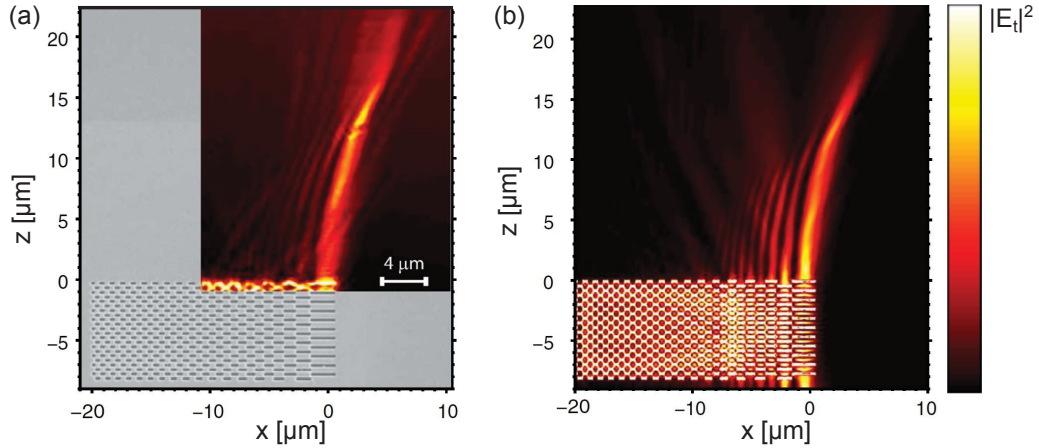


Figure from Ref. [189], © (2011) by the American Physical Society

Figure 5.3: (a) Collection-mode SNOM image of the plasmonic near-fields, overlaid on a scanning electron micrograph of the excitation grating. (b) Numerically calculated distribution of $|E_t|^2 = |E_x|^2 + |E_y|^2$ at the metal-air interface.

of π . In this way, the phase distribution of the Airy function [see Fig. 5.2(c)] is imprinted onto the plasmonic beam. No special measures have been taken to additionally reproduce the amplitude distribution of the Airy function. Potentially, this could be achieved by tuning the z -dimensions of the slits.

The fabricated grating consists of 33 columns (in x -direction) and 11 periods in z -direction. It was illuminated from below by a z -polarized diode laser with a free-space wavelength of 784 nm. The beam was collimated and then weakly focused to generate a spot size of around 200 μm on the sample, so that the grating, with dimensions of around 20 μm x 8.5 μm, was homogeneously illuminated. We imaged the optical near-fields of the Airy plasmon excited by the grating on the gold surface by collection-mode SNOM (Nanonics MultiView 4000). The gold-coated, cantilevered fiber tip had an aperture diameter of 150 nm.

Fig. 5.3(a) shows the detected SNOM image, overlaid on a scanning electron micrograph of the grating. The self-accelerating property of the beam is evident, as the main lobe follows a bent trajectory. A transverse (x) displacement of more than two widths of the main lobe is attained before the beam is damped by the plasmonic losses. The main lobe retains its narrow profile over a propagation distance of around 20 μm. A quantitative analysis of these parameters is given in Fig. 5.4. Overall, the detected image resembles the FDTD simulation shown in Fig. 5.3(b), which shows the distribution of $|E_t|^2 = |E_x|^2 + |E_y|^2$. While in reality, the contributions of the different components of the electromagnetic field

to the detected image may be more complex (cf. Chapter 4), this does not affect the image in the case of the Airy plasmon, as here, like in a plasmonic plane wave, all field components either vanish or are proportional to E_y [187].

Apart from the curved trajectory and non-broadening main lobe, one can also observe the self-healing property of the beam profile in the SNOM image [Fig. 5.3(a)]. After a propagation distance z of around $12\ \mu\text{m}$, the main lobe passes an obstacle on the sample surface, which was also observed in the simultaneously acquired topography image (not shown). While the profile and the intensity of the main lobe show some considerable modulation at the location of the particle, the main lobe appears to regain its original width and intensity after a propagation distance of only a few μm , as the main lobe is re-constituted by light diffracted from the other lobes.²

The good quality of the SNOM image allowed us to quantitatively compare the measured intensity distribution to numerical and analytical predictions, and thereby, to confirm the Airy-like characteristics of the plasmonic beam. In Fig. 5.4(a), the measured values of the main lobe's deflection are plotted and compared to the analytical solution, i.e., under paraxial conditions, to the deflection of an apodized Airy beam propagating under non-paraxial conditions[200], and to the numerical simulation shown in Fig. 5.3(b). After some initial variations ($z < 5\ \mu\text{m}$), the experimental values follow a smooth trajectory which closely matches the numerically simulated one. Both these trajectories – the experimentally measured one and the numerical solution – resemble the non-paraxial solution. This means that even though the profile of our plasmonic beam is truncated, and its amplitude does not exactly match the Airy function, its main lobe deflection still corresponds well to that of an apodized Airy plasmon under non-paraxial conditions. The analytical, paraxial solution deviates from the other three curves, as the paraxiality condition ($x_0 \gg \lambda$) is not fulfilled for the beam under consideration ($x_0 = 700\ \text{nm}$, $\lambda_{\text{SPP}} = 764\ \text{nm}$).

Fig. 5.4(b) shows the evolution of the main lobe's width as the beam propagates. An ideal Airy beam, under paraxial conditions, does not broaden and keeps its initial width of $2x_0 = 1.4\ \mu\text{m}$. Realistic Airy-like beams, which are either apodized or truncated, maintain their intensity profile over their so-called diffraction-free propagation range, after which they quickly spread [indicated by the gray areas in Fig. 5.4(a) and (b)]. In our case, this diffraction-free propagation distance is around $15\ \mu\text{m}$. The beam width of the experimentally

²It should be noted that the SNOM image does not easily permit an estimation of how much the plasmonic propagation was disturbed, because the particle in question could also lead to a topographic artifact. Therefore, even if the beam remains undisturbed, an irregularity might be observed in the SNOM image at the position of the particle.

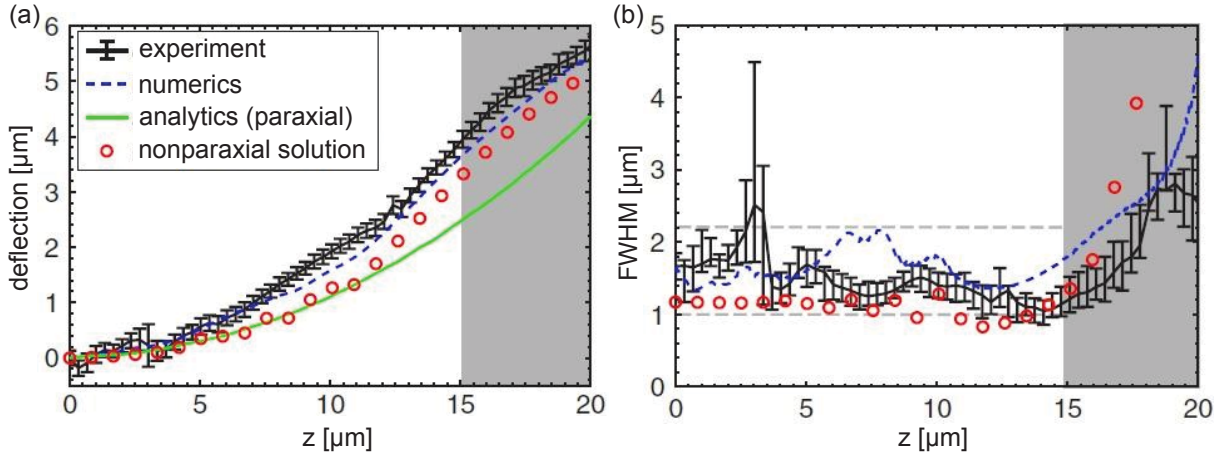


Figure from Ref. [189], © (2011) by the American Physical Society

Figure 5.4: (a) Deflection of the main lobe's peak in dependence of the propagation distance. (b) Full width at half maximum of the main lobe in dependence of the propagation distance. Black symbols: experimental data, blue dashed line: numerical simulation (FDTD), red symbols: nonparaxial solution, green line [only in (a)]: analytical solution.

generated Airy plasmon strongly fluctuates within the first 5 μm of propagation. These fluctuations represent the influence of some extra-radiation, which is not part of the Airy plasmon and which represents the imperfection of our scheme. This extra-radiation quickly spreads due to diffraction, so that it is less noticeable in later stages of beam propagation. After this initial propagation stage, the main lobe maintains its narrow width of below 2 μm for a propagation distance of more than 10 μm [Fig. 5.4(b)].

In summary, we have demonstrated the generation of an Airy plasmon on a gold surface. By mapping the optical near-fields with collection-mode SNOM, the main characteristics of the Airy plasmon, namely, non-diffracting propagation within the diffraction-free propagation range, self-acceleration, and self-healing after a disturbance. The SNOM measurement permitted quantitative comparisons of the beam deflection and beam width with analytical and numerical models.

In the meantime, it has been shown that the trajectories of grating-generated Airy plasmons can be controlled by linear optical potentials[201, 202]. Free-space Airy beams and self-bending beams have been used for micromachining along a curve[203] and for particle manipulation[204, 205]. Free-space Airy beams with a radially symmetric profile exhibit abrupt autofocusing[206, 207], which can be used for particle trapping and guiding[205]. Due to their fascinating properties and their ability to guide light along a curved path on

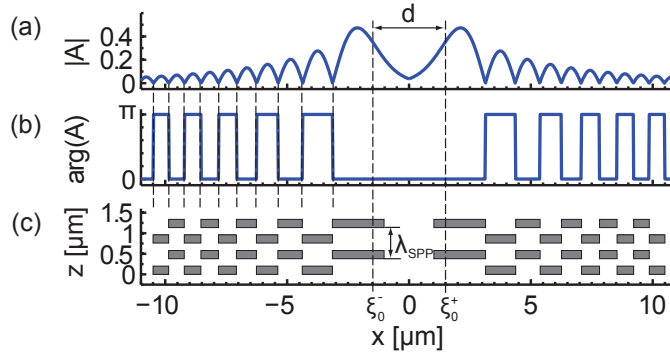


Figure 5.5: Grating geometry for the generation of interfering Airy plasmons. (a),(b) Absolute value and phase of the desired profile of the two Airy plasmons. ξ_0^- (ξ_0^+) denotes the x -coordinate where the function argument of the left (right) Airy function becomes zero (cf. Fig. 5.1). (c) Grating geometry for excitation of Airy plasmons. $\lambda_{\text{SPP}} = 764$ nm denotes the SPP wavelength. The distance between the gratings, d , is measured between ξ_0^- and ξ_0^+ .

a surface, Airy plasmons are promising candidates for applications in plasmonic circuitry, biosensing and in particle manipulation on surfaces[208].

5.2 Interference of Airy plasmons: plasmonic hot-spots

In analogy to the abrupt autofocusing of radially symmetric Airy beams observed in free space,[206, 207] the interference of two mirror-symmetric Airy plasmons creates a plasmonic hot-spot on the metal surface[192]. Its position and brightness can be varied by using different excitation grating geometries, or by tilting the illuminating laser beam with respect to the sample normal. Plasmonic hot-spots whose positions can be varied may find applications in various areas, like biosensing or surface optical tweezing. Previously, plasmonic hot-spots generated through spatial coherent control have been demonstrated,[209, 210] and were recently applied in a novel microscopy method based on scanning a plasmonic hot-spot over the surface under investigation[211].

To generate a plasmonic hot-spot by interference of two Airy plasmons, we combine two gratings in a mirror-symmetric layout on a common sample [see Fig. 5.5]. Each of the gratings resembles the grating described in Chapter 5.1. In order to fabricate both gratings within one writing-field of the focused ion beam, the excitation gratings in this configuration are shorter along the x direction and comprise only 10 columns per grating. Both gratings are simultaneously illuminated by a weakly focused laser beam ($\lambda_0 = 784$ nm,

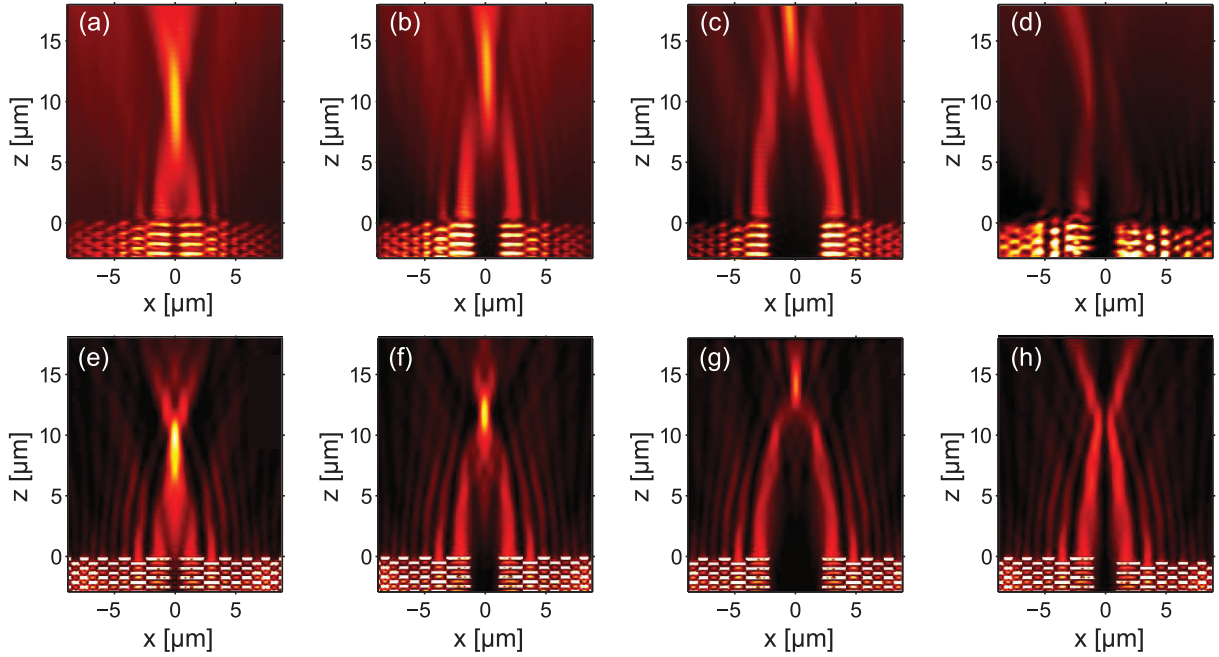


Figure 5.6: Plasmonic near-field distributions of interfering Airy plasmons for different separation distances d between both gratings: SNOM images [(a)-(d)] and FDTD calculations of $|E_t|^2$, where E_t is the component of the electric field parallel to the sample plane, evaluated 10 nm above the sample surface [(e)-(h)]. Separation distances: $d = 1.5 \mu\text{m}$ [(a),(e)], $d = 3.0 \mu\text{m}$ [(b),(f)], and $d = 5.0 \mu\text{m}$ [(c),(g)]. (d),(h) were obtained for a separation distance $d = 2.5 \mu\text{m}$ and a z -shift of half a grating period.

spot size $\approx 50 \mu\text{m}$). Each of the gratings excites a (truncated) Airy plasmon, and the parabolic trajectories of both main lobes intersect on the symmetry axis. By the constructive interference of the main lobes, a bright hot-spot is generated.

In Fig. 5.6, SNOM images [(a)-(c)] of the generated interference patterns and corresponding FDTD simulations [(e)-(g)] are presented for a series of mirror-symmetric grating patterns featuring different distances d between both gratings. As the distance between the gratings increases, the bright spot shifts upward along the symmetry axis. Due to losses and self-acceleration of the main lobes, the size and intensity of the hot-spot vary. According to the FDTD simulations, for a distance d of $3.0 \mu\text{m}$ between the gratings the intensity of the hot-spot is 2.5 times higher than the illumination intensity [Fig. 5.6(f)]. While the simulations predict a hot-spot with FWHM sizes of only $0.5 \mu\text{m}$ (along x) by $1.5 \mu\text{m}$ (along z), the hot-spots appear more extended in the SNOM measurements, particularly along the

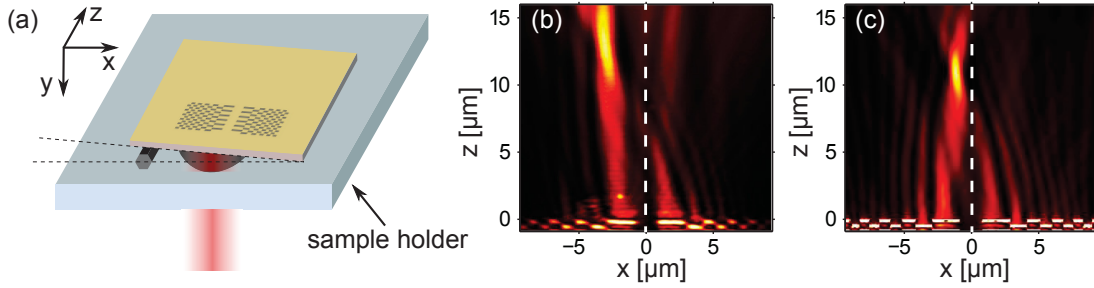


Figure 5.7: Introducing an angle between the illumination beam and the sample makes the hot-spot shift sideways. (a) Schematic of the experimental setup. (b) SNOM image for tilted illumination at $\alpha = 5.3^\circ \pm 0.3$, for $d = 2.5 \mu\text{m}$ (c) Tangential component of the electric field ($|E_t|^2$) calculated by FDTD. The dashed lines mark the sample's symmetry axis.

z direction. We suspect that this broadening is due to the finite resolution of the SNOM and due to the influence of the SNOM tip on the SPP propagation.

While variations of the distance d between both gratings preserve the mirror-symmetry of the configuration and make the hot-spot shift along the symmetry axis, shifting one grating along the z direction breaks the symmetry and gives rise to a phase difference between the two Airy plasmons. Depending on the value of this phase shift, the brightness of the spot varies. For a phase shift of π , obtained by shifting one of the gratings by half a period, the bright spot completely disappears [see Fig. 5.6(d),(h)] due to destructive interference of both main lobes. According to our simulations, the spot reappears when the shift is increased to a whole grating period, corresponding to a phase shift of 2π . At phase shifts which are not integer multiples of π , the interference pattern is not mirror symmetric. An animation of the simulated interference patterns for continuously increasing phase shifts is available as supplementary material to Ref. 192.

With regard to applications, it is of particular interest to dynamically shift the position of the hot-spot, e.g., to address or manipulate particles on the surface. An easy way of shifting the spot is to tilt the illuminating beam sideways, or equivalently, to tilt the sample [see Fig. 5.7(a)]. This breaks the mirror-symmetry and introduces a momentum k_x , resulting in a sideways shift of the hot-spot. For a grating with a separation distance $d = 2.5 \mu\text{m}$, we measured a lateral shift of $3.0 \mu\text{m}$ for an illumination angle $\alpha = 5.3^\circ \pm 0.3^\circ$ [see Fig. 5.7(b)]. This is the calculated angle at the glass/gold interface, taking into account the refraction at the air/glass interface of the substrate rear side. Remarkably, the shifted spot maintained a lateral FWHM (along x) below $1 \mu\text{m}$. FDTD simulations predict a

lateral shift of only $1.3\ \mu\text{m}$ for an illumination angle $\alpha = 5^\circ$, and a lateral shift of $2.3\ \mu\text{m}$ for $\alpha = 10^\circ$. As a phase gradient along x is introduced by illuminating the grating at an angle, the beam profile gradually deviates from the desired Airy profile, which does not exhibit such a gradient. This sets an upper limit to the realizable illumination angles.

The possibility to generate either single plasmonic Airy beams, or mirror-symmetric plasmonic Airy beams which form a plasmonic hot-spot by interference of the two main lobes, was convincingly detected by collection-mode SNOM. The presented scheme for the generation of plasmonic hot-spots is simpler than schemes based on coherent spatial control[209, 210], and in contrast to hot-spots created with the help of nanoantennas, the sample surface does not need to be structured in the close vicinity of the bright spot. Along with the opportunity to dynamically shift the hot-spot by tilting the illumination beam, the concept may be useful for plasmonic circuitry applications, surface optical tweezers, optical data storage, and biosensing.

Chapter 6

Mapping whispering-gallery modes in fused silica microresonators

6.1 Introduction

Dielectric microresonators can store light in so-called whispering-gallery modes (WGM), i.e., modes which are located near the edge of a resonator[212–214]. In such a resonator light travels in a high-index dielectric and undergoes repetitive total internal reflections under oblique incidence angles at the interface to the surrounding medium, which has a lower refractive index. The resonance condition is fulfilled if after a round-trip, the wave interferes constructively with itself. Some of the most common types of optical microresonators are those of spherical, cylindrical and toroidal shape.

Microresonators are used in a variety of applications such as biosensing[215–217], cavity quantum electrodynamics[218–220], all-optical switching[221], as laser resonators[222–224] and for the generation of optical frequency combs[225, 226]. Depending on the fabrication and material quality, high quality factors of up to 10^9 can be achieved. For the imaging of WGM, different methods have been described in literature: A microscope can be used to detect light that is scattered from the resonators, e.g., by surface defects[227]. While this method is easy to implement, it suffers from a very low resolution. This method could be improved by using erbium-doped disks, in which a 3-photon fluorescent up-conversion process converts some of the light from the infrared into the visible spectral range, leading to a higher resolution of the images, as the diffraction limit scales proportionally to the wavelength[228]. With these far-field microscopy methods, the nodes and anti-nodes of the standing-wave pattern could not be resolved. Especially for studying the mode symmetries

in sets of coupled resonators, the standing-wave pattern can serve to distinguish different mode symmetries[229, 230]. Therefore for the investigation of coupled resonators, high-resolution SPM techniques are better suited than far-field microscopy for the investigation of the modes.

Early SPM investigations of WGMs were done by collection-mode SNOM[231–233] and were capable of resolving the nodes and anti-nodes of the standing-wave pattern which is formed by the interference of a WGM and its degenerate, counter-propagating mode. Another SPM method is to use a conventional scattering-SNOM technique, i.e., an AFM tip is placed on the resonator as a scatterer and the scattered light is detected in the far-field[234].

Within the scope of this thesis, three different SPM methods to map WGM in fused silica microresonators were explored in collaboration with colleagues. Some of our results are also reported in references 229, 230 and 151. The first method (section 6.2) is collection-mode SNOM¹, which has also been used for the measurements reported in Chapter 5. Additionally, two alternative SPM methods were developed, which improved the resolution and the sensitivity of the measurements: In the scattering-based method (section 6.3), a sharp SPM tip scanning over the resonator surface modifies the transmission and reflection signals measured at the tapered fiber which is evanescently coupled to the microresonator and serves to excite the WGM.² Lastly, we employed thermocouple-probe microscopy[151] (section 6.4), which has been discussed in Chapter 3, to map the intensity distributions of WGM³. All measurements presented in this chapter were performed with the MV-4000 SPM system from Nanonics Imaging Ltd.

6.2 Collection-mode SNOM

Our first experiments were aimed at mapping the intensity distributions of WGMs in spherical microresonators. These microresonators were produced by heating an optical fiber with a CO₂-laser and pulling both ends apart, so that the fiber breaks. Surface tension leads to the formation of a sphere or ellipsoid which stays attached to the fiber. The resonators we studied had diameters varying between 40 μm and 200 μm. With the help

¹sample fabrication and WGM excitation setup: Thomas Käsebier, Carsten Schmidt; SNOM measurements: Angela Klein, Carsten Schmidt (spherical microresonators), Mattes Liebsch (disk microresonators)

²measurement setup: Angela Klein, Mattes Liebsch, Carsten Schmidt; measurements: Mattes Liebsch; theoretical description: Carsten Schmidt, Mattes Liebsch

³measurement setup: Angela Klein; measurements: Mattes Liebsch; data analysis: Angela Klein; FEM simulation (optical): Carsten Schmidt; FEM simulation (thermal): Angela Klein

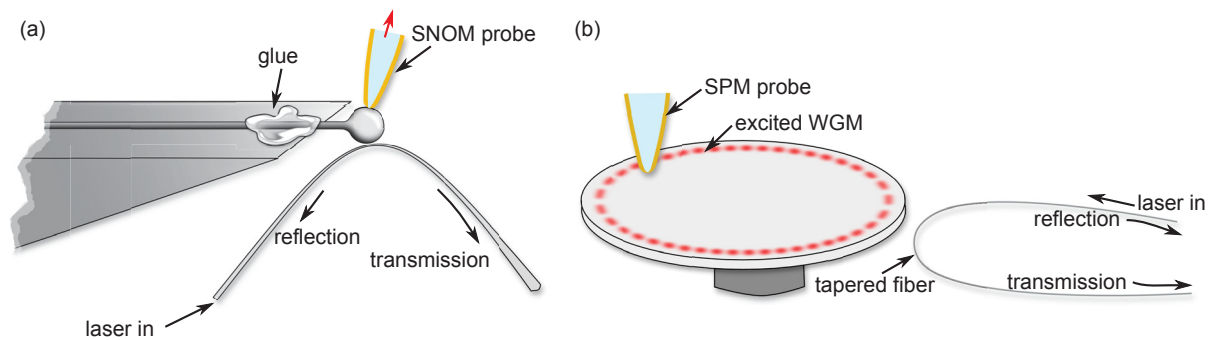


Figure 6.1: (a) Schematic of the setup for the excitation and collection-mode SNOM mapping of WGM in spherical microresonators. (b) Schematic of the setup for the excitation and SPM-mapping of WGM in microdisk resonators.

of a microscope and UV-curable glue, the fiber was mounted onto a holder so that only a very short piece of fiber ($< 100 \mu\text{m}$), holding the microresonator, protruded over the edge [see Fig.6.1(a)]. We found that if the protruding fiber is too long, it is not possible to land an SPM tip on the sphere and do a topographic scan, because the elastic fiber lets the sphere evade sideways or downwards. For obtaining a mechanically stable experimental configuration which permitted to scan the sphere surface, it was necessary to optimize the gluing procedure, as well as the SPM's feedback and approach parameters. WGMs were excited by evanescent coupling from a tapered fiber loop[235] which was placed below the sample. As an excitation light source for all microresonator experiments, we used a tunable continuous-wave laser operating in the spectral range around 1550 nm (81640A, Agilent). The optical signals were detected by InGaAs photoreceivers (TIA-525I, Terahertz Technology). By observing the transmission and reflection through the excitation taper while sweeping the excitation laser wavelength, the resonance wavelengths at which WGMs are excited were found. For SNOM mapping, the laser wavelength was fixed at one of the resonances, thus exciting a specific mode of the microresonator. The collected SNOM signal was measured with a photodiode detector. We mapped intensity distributions of different modes in spherical microresonators by scanning the tip over the microresonator surface. Two examples of measured intensity distributions, overlaid on topographic maps, are shown in Fig. 6.2(a). The multitude of bright bands in the intensity distributions indicates that higher-order modes were excited, which feature many intense rings instead of a single high-intensity band. As the microresonators are not exactly spherical, their

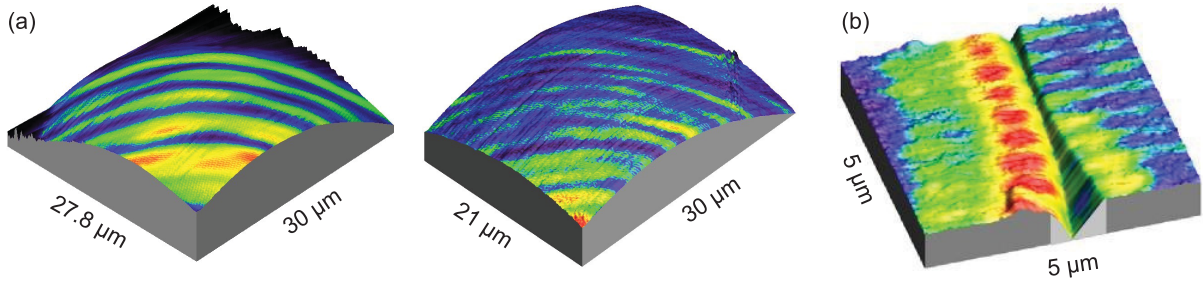


Figure 6.2: (a) Collection-mode SNOM measurements of WGM in spherical silica microresonators, overlaid on topographical maps of the samples. The z axis has been rescaled to emphasize the surface curvature. (b) Collection-mode SNOM measurement of WGM in the contact region between two microdisk resonators, overlaid on the topographic map. The edges of the cylindrical disks appear slanted, due to the finite extension speed of the tip's z piezo and the feedback mechanism.

geometrical parameters were only approximately known, and the resonance wavelengths and near-field images could not be assigned to individual mode numbers.

Another microresonator design are cylindrical microdisks, which can be produced by lithographic methods[227, 229]. The geometrical parameters of microdisks can be precisely controlled, which makes it easier to assign the resonances to individual modes. Typical microdisk diameters are in the range of 30 μm to 40 μm. The precisely controllable positions and diameters of such microdisks make it possible to fabricate and study ensembles of resonators coupled via their evanescent near-fields[227]. At the same time, their planar surfaces and fixed positions on a substrate facilitate SPM studies. In analogy to the SNOM measurements of WGMs in spherical microresonators, we mapped WGM in coupled microdisks by collection-mode SNOM. A schematic of the setup is shown in Fig. 6.2(b). In contrast to the measurements on spherical resonators, the nodes and antinodes of the standing-wave pattern could be observed in these measurements. An example of such a measurement, which represents the contact region of two near-field coupled microdisks, is shown in Fig. 6.2(b).

A relatively large tip (aperture diameter: 250 nm) had to be used to obtain a sufficient signal in this wavelength range. The large tip disturbed the modes so much that higher-order radial modes, with several intensity maxima along the disk radius, could not be observed.

6.3 Scattering-based SNOM

As an alternative to collection-mode SNOM, we developed a customized scattering-based measurement method for the investigation of microdisk resonators. A sharp, gold-coated tip (Nanonics Imaging Ltd.) with an apex diameter of ≈ 80 nm was used to scan the microresonator surface. Like the SNOM tips in the previous investigations, the tip was fabricated by heating and pulling a silica fiber to obtain a tapered, bent tip, which was then metal-coated and can be used for topography measurements as an atomic force microscopy (AFM) tip. The tip is fully compatible with the SNOM setup, and while the metal coating leads to a large apex size in comparison with conventional AFM tips, it is still much smaller than the NIR wavelengths used in the measurements on microresonators. In comparison to the SNOM tips, the AFM tip is sharper, the metal coating is thinner and it does not have an aperture. Unlike in conventional scattering-SNOM measurements, we did not collect the light that was scattered into the far-field. Instead, we made use of the changes the tip introduces in the system's resonance properties. We described this method and the theoretical background in detail in Ref.[229, 230]. The method is related to previous works by other groups where the influence of a scattering tip on the transmission of a waveguide[236] or a photonic crystal microcavity[237] was used for optical imaging.

Mode maps of WGM were obtained by recording the transmission or the reflection through the excitation taper as a function of the scanning tip's position [see Fig. 6.2(b)]. For a better signal-to-noise ratio, the transmission and reflection signals were demodulated by a lock-in amplifier (SR830, Stanford Research Systems) locked to the tip's oscillation frequency. Figure 6.3 shows maps of the demodulated "transmission" and "reflection" signals ("amplitude" output of the lock-in amplifier) obtained while scanning over the gap region of two closely spaced microdisks which are coupled via their evanescent fields. The mode position is clearly visible in both images. The reflection image shows better contrast, while the transmission image appears more blurred in comparison. Along the two arc-like features which represent the position of the mode in each of the disks, a regular succession of maxima and minima indicates the position of nodes and antinodes. As the nodes and antinodes extend across the gap between the disks, one can conclude that the disks are symmetrically coupled.

Conspicuously, the perturbation by the tip can lead to either increased or decreased values of the reflection signal, when compared to the "background" signal level which is measured when the tip is not within the mode volume. This constitutes a clear difference between the "reflection" image and the collection-mode SNOM image shown in Fig. 6.2(b).

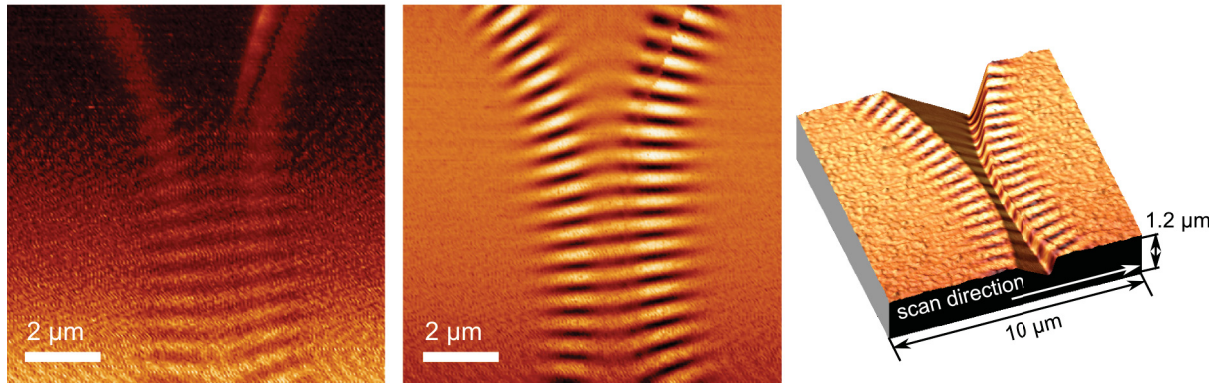


Figure 6.3: Images of WGM in two coupled microdisk resonators, obtained by scanning an AFM tip over the contact region between both disks and recording the transmission and reflection through the excitation taper. (a) Transmission image. The two arc-like features indicate the mode position near the edges of the disks. (b) Reflection image. Within the arcs which indicate the mode position, strong maxima and minima occur. The “background” signal level (when the tip is not within the evanescent fields of the mode) is between the maximum and minimum levels which occur within the arc. (c) Reflection image, overlaid on the simultaneously recorded topography image. The finite extension speed of the z piezo and the feedback mechanism cause the disk edges to appear slanted.

The “collection” signal never drops below the background level as long as the tip is close to the disk edge, i.e., within the mode volume. This is strong evidence that the “reflection” and “transmission” mode maps do not constitute simple intensity maps of the WGMs. In our experiments, the presence of the metal-coated tip in the evanescent field region of WGMs has two main effects: Due to the high refractive index of the tip coating, the effective refractive index of the surrounding medium and therefore the resonance wavelength of the mode change. Secondly, the tip acts as a scatterer which leads to additional coupling between the WGM and its degenerate, counterpropagating mode and also to coupling to radiative modes. The excitation strength of the WGM and its counterpropagating, degenerate mode both influence the transmission and reflection through the excitation taper. Therefore, the “reflection” and “transmission” maps reflect the influence of the scanning tip on the WGMs in a non-trivial way. To understand the image formation, the microdisks (i.e., a single disk or several coupled ones) and the excitation taper were modeled by a coupled-mode theory. The tip was taken into account by introducing a Rayleigh scatterer[229, 230]. This model accurately predicts the typical features of mode maps and their spectral variations. By comparing experimentally obtained mode maps with such calculations, the actual electromagnetic fields can be inferred.

The blue arrows in Fig. 6.3(a) and (b) indicate regions where strong topographic artifacts are present: Due to the peculiar geometry of the microdisk sample, which exhibits a height drop of around $10\ \mu\text{m}$ at the disk edge, the tip is not able to accurately follow the surface topography while it is scanned along the x axis at constant lateral speed. The tip's actual path and the origin of the artifact can be obtained from Fig. 6.3(c): As the tip is scanned over the edge of the left disk, it loses contact to the surface and consequently moves downwards. The speed of this downwards motion is determined by the maximum extension speed of the z piezo and by the parameters of the feedback loop. As soon as the tip gets into contact with the right disk - as the tip apex is below the disk surface and the disk has a vertical edge, this contact happens between the disk edge and the tip shaft - the tip moves upwards. This upwards motion also happens with finite speed, leading to another slanted edge in the topography image. Depending on the feedback parameters, it may overshoot before the tip apex reaches the surface of the second (right) disk, and follows its surface topography for the rest of the scanning line. As long as the tip moves upwards and the tip shaft is in contact with the disk edge, it acts as scatterer of the WGM, therefore it also influences the "reflection" and "transmission" signals.

6.4 Thermal SPM

6.4.1 Measurements

The third near-field mapping method which we employed for mapping WGMs is scanning thermocouple-probe microscopy, which has been discussed in Chapter 3. A thermocouple tip featuring a gold-platinum contact at its apex is scanned over the sample surface, and a map of the apex temperature is recorded. Originally, we intended to use scanning thermocouple-probe microscopy to study the disk temperature. However, it turned out that the tip is predominantly heated by light absorption, not by heat transport from the disk towards the tip (see section 6.4.2).

Figure 6.4(a) shows a thermovoltage map of a WGM in a microdisk resonator, overlaid on the topographic map of the sample. Near the rim of the disk, a bright ring is observed, which marks the localization of the WGM. The thermovoltage map resembles collection-mode SNOM images of WGM in microdisk resonators [cf. Fig. 6.2(b)], indicating that the near-field intensity can be mapped by the thermocouple probe. As a WGM and its counterpropagating, degenerate mode co-exist, a standing-wave pattern is formed. The nodes and antinodes of this standing-wave pattern can be distinguished in the thermovoltage

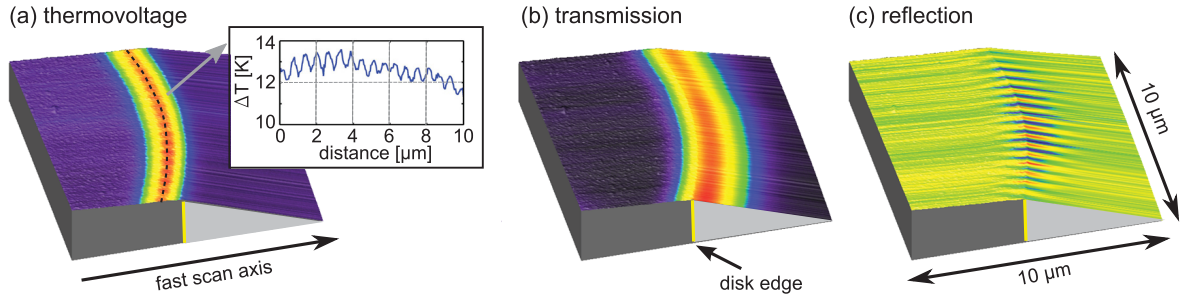


Figure 6.4: Synchronously obtained images of a microdisk resonator: (a) thermovoltage, (b) transmission and (c) reflection through the excitation taper. All mode maps have been overlaid on a topographic map of the sample.

image as local intensity minima and maxima within the bright ring, which indicates a spatial resolution of at least $\lambda_{\text{eff}}/4 \approx 310$ nm.

While scanning the disk with the thermocouple probe, we simultaneously recorded the thermovoltage map and transmission [Fig. 6.4(b)] and reflection [Fig. 6.4(c)] maps, as described above (Chapter 6.3), for comparison. Here, the transmission image does not show the nodes and antinodes of the standing-wave pattern, presumably because the thermocouple tip is much larger than the AFM tip used for the measurement in Fig. 6.3. While the thermovoltage map [Fig. 6.4(a)] shows the standing wave as a ring inside the disk, at the inner part of the rim, the transmission [Fig. 6.4(b)] and reflection [Fig. 6.4(c)] signals appear at the disk edge. The maximum of the transmission signal even appears on the sloped area, i.e., when the tip apex is not on the disk surface. This shift can be attributed to the topographic artifact of the scattering method which was described above: The tip acts as an efficient scatterer when it is near the edge of the disk, so that the apex is already off the edge, moving downwards, and the metalized conical shaft is next to the disk edge, penetrating the mode volume. As the topographic map represents the positions of the tip apex, this results in the observed images with the maximum signal “outside” the disk area. The thermovoltage image reproduces the temperature of the tip apex, and so in the corresponding image [Fig. 6.4(a)], the maximum intensity is recorded on top of the disk. It represents the real mode position with respect to the topographic image.

In our collection-mode measurements on microdisk resonators (Chapter 6.2), we found that it was impossible to excite and map higher-order radial modes, because the large aperture tip strongly disturbed the modes. With a thermocouple probe, we succeeded in mapping microresonator modes of higher radial order. Fig. 6.5 shows the thermovoltage

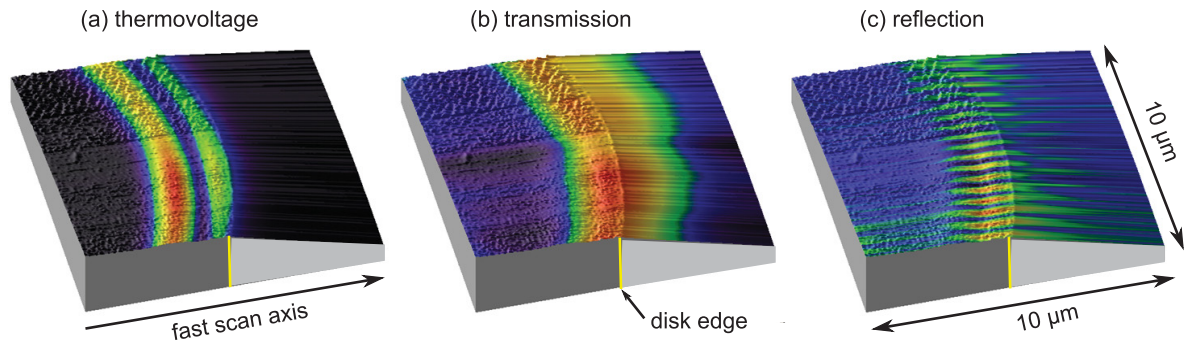


Figure 6.5: Synchronously measured maps of a WGM with two radial maxima, overlaid on the topographic image. (a) Thermovoltage, (b) transmission and (c) reflection through the excitation taper.

image of such a mode with two radial maxima, overlaid on the simultaneously obtained topographic map of the sample. The radial maxima are clearly visible as concentric rings near the disk edge. This proves that in comparison to collection-mode SNOM measurement, the thermocouple measurement is highly sensitive, while disturbing the mode to a lesser extent. The nodes and antinodes along the rings are not distinguishable in the thermocouple measurement. Although the signal-to-noise ratio is good in the transmission and reflection images, they do not show the two clearly separated rings indicating the higher-order mode.

An interesting feature in Fig. 6.5 is that in the topography measurement, slight bulges appear near the disk edge, at the position of the WGM [most clearly visible in Fig. 6.4(c)]. It looks as if the disk surface was not completely flat. The bulges coincide with the bright rings of the thermovoltage image. In reality, the disk surface is flat, and the apparent bulges are due to influences of the optical fields on the topographic measurement. Such crosstalk could either be due to optical forces on the tip[152, 153, 238], or due to heating of the tip, which might change its oscillation characteristics, thereby interfering with the feedback mechanism.

Having demonstrated that the thermovoltage images resemble intensity maps of the optical modes, we proceed to discuss the physical mechanism of thermal mode mapping. Two different effects lead to heating of the thermocouple tip when it is within or close to the mode volume of the WGM: Firstly, as the mode's evanescent optical fields extend into the air above the disk, the tip penetrates the evanescent fields while scanning above the disk. The metallic tip coating is heated by absorption. Secondly, the fused silica disk heats up due to absorption[239] when WGM are excited. As the tip-sample distance is in the nanometer range, heat conduction from the disk surface to the tip can also lead

to tip heating. Radiative and convective heat transfer from the disk to the tip have been estimated to be negligible in comparison to heat conduction. To elucidate the tip heating mechanism, both the intensity distribution and the temperature distribution inside and around a microdisk were modeled by a finite element method (Comsol Multiphysics). By comparing the radial profile of a measured thermovoltage image with the calculated intensity and temperature profiles, we show that the thermovoltage image represents the light intensity at the disk surface, rather than the temperature. This means that light absorption by the tip contributes stronger to the tip's heating than heat conduction.

6.4.2 Simulations

We used the finite element method (Comsol Multiphysics) with an axisymmetric geometry to calculate the intensity and temperature distributions associated with a WGM. The resonator was modeled as a $1\ \mu\text{m}$ thick fused silica disk with a radius of $20\ \mu\text{m}$ which is connected to a silicon substrate by a $4\ \mu\text{m}$ thick and $7\ \mu\text{m}$ high cylindrical silicon pillar. The resonator is surrounded by air. First, an optical eigenmode is found by a simulation with a fine grid comprising only a small region around the microresonator, surrounded by perfectly matched layers. To obtain the associated temperature distribution, we simplified the geometry of the heat source by representing the mode volume by a toroid with elliptical cross section. The toroid surface represents the contour at which the calculated optical intensity has dropped to half of its maximum value. A pump power of $\approx 1\ \text{mW}$ in the tapered fiber is estimated to correspond to an absorbed power of $\approx 100\ \mu\text{W}$, and to a homogeneous heating of the toroidal mode volume with $1\ \text{MW cm}^{-3}$. The temperature at the boundaries of the simulation volume (a cylinder with a diameter of $100\ \mu\text{m}$ and a height of $100\ \mu\text{m}$) is set to $300\ \text{K}$. Figure 6.6(a) shows the resulting temperature distribution, calculated in steady state and based solely on heat conduction. The maximum temperature increase inside the mode volume is around $8.5\ \text{K}$. This value is consistent with previous calculations and experiments with optical excitation powers (at the taper input) in the milliwatt range[239]. In Figure 6.6(b), the calculated profiles of the optical intensity and the temperature at a height of $20\ \text{nm}$ above the disk surface [dashed line in Fig. 6.6(a)] are compared to the thermovoltage profile, obtained in a measurement with an excitation laser power of $4\ \text{mW}$. All curves have been normalized, so that they could be plotted in the same diagram. The maximum thermovoltage value corresponded to a temperature increase of $13.9\ \text{K}$. The thermovoltage profile as well as the simulated intensity profile of the WGM exhibit a pronounced, narrow peak (FWHM= $1.1\ \mu\text{m}$) above a flat background.

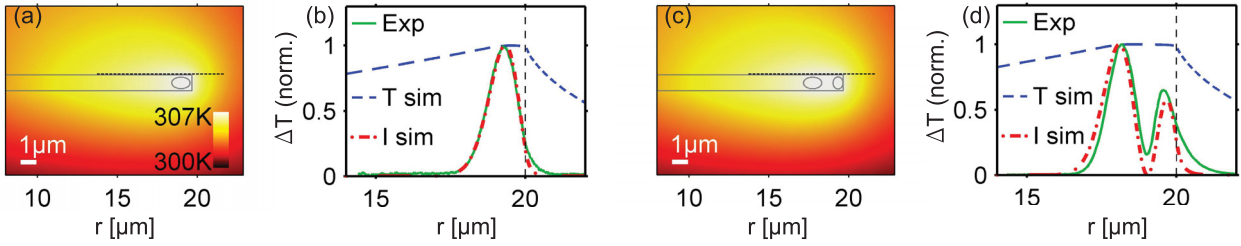


Figure 6.6: (a) Axisymmetric finite element simulation of the temperature distribution within and around a microdisk resonator. (b) Comparison of radial profiles of the simulated temperature (blue dashed line), the simulated optical intensity (red dash-dotted line) and the measured temperature signal (green line) along the dashed line in (a). All profiles have been normalized to the range between 0 (background signal/ambient temperature) and 1. The vertical dashed line marks the disk edge. (c) Simulation of the temperature with excitation of a mode with two radial maxima (cf. Fig. 6.5). (d) Same as in (b), but for the higher-order mode shown in (c).

The simulated temperature profile, in contrast, exhibits only a very flat maximum and decreases smoothly towards the center and towards the disk edge. These features of the three curves lead us to the conclusion that the recorded thermovoltage map is indeed a map of the optical intensity, and not a map of the disk's surface temperature.

To further corroborate this claim, we do the same comparison for a higher-order radial mode [cf. Fig. 6.5(a)], which exhibits two radial maxima [Fig. 6.6(c)-(d)]. Here, the mode volume is represented as two elliptical toroids, the edges of which represent the contour at which the simulated optical intensity has dropped to half of its maximum value. The two peaks corresponding to the two toroids are clearly distinguishable in the thermovoltage profile as well as in the simulated optical intensity profile, whereas they blur into a single, broad feature in the simulated temperature profile. The two maxima are hardly discernible. The thermovoltage and intensity profiles exhibit a striking resemblance.

We conclude that in our experimental configuration, absorptive heating of the tip outweighs heat conduction from the disk to the tip. Therefore, the recorded thermovoltage images constitute maps of the light intensity. In comparison to aperture SNOM tips, thermocouple tips can be manufactured with smaller apex sizes while maintaining a sufficient signal/noise ratio. Good optical contrast can be achieved while disturbing the mode pattern to a lesser extent than in our aperture SNOM measurements. On the other hand, both evanescent and propagating fields contribute to tip heating. Thermocouple tips are not able to distinguish both contributions, whereas other methods (e.g., scattering SNOM) succeed to primarily detect evanescent fields. Therefore, the thermocouple SPM

method is particularly adapted to applications where the near-fields of interest are not superimposed by strong propagating fields. Possible applications of thermocouple-probe near-field microscopy include plasmonic waveguides or photonic crystals. In Dual-SNOM measurements the optical excitation is realized by an aperture tip and therefore, the near-fields of interest are not superimposed by the field of an illuminating far-field beam. Thus, a thermocouple probe could replace the collection SNOM probe in Dual-SNOM experiments, and the near-field measurement would not be disturbed by propagating fields originating from a far-field illumination scheme.

For each measurement configuration, it has to be evaluated whether tip heating occurs primarily via absorption by the tip coating or by heat transfer from the sample to the tip, which would result in thermal rather than optical maps. In metallic samples, light is efficiently absorbed by both the sample and the tip. The thin air layer between tip and sample efficiently conducts heat from the sample to the tip [cf. Fig. 6.6(a) and (c)]. Therefore, we estimate that the sample would have approximately the same temperature as the tip (as the light intensity is approximately the same at the sample surface and the tip's position), which would lead to a blending of optical and thermal information. We expect that thermocouple probes are essentially polarization-insensitive. Except for resonance effects, it is straightforward to assume that the absorption efficiency does not depend on the polarization of incident light, which justifies the interpretation of the obtained images as intensity maps.

Overall, each of the three presented methods for the characterization of WGM has its assets and drawbacks: The scattering method has a very high resolution, and the sharp tip used for scattering perturbs the mode spectrum to a lesser extent than the larger tips used for collection-mode SNOM and thermocouple-probe microscopy. Due to the small linewidths of the resonances, this small perturbation by the scattering tip is still sufficient to map WGM even at low excitation powers (below 100 μ W). However, artefacts occur due to mode perturbation by the tip shaft when the tip is near the disk edge. The relation between the obtained images and the intensity distribution at the resonator surface is not trivial, but could be convincingly explained by a model developed by C. Schmidt[229, 230]. With this model, in turn, the actual intensity distributions can be calculated.

In the other two methods, the interpretation of the obtained images is more straightforward, albeit the interaction between the modes and the tip is disregarded. In collection-mode SNOM, the sensitivity is strongly dependent on the utilized tip, that can strongly disturb

the resonator mode under investigation. A compromise has to be found between the required sensitivity and the size of the tip.

In scanning thermocouple-probe microscopy, the tip is typically smaller than in collection-mode SNOM, thus disturbing the mode spectrum to a lesser extent. Further possible advantages are the broad spectral range in which the thermocouple probe can be used, and its insensitivity to polarization. However, at low laser powers, its signal-to-noise ratio was found to be worse than that of the scattering-based method and that of collection-mode SNOM with sufficiently large apertures.

Chapter 7

Characterization of plasmonic waveguides by Dual-SNOM

7.1 Observation of leaky modes in gold strip waveguides

Plasmonic circuitry has been a hot topic within the field of nanophotonics for the last years[14, 83, 240–242], as it promises information processing and transport at high speed and within small devices. In contrast to dielectric waveguides and devices, plasmonic elements can concentrate light in sub-diffraction volumes, which can reduce the geometric footprint of the targeted photonic circuits. To investigate plasmonic devices and waveguides, scanning near-field optical microscopy (SNOM) is widely used, due to its ability to image the optical near-fields at the sample surface.

A common way to excite plasmonic waveguides is direct illumination of the waveguide with free-space light. This method is a rather inefficient way of exciting waveguide modes, and the large illumination spot makes further investigation of the excited modes difficult. By using an antenna, free-space radiation can be converted into plasmonic waveguide modes more efficiently[15]. Alternatively, plasmonic waveguides can be coupled to dielectric ones, which are excited by end-fire or grating coupling[243, 244]. Extended metallic launching pads have been used to first excite surface plasmon polaritons (SPPs) with plane-wave characteristics, which were then used to excite modes in metal strip waveguides extending from the launching pad[164, 167, 245]. With regard to future applications in integrated optical circuits, the integration of light sources – i.e, nanolasers[246, 247] or nanoscale

light-emitting diodes[14] – in the microfabricated sample is a straightforward way to excite plasmonic waveguide modes. However, such integrated light sources drastically increase the complexity of the fabricated sample, which makes them less applicable for the investigation of the waveguide structure itself.

Dual-SNOM can be advantageously used to study plasmonic modes in gold strip waveguides. This way, no additional structures on the sample, like antennas or launching pads, are needed for excitation, and the plasmonic modes can be observed in the near-field regime.

At the same time, the plasmonic waveguides constitute a relatively simple model system suitable for studying and demonstrating the instrumental characteristics of the Dual-SNOM. With respect to the instrumental characteristics, plasmonic waveguides complement the measurements presented in Chapter 4.3. The homogeneous gold film which was used for the first Dual-SNOM investigations described in Chapter 4.3 is translational invariant (within the horizontal plane) and supports a continuum of SPP modes which have the same absolute value of the wavenumber, but propagate in all in-plane directions. The local density of optical states (LDOS), which is often used to describe illumination-mode SNOM[130, 163], is spatially uniform for such a simple sample. In contrast, strip waveguides feature a limited number of guided modes, a discrete k -spectrum, and a non-uniform LDOS. The number of guided modes on a gold strip waveguide depends on the waveguide width. Depending on the waveguide width, one mode or the interference of several modes can be observed in Dual-SNOM experiments. In addition to studying the mode propagation and interference by using the first SNOM tip as a stationary excitation source and performing collection-mode measurements with the second tip, it is investigated how the relative excitation strength of several modes of a multimode waveguide depends on the position of the excitation tip.

The “parallel” Dual-SNOM setup described in Chapter 4 was used for these measurements. For excitation, we used the SM-fiber tip whose far-field emission and detection characteristics were studied in detail in Chapter 2.4 and whose SPP emission pattern is shown in Fig. 4.5. We set the polarization of the incoupled laser beam ($\lambda_0 = 663$ nm) such that the light emitted from the tip’s aperture had a high degree of polarization ($Q = \frac{I_{max} - I_{min}}{I_{max} + I_{min}} = 0.96$, extinction ratio 50:1). The emitted light was mainly polarized along the y direction [Fig.7.1(a)].¹

For collection, we used a MM-fiber tip with a collection-mode polarization sensitivity of $Q_c = 0.42$ – free-space light which is polarized along the y axis generates an approximately

¹The coordinate system used in this chapter differs from the one used in Chapters 2.4 and 4.3. The y -direction corresponds to $\theta = 0^\circ$.

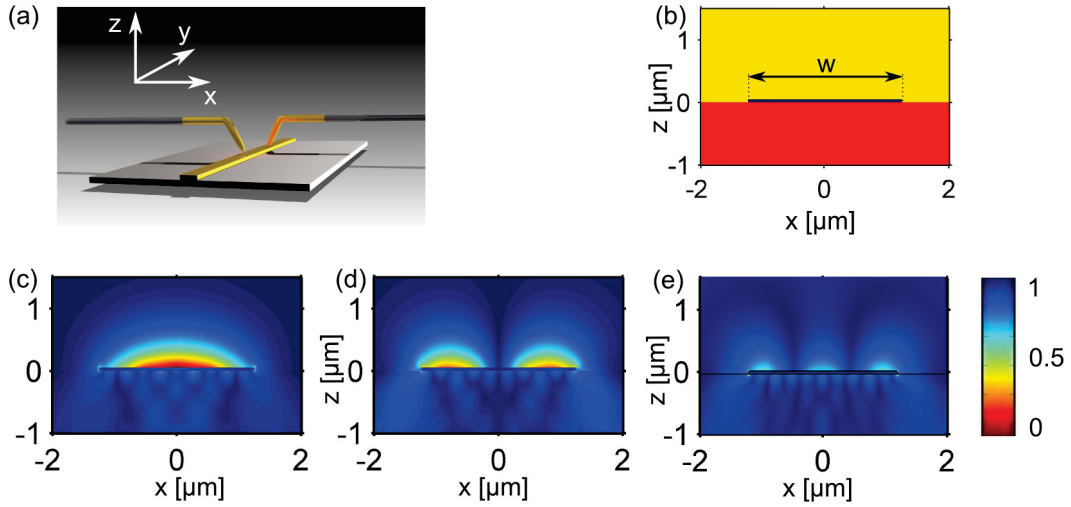


Figure 7.1: (a) Dual-SNOM setup for excitation and near-field mapping of waveguide modes. The excitation and collection tips are both placed on a metal strip waveguide with their fiber axes perpendicular to the waveguide. The excitation tip is kept at a fixed position while the collection tip is raster-scanned over the waveguide to map the optical near-fields. (b) The simulated waveguide geometry in 2D (magnified detail). Red: fused silica, blue: gold, yellow: air. (c) Norm of the electric field of the fundamental leaky mode. (d) Norm of the electric field of the second, antisymmetric leaky mode. (e) Norm of the electric field of the third, symmetric leaky mode.

2.5 times higher detected signal than free-space light which is polarized along the x axis. This tip has also been described in Chapters 2.4 and 4.3. It was connected to a fiber-coupled photon counting module (Perkin Elmer SPCM-AQR).

The excitation tip was kept stationary, while the collection tip was scanned over the sample surface so that it gradually approached the stationary tip [fast scanning axis: x , slow scanning axis: y in Fig. 7.1(a)]. The scan was stopped when shear-force interactions between both tips occurred (cf. Chapter 4.2).

The gold strip waveguides under investigation were fabricated on a fused silica substrate by electron beam lithography. The waveguides are 55 nm thick, 300 μm long and have different widths between 300 nm and 2.5 μm . A titanium adhesion layer with a thickness of less than 5 nm was applied between glass and gold. Such waveguides support two classes of modes: modes mainly localized on the substrate-metal interface and modes mainly localized on the metal-air interface, i.e., on the top surface of the waveguides[248]. The dispersion relations of the metal-air interface modes generally lie between the light line in air and the light line in the substrate, which means that they can couple to far-field radiation inside

the substrate. It is straightforward to assume that in SNOM experiments, we mainly probe these leaky modes on the top surface of the waveguides[165, 248]. Plasmonic edge modes can also exist in such waveguides, but are typically not observed in SNOM measurements[167].

The field profiles and effective mode indices of the leaky waveguide modes were found by a finite element method (FEM) simulation (Comsol Multiphysics, 2D modal analysis). As all the relevant modes are leaky modes, their calculation with numerical methods is considerably more challenging than the calculation of typical bound modes. Some of their energy is radiated into the substrate and, subsequently, into the perfectly matched layers (PML) which surround the simulation volume. This makes it impossible to normalize the modes, and additionally, the imaginary parts of the effective mode indices might deviate from the calculated values.

Depending on the waveguide width, several leaky modes can exist. The relevant modes in our analysis are the fundamental, symmetric mode with a single maximum in the middle of the waveguide, the second mode which is antisymmetric to the longitudinal waveguide axis, and the third mode, which again has a mirror-symmetric field profile.

Figures 7.1(c),(d), and (e) show the electric field norm of these modes in the xz -plane (across the waveguide), for a $2.5\ \mu\text{m}$ wide waveguide. The permittivity of gold was taken from Ref. 148. At close distance above the waveguides, the strongest electric field component is E_z , followed by E_y and E_x . E_x is much weaker than E_z and E_y and has maxima at the waveguide edges. Regarding the magnetic fields, H_x is the strongest component, followed by H_z . H_y is close to zero above the waveguide, with sharp maxima at the waveguide edges. For a waveguide width of $2.5\ \mu\text{m}$, the calculated effective indices are $n_{\text{eff},1} = 1.031 + 0.0073i$ for the fundamental mode, $n_{\text{eff},2} = 1.015 + 0.013i$ for the second mode, and $n_{\text{eff},3} = 0.982 + 0.017i$ for the third mode. The fact that the real part of $n_{\text{eff},3}$ is below 1 means that the cutoff of the third mode happens at a waveguide width slightly above $2.5\ \mu\text{m}$. Modes with effective indices below 1 radiate into the air. However, as we investigate the modes at close distances from the excitation location (see below), such radiative modes might still be observed at the waveguide surface. Also, slight deviations of the fabrication parameters or of the gold permittivity can shift the effective index of the mode. According to our mode analysis, the second mode has a cutoff at a waveguide width of approximately $1.8\ \mu\text{m}$, at which the real part of its effective index becomes 1, whereas the fundamental mode has its cutoff at a waveguide width of around $500\ \text{nm}$.

We excited waveguide modes by placing the excitation tip on a waveguide such that the waveguide runs perpendicular to the fiber axis (i.e., parallel to the polarization of

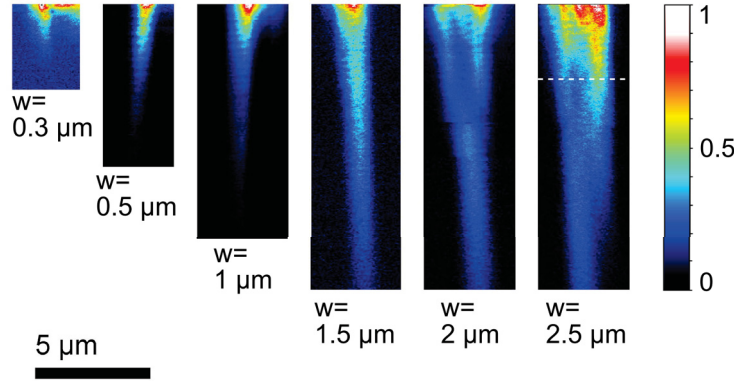


Figure 7.2: SNOM measurement results for plasmonic waveguides with different widths between $0.3\ \mu\text{m}$ and $2.5\ \mu\text{m}$. The scale bar applies to all images. The width of each waveguide is indicated below the respective image. The white dashed line in the rightmost image marks the position of the line scans in the measurement shown in Fig. 7.3.

emitted light, y) and the tip is approximately in the middle of the waveguide profile [see Fig. 7.1(a)]. When turning the waveguide by 90° such that it runs parallel to the fiber axis (x), only very weak signals could be obtained, due to polarization mismatch between the light emitted by the tip and the waveguide modes. The distance between the excitation tip and each waveguide end was chosen large enough to avoid interference effects caused by back-reflection from the waveguide ends. The collection tip was used to obtain SNOM images of the plasmonic field distributions on the waveguide. Fig. 7.2 shows measured intensity distributions of waveguides with different widths w . The images have been slightly cropped at the top to exclude the immediate vicinity of the excitation tip with very high signal levels, where radiative modes and direct tip-to-tip coupling strongly contribute to the measured signal. It is clearly visible that for widths between $0.5\ \mu\text{m}$ and $1.5\ \mu\text{m}$ the fundamental waveguide mode is excited and its propagation distance increases with increasing width. For $0.3\ \mu\text{m}$ wide strips, no propagation could be observed. When the strip width is increased to $2.0\ \mu\text{m}$ or $2.5\ \mu\text{m}$, a mode beating pattern between the fundamental mode and higher order modes can be observed.

Remarkably, for the two broadest waveguides ($w=2\ \mu\text{m}$ and $w=2.5\ \mu\text{m}$), two intensity maxima are clearly visible over a propagation range of over $5\ \mu\text{m}$. The characteristic profile with two maxima (“M-profile”), visible as two bright strips in the 2D-maps, is observed in all our measurements on waveguides which are at least $2\ \mu\text{m}$ wide, including measurements with different tips (not shown here). This “M-profile” suggests that in addition to the fundamental symmetric mode and the first antisymmetric mode, the third

mode is excited and is observed over a certain propagation range. In beating patterns of only the fundamental symmetric mode and the first antisymmetric mode, an “M-profile” can only occur if the excitation coefficient of the antisymmetric mode is higher than that of the fundamental mode. At equal amplitude of both modes, one would see a single maximum towards one edge of the waveguide, as for one half of the waveguide, the fields of both modes interfere constructively and for the other half, destructively. As the excitation tip was placed near the middle of the waveguide for the measurement, i.e., in the antinode of the fundamental mode and the node of the antisymmetric one, one would expect the fundamental mode to be excited more strongly, thus making it improbable that the observed “M-profile” is generated by the antisymmetric mode.

7.2 Investigation of the excitation process

In order to get deeper insight into the relative excitation strength of the three modes, we studied the influence of the excitation tip’s position across waveguide ($w = 2.5 \mu\text{m}$) on the intensity profiles at a fixed distance between both tips. The collection tip was used to repeatedly scan the same line (across the waveguide, at a distance of approximately $6.5 \mu\text{m}$ from the excitation tip) and map the near-field intensity profiles, while the excitation tip’s position was shifted across the waveguide in steps of $\approx 100 \text{ nm}$. At each position of the excitation tip, many line scans of the collection tip were performed and later averaged to reduce noise. In Fig. 7.3, each horizontal line represents the average profile collected for a specific position of the excitation tip. The horizontal coordinate represents the position of the collection tip. As expected, the edges of the plot are dark, indicating that there is no light transmitted from the excitation tip to the collection tip as long as one of the tips is not on the waveguide. The measured pattern resembles a diamond shape, with its upper left segment being weaker than the others. Additionally, an intensity maximum is located at the lower right corner, i.e., when both tips are located at opposite edges of the waveguide. A similar, but less pronounced feature appears in the upper left corner. The complex pattern indicates that the position of the excitation tip has a strong influence on the beating pattern and therefore, on the relative excitation strengths of the individual waveguide modes.

In order to understand the measured pattern, we applied a simple model for the excitation of waveguide modes by the SNOM tip which is based on calculating the overlap integral between the tip’s fields and each of the three considered waveguide mode profiles.

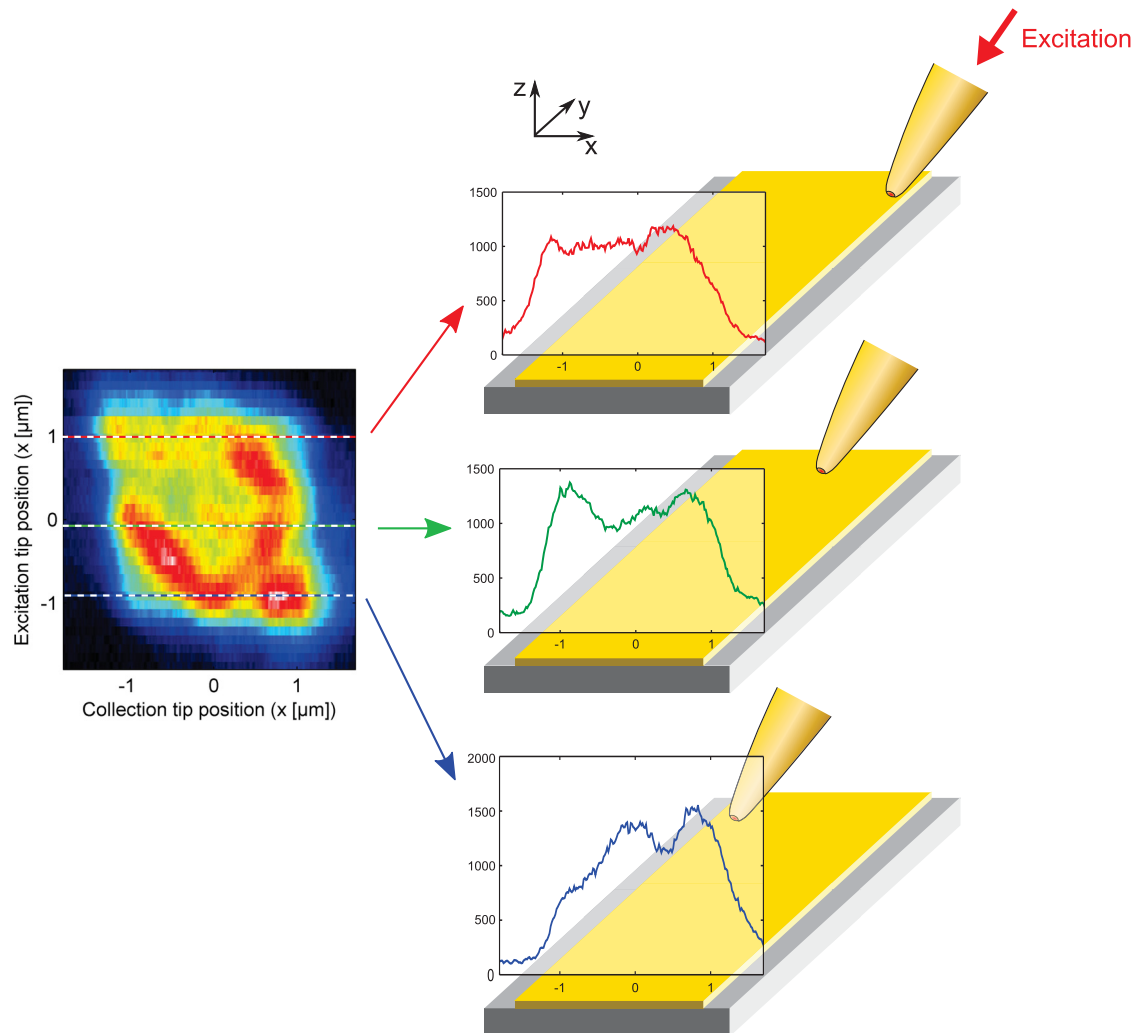


Figure 7.3: Near-field profiles at $\approx 6.5 \mu\text{m}$ propagation distance, measured by shifting the excitation tip across the waveguide ($w = 2.5 \mu\text{m}$) in steps of $\approx 100 \text{ nm}$ and recording the near-field intensity profile (horizontal intensity profiles) with the collection tip. Due to variations of the excitation strength and phase of the two modes on the waveguide surface, the beating pattern and therefore the intensity profile at the collection tip's position changes as the excitation position is varied.

As the results presented in Chapter 4.3 suggest that the excitation tip can be modeled as a magnetic dipole within the tip's aperture plane and perpendicular to the direction θ (here, $\theta = 0$ corresponds to the y direction), we assumed that the waveguide modes are excited via their H_x components. Due to the aperture's tilt, the assumed dipole has also a component along z , but as H_z of the waveguide modes is very weak, this contribution was neglected.

It seems natural to use the numerically calculated waveguide mode profiles for the calculation of the excitation coefficients. However, for this purpose, a proper normalization of the modes is vital. As the modes under consideration are not bound modes, but leaky modes, they cannot be normalized. In the FEM simulations, this is reflected by the electromagnetic field extending to the perfectly matched layers. On the other hand, the simulations suggest that with respect to the fields on the top surface, the strips behave almost like a perfect electric conductor (PEC). Therefore, we simplify the theoretical treatment by assuming trigonometric dependencies of the mode profiles $H_x(x)$. These simplified mode profiles reflect the nodes and the symmetries of the real mode profiles and can easily be normalized.

The spatial profile of the excitation tip was represented by a Gaussian with a FWHM of 200 nm along x (i.e., across the waveguide). Along the propagation direction y , its spatial extension was neglected, i.e., it was assumed to be infinitely thin. The model could potentially be improved by incorporating the field distributions of the tip's eigenmodes, which were recently calculated by Sören Schmidt[108, 128]. Alternatively, one might model the tip as a magnetic dipole, as it is suggested in Chapter 4.3.

For 300 different positions across the waveguide, the overlap between the tip profile and each of the three considered waveguide mode profiles was calculated, resulting in excitation coefficients for each mode and each excitation position. Subsequently, the interference of the modes along the waveguide was calculated, taking into account these excitation coefficients, the simplified mode profiles and the calculated, complex effective indices of the modes. The detection process after a certain propagation length Δy was then modeled by assuming that only the magnetic field component H_x contributes to the detected image. For comparison, we also calculated the resulting intensity distribution if both magnetic field components parallel to the sample surface, H_x and H_z , contribute to the detected intensity according to the collection tip's polarization sensitivity of $Q_c=0.42$ (not shown). For this calculation, the spatial field profiles were extracted from the numerically simulated data 20 nm above the waveguide surface. However, it turned out that the tip's polarization sensitivity did not

significantly influence the appearance of the calculated image. Neither the tip's inclination nor its finite resolution power were taken into account.

Fig. 7.4(a) shows calculated beating patterns on a 2.5 μm wide waveguide for different positions of the excitation tip. As the relative mode content varies, the resulting beating patterns show strong variations. The characteristic "M-profile" is visible when the excitation tip is placed close to the waveguide's symmetry axis (leftmost images).

The calculated image in Fig. 7.4(b) shows the variations of the intensity profile upon variation of the excitation position (x), at a fixed y -distance of $\Delta y = 6.5 \mu\text{m}$ between both tips. Like in Fig. 7.3, the horizontal and vertical axis represent the collection tip's x -position and the excitation tip's x -position, respectively. Two elongated features above and below the secondary diagonal resemble the upper right and lower left edges of the diamond shape that was observed in the measurement (Fig. 7.3). Also, the maxima in the lower right and upper left corners of the image, as well as the dip in the center, match the experimental observation. The most noticeable differences between the measurement (Fig. 7.3) and the calculated image are (1) the lower right edge of the diamond, which is much more pronounced in the measurement than in the calculation, and (2) the low intensity in the upper left corner of the measured image. However, these features constitute asymmetries of the measured image. In contrast, the utilized model is inherently symmetric², i.e., the roles of the tips could be exchanged without changing the calculation result, and their inclinations are not taken into account. In reality, the tips' inclinations break this symmetry. Possibly, the asymmetries in Fig. 7.3 are due to this symmetry breaking. Alternatively, experimental imperfections like slightly irregular aperture shapes might cause such asymmetries. The fact that the key features of the calculated image resemble those of the measurement suggest that the tips' inclinations do not significantly influence the excitation dynamics of the investigated waveguide modes.

The calculation also proves that indeed the third waveguide mode, for which a propagation constant below 1 has been calculated, significantly contributes to the intensity distribution at a distance of $\Delta y = 6.5 \mu\text{m}$ between both tips. For comparison, Fig. 7.4(c) shows an image which has been calculated similarly to the one in Fig. 7.4(b), but in which only the first two modes are taken into account. The pattern resembles an "X", with strong maxima along the main diagonal, and it does not strongly resemble the measured image (Fig. 7.3).

In conclusion, our measurements on gold strip waveguides show that the leaky surface

²The symmetry is slightly broken by assuming a finite size of the excitation tip, but a point-like detecting tip.

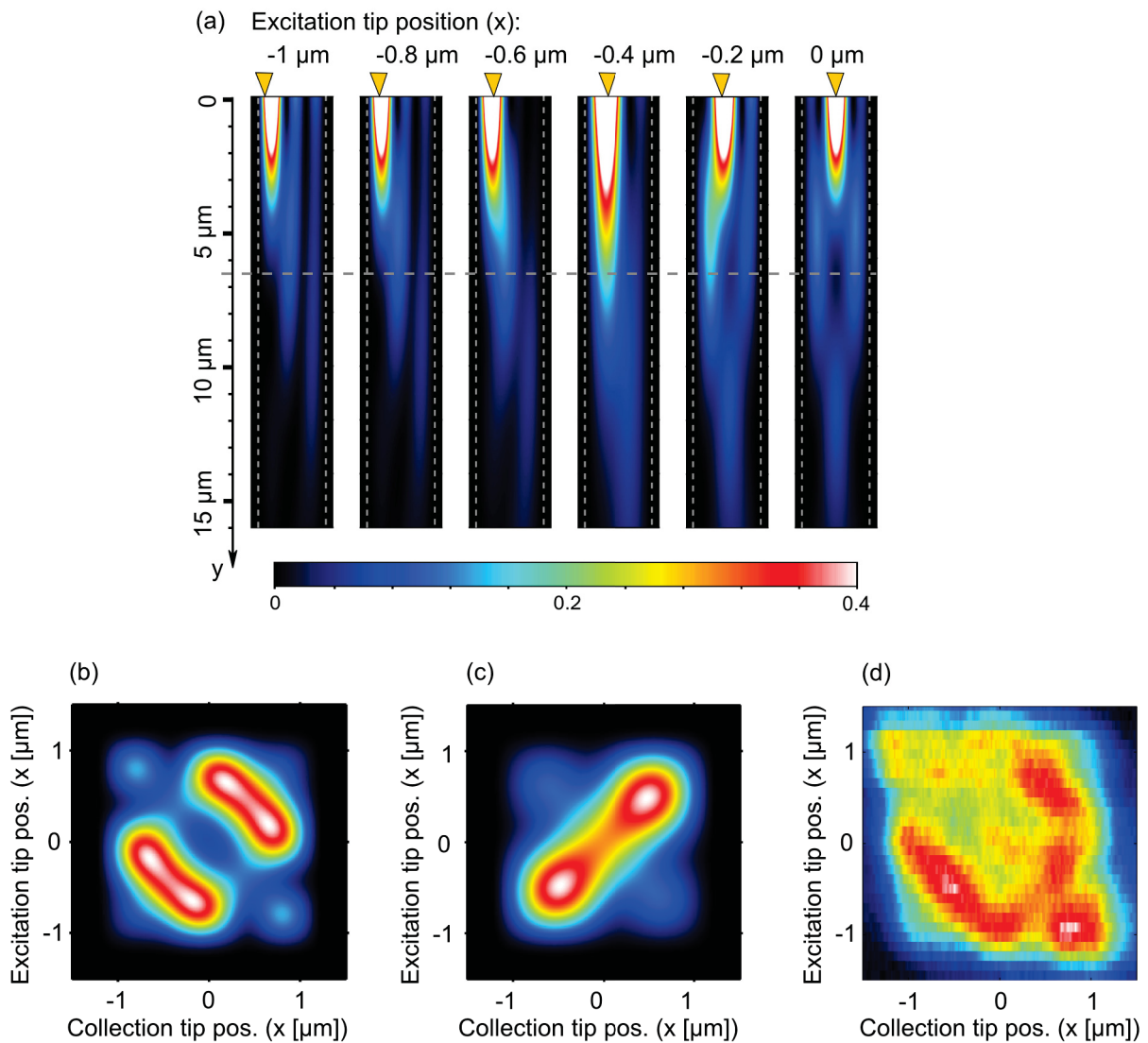


Figure 7.4: (a) Calculated beating patterns (intensities) of the first three leaky modes of a $2.5\ \mu\text{m}$ wide waveguide. The excitation tip's position with respect to the waveguide's symmetry axis is indicated above the images and by the orange triangles. The color scale of each image has been saturated at 40% of the maximum intensity to make the mode beating at longer propagation distances visible. The vertical dashed lines indicate the waveguide edges, the horizontal dashed line marks the position of the line scans represented in (b) and (c). (b) Simulated Dual-SNOM image showing the expected intensities as a function of both tips' x positions, assuming that the first three waveguide modes are excited and contribute to the image. The distance Δy between both tips is $6.5\ \mu\text{m}$. (c) Simulated Dual-SNOM image, assuming that only the first two waveguide modes contribute to the image. (d) Measured Dual-SNOM image (same as in Fig. 7.3) for comparison with (b) and (c).

modes can be efficiently excited and mapped by Dual-SNOM. The excitation conditions can be precisely tuned by simply positioning the excitation tip at different locations on the sample surface, thus modulating the relative excitation strengths of different waveguide modes. The measurement results could be qualitatively described by a simple theoretical model based on the spatial overlap between the excitation tip profile and the component of the sample modes' magnetic field which matches the tip's polarization characteristics. This model can also be related to the LDOS-based description of illumination-mode SNOM[129–131], because the overall coupling to the waveguide is expressed by the sum of the waveguide modes' H_x -components at the excitation tip's position.

Chapter 8

Summary and Outlook

The aim of this thesis was to apply scanning near-field optical microscopy (SNOM) for the investigation of the interaction of light with selected micro- and nano structures. Furthermore, it was envisaged to combine two SNOM heads into a Dual-SNOM setup, which permits truly near-field optical experiments where the first tip serves as a subwavelength light source and the second tip is used to map the electromagnetic near-fields at the sample surface.

One investigated example of single-SNOM is the near-field mapping of plasmonic Airy beams. An elaborate grating was used to generate the Airy plasmons, which exhibit a number of remarkable properties: upon propagation, the main lobe does not spread within a certain “diffraction-free” propagation range, which comprises several diffraction lengths of comparable Gaussian-shaped plasmons. Furthermore, the intensity features of the Airy plasmon follow parabolic trajectories, i.e., they self-accelerate. If an obstacle perturbs the wavefront, self-healing can be observed: The original intensity profile is restored. We succeeded to map the generated Airy plasmon, to experimentally demonstrate the aforementioned properties, and to quantitatively analyze its characteristics. Additionally, we experimentally demonstrated the generation of a bright hot-spot by interference of two mirror-symmetric Airy plasmons. By varying the grating positions or the illumination angle, the hot-spot could be shifted along the sample surface.

The imaging of whispering-gallery modes (WGM) in fused silica microresonators was another task which we first approached by collection-mode SNOM. While collection-mode SNOM is able to resolve the relevant details of the WGM and to reveal the mode symmetries in coupled microdisk resonators, a usually undesired property of aperture SNOM can be observed in these measurements: When the rather bulky, metal-coated aperture tip is

placed in the near-field region of a sample, it perturbs the sample's mode spectrum. Due to the high quality factors of the microdisk resonators, this effect is particularly pronounced in this type of micro-optical system. We took advantage of this sensitivity and developed a scattering-based mapping method for WGM. Here, a sharp, fully metal-coated fiber tip is used as a scatterer, whose position influences the resonance positions and the coupling between WGMs and their respective counter-propagating, degenerate modes. Consequently, the transmission and reflection that can be measured at the ends of the tapered fiber loop which serves for excitation of the WGMs are also modified by the tip's presence. By correlating the transmission and reflection signals with the tip's position, highly resolved images are obtained. However, these images don't constitute simple intensity maps of the WGMs, but can only be explained by an image formation model based on coupled-mode theory comprising the scattering tip.

As a further alternative to collection-mode SNOM, we developed scanning thermocouple-probe microscopy and demonstrated its functionality using the example of WGMs in microdisk resonators. Here, a commercially available miniature thermocouple is used to scan the sample surface. The tip is heated by light absorption, thus generating an electrical signal directly at the sample surface. We showed that in the case of WGM in microdisk resonators, the thermovoltage signal represents the near-field intensity at the tip's position, rather than the sample's surface temperature. Therefore, scanning thermocouple-probe microscopy can be used to obtain near-field intensity maps, being a complementary technique to aperture SNOM. In the application case of microdisk resonators, where we need a rather bulky SNOM tip with a large aperture to collect a sufficient optical signal, an advantage of the thermocouple method over collection-mode SNOM is that the thermocouple tip disturbs the modes to a lesser extent.

In the field of aperture SNOM, a major achievement of this thesis is the implementation of several different Dual-SNOM configurations. The first configuration comprises a vertical tip operating in shear-force feedback mode combined with a second tip operating in tapping mode. In this configuration, optical access from above as needed for non-transparent sample adjustments is not possible, which turned out to be an important drawback in experiments. The other two Dual-SNOM configurations consist of two identical SNOM heads using tapping mode feedback, which are arranged either opposite each other or in a right angle. In order to avoid tip collisions, a collision-prevention mechanism was developed which is based on mechanical interactions between the two oscillating tips of a Dual-SNOM. This mechanism is applicable to all three Dual-SNOM configurations.

Recently, the very first Dual-SNOM measurements were published by other groups [168–171], demonstrating the excitation of surface plasmon polaritons (SPPs) on metallic surfaces and their reflection at the edges of metal films and at grooves, which leads to interference fringes. Kaneta et al. [171] probed the carrier dynamics in quantum wells by Dual-SNOM. The theoretical models used to describe the aforementioned experiments differ considerably – the excitation tip is modeled as a dipole [168], as a randomly polarized source [170] or the polarization is not specified at all [169, 171]. The collection tip was assumed to be polarization-insensitive in all these studies.

In this thesis we systematically studied the image formation in Dual-SNOM measurements by using simple samples and by pre-characterizing the aperture tips. The inherent polarization characteristics of individual tips were investigated in the far-field, revealing significant polarization sensitivity for all tips. We studied the propagation directions of SPPs excited by an aperture tip with a “bull’s eye” grating, which converted the SPPs into free-space light. This experiment confirmed that the polarization characteristics of tips observed in the far-field are preserved in the near-field.

By using an unstructured, planar gold film as a sample, we obtained near-field images of the SPPs excited by an aperture SNOM tip. The observed images can be modeled by describing the excitation tip as a magnetic dipole source, while the inherent polarization-sensitivity of the collection tip determines the contribution of the different vectorial field components to the detected image. These polarization-resolved Dual-SNOM measurements, which have been obtained without any additional polarizers, highlight the important role of polarization in SNOM measurements.

Finally, we used the Dual-SNOM setup to study plasmonic modes in gold strip waveguides of different widths. In multi-mode waveguides, mode beating could be observed and it could be shown that the excitation strengths of the individual modes can be varied by changing the excitation tip’s position.

Perspectively, our Dual-SNOM setup can be used to study the near-field response of nanostructured samples to a point-dipole excitation at a precisely controlled position. The information obtained in this way is conceptually correlated with the sample’s Green’s dyadic tensor. This raises high expectations for the application to a multitude of structures like, e.g., metamaterials, photonic crystals, and various waveguides. However, one should not forget that the two metal-coated tips can significantly perturb the phenomena under investigation, and that often, a compromise has to be found between the achievable resolution and the photon count rate.

With the exception of the newly developed methods for imaging WGM in microdisk resonators, only commercial aperture SNOM probes whose aperture was formed by angled evaporation were used in the course of this thesis. However, alternative probes may provide more advantageous imaging properties, i.e., the throughput, resolution, and polarization control may be optimized. Several optimized tip designs have been proposed over the last few years, often fabricated by focused ion beam milling. Fully metal-coated fiber tips exhibiting plasmonic nanofocusing are another promising approach to realize an ideal SNOM probe. In Dual-SNOM, high throughput and good polarization control are of particular importance. Therefore, it would be rewarding to use such optimized tips in Dual-SNOM. In this case, the developed collision-prevention mechanism will be vital to prevent damage of the laboriously fabricated tips.

Apart from SNOM tips, other tips can readily be used in the Dual-SNOM setup: Thermocouple tips could be used as an alternative way to map optical intensities, whereas “electrical” tips could be used to map surface potentials which may change due to illumination by an excitation tip. Alternatively, one of the tips could serve to manipulate the sample, e.g. by nanolithography[249–251] or by operation as an optical tweezer[252], while the second tip maps the optical near-fields and/or the sample topography.

While time-resolved SNOM measurements with pulsed excitation have been demonstrated, it is problematic to combine this technique with Dual-SNOM, because signal levels would probably be too low, or rather, the measurements would take very long due to long integration times. The excitation power in such a measurement could not be scaled up above a certain threshold, because the metallic coating of the excitation tip would melt.

A challenging, but certainly worthwhile extension of the Dual-SNOM setup would be the implementation of a heterodyne technique, which would permit phase-resolved Dual-SNOM measurements. Propagation phenomena could then be studied in even greater detail.

In order to get further insights into image formation and artefacts both in single- and dual-tip SNOM, it might be worthwhile to combine a Dual-SNOM measurement with a conventional illumination-mode SNOM measurement, i.e., to additionally collect light via a microscope objective with high numerical aperture while the excitation tip is scanned over the sample. Such an illumination-mode SNOM measurement would give access to the partial LDOS[129–131] of the system. By positioning the collection tip at different locations, it could be investigated how its presence modifies the partial LDOS. Similarly, one might use leakage radiation microscopy to study the effect of the collection tip on the excited sample modes.

Appendix A

Zusammenfassung

In dieser Arbeit wurde mittels optischer Rasternahfeldmikroskopie (SNOM) die Wechselwirkung von Licht mit ausgewählten Mikro- und Nanostrukturen untersucht. Weiterhin wurden zwei SNOM-Messköpfe zu einem Zweispitzen-SNOM kombiniert, sodass die untersuchten Proben mit einer Aperturspitze angeregt werden können, während die zweite Aperturspitze das elektromagnetische Nahfeld an der Probenoberfläche vermisst.

Als Beispiele für SNOM-Untersuchungen mit einer einzelnen Aperturspitze wurden in der vorliegenden Arbeit der Nachweis von Airy-Plasmonen sowie die Untersuchung von Whispering-Gallery-Moden (“Flüstergaleriemoden”) in kugel- und scheibenförmigen Quarzglas-Mikroresonatoren vorgestellt.

Airy-Plasmonen sind Anregungen an Metalloberflächen, deren Profil durch eine Airy-Funktion beschrieben wird. Diese an Metalloberflächen gebundenen Strahlen folgen gebogenen Bahnen, wobei sich das Strahlprofil durch Beugung nicht aufweitet. Wird das Strahlprofil durch ein Hindernis gestört, regeneriert es sich innerhalb einer kurzen Propagationsstrecke selbst. Die Plasmonen wurden durch ein spezielles Gitter angeregt. Mit Hilfe von optischer Nahfeldmikroskopie (collection-mode SNOM) wurden die Airy-Plasmonen abgebildet. Ihre charakteristischen Eigenschaften wurden experimentell nachgewiesen und quantitativ untersucht. Weiterhin wurde experimentell gezeigt, dass sich durch Interferenz zweier Airy-Plasmonen ein eng umgrenztes plasmonisches Intensitätsmaximum, ein sogenannter “Hot-Spot”, erzeugen lässt. Durch Neigen des Anregungsstrahls oder Veränderung der Gittergeometrie konnten die Position und die Helligkeit des Hot-Spots variiert werden.

Flüstergaleriemoden in Mikroresonatoren konnten ebenfalls mittels collection-mode SNOM abgebildet werden. In diesen hochresonanten Systemen wird das Modenspektrum allerdings durch die Spitze merklich gestört. Dieser Effekt wurde in der zweiten vorge-

stellten Abbildungsmethode gezielt genutzt: Hierbei wurden die evaneszenten Felder der Resonatormoden durch eine scharfe, metallbeschichtete Spitze des Rastermikroskops gezielt gestreut. Die Position der Spitze beeinflusst die Resonanzpositionen der Flüstergaleriemoden und die Kopplung zwischen der angeregten Mode und der entsprechenden entarteten, in Gegenrichtung propagierenden Mode. Dadurch verändern sich die Transmission und Reflexion eines gebogenen Fasertapers, der zur Anregung der Flüstergaleriemoden dient. Durch Korrelation der Transmissions- und Reflexionssignale mit der Position der Spitze erhält man hochaufgelöste Abbildungen der Flüstergaleriemoden, die indirekte Rückschlüsse auf die Intensitätsverteilung an der Resonatoroberfläche erlauben.

Als dritte rastermikroskopische Abbildungsmethode für Flüstergaleriemoden wurde die Abtastung der Probenoberfläche mit einer Thermoelement-Spitze vorgestellt. Hierbei wird ausgenutzt, dass sich die Spitze durch optische Absorption aufheizt, sodass die Thermospannung als Maß für die Intensität genutzt werden kann.

Über diese Einzelspitzen-Messungen hinaus stellen der Aufbau verschiedener Zweispitzen-Nahfeldmikroskope und die damit durchgeführten Messungen wesentliche Ergebnisse der Arbeit dar. Um Zusammenstöße der Spitzen und damit einhergehende Beschädigungen zu vermeiden, wurde ein Schutzmechanismus entwickelt, der auf mechanischen Wechselwirkungen zwischen den beiden vibrierenden Spitzen beruht.

Zur Untersuchung der Bildentstehung im Zweispitzen-SNOM wurden die verwendeten Spitzen zunächst im Fernfeld charakterisiert. Hierbei zeigte sich, dass alle Spitzen eine intrinsische Polarisationsempfindlichkeit aufweisen, die jedoch von Spitze zu Spitze unterschiedlich ausfällt. Die im Fernfeld vermessenen Polarisationsseigenschaften zeigen sich gleichermaßen im Nahfeld der Spitzen. Dadurch war es möglich, Oberflächenplasmonen, die von einer Aperturspitze auf einer Goldoberfläche angeregt wurden, polarisationsaufgelöst abzubilden. Die so erhaltenen Bilder konnten durch ein theoretisches Modell erklärt werden, in dem die Anregungsspitze als magnetische Dipolquelle betrachtet wird. Die Ausrichtung dieses Dipols steht im Einklang mit der Polarisation des Lichts, das von der Spitze ins Fernfeld abgestrahlt wird. Die Polarisationsempfindlichkeit der abbildenden Spitze bestimmt, wie stark die verschiedenen Vektorkomponenten des elektromagnetischen Nahfelds zum detektierten Signal beitragen. Die beschriebenen polarisationsaufgelösten Messungen unterstreichen die wichtige Rolle der Polarisation in SNOM-Untersuchungen.

Mit dem Zweispitzen-SNOM wurden plasmonische Leckmoden in Goldstreifen-Wellenleitern angeregt und abgebildet. In Multimodewellenleitern konnten Schwebungsmuster beobachtet werden, die sich durch Verschieben der Anregungsspitze verändern, da die

Anregungskoeffizienten der einzelnen Moden von der Position der Anregungsspitze abhängen. Diese Abhängigkeiten konnten durch ein einfaches Modell beschrieben werden, in dem die Anregungsspitze als gaußförmige, polarisierte Quelle dargestellt wurde. Somit ist es gelungen, Zweispitzen-Nahfeldmikroskopie zur Untersuchung der Wellenleitermoden einzusetzen und die Bildentstehung zu modellieren.

Appendix B

Lebenslauf

Name	Angela Elisabeth Klein (geb. Weitz)
26.02.1984	Geburt in St. Wendel
03.2002	Abitur, Staatliches Gymnasium Birkenfeld (Nahe)
04.2002–03.2007	Studium der Physik an der Universität Karlsruhe (TH)
03.2004–08.2004	wissenschaftliche Hilfskraft, Institut für Nanotechnologie, Forschungszentrum Karlsruhe
09.2004–07.2005	Studium der Physik an der Université Joseph Fourier, Grenoble, Frankreich
04.2005–07.2005	Studienarbeit, CEA, Grenoble, Frankreich
03.2007	Diplom in Physik, Universität Karlsruhe (TH)
05.2007–09.2007	Praktikum, XAAR Jet AB, Järfälla, Schweden
seit 01.2008	Doktorandin am Institut für Angewandte Physik, Friedrich-Schiller-Universität Jena

Stipendien und Auszeichnungen

- 2003–2007 Studienstipendium der Studienstiftung des deutschen Volkes
- 2004–2005 Auslandsstipendium der Deutsch-Französischen Hochschule
- 2006 Deutsch-Französischer Hochschulpreis
- 2008–2011 Promotionsstipendium
der Jena School for Microbial Communication (JSMC),
Deutsche Forschungsgemeinschaft

Jena, 06.10.2014

Appendix C

Publications

Journal articles

- A. E. Klein, N. Janunts, M. Steinert, A. Tünnermann, and T. Pertsch, *Polarization-resolved near-field mapping of plasmonic aperture emission by a Dual-SNOM system*, Nano Lett. **14**, 5010 (2014).
- A. E. Klein, C. Schmidt, M. Liebsch, N. Janunts, M. Dobynde, A. Tünnermann, and T. Pertsch, *Highly sensitive mode mapping of whispering-gallery modes by scanning thermocouple-probe microscopy*, Opt. Lett. **39**, 1157 (2014).
- A. Minovich, A. E. Klein, D. N. Neshev, T. Pertsch, Y. S. Kivshar, and D. N. Christodoulides, *Airy plasmons: non-diffracting optical surface waves*, Laser & Photonics Reviews **8**, 221 (2014).
- C. Schmidt, M. Liebsch, A. Klein, N. Janunts, A. Chipouline, T. Käsebier, C. Etrich, F. Lederer, E.-B. Kley, A. Tünnermann, and T. Pertsch, *Near-field mapping of optical eigenstates in coupled disk microresonators*, Phys. Rev. A **85**, 033827 (2012).
- A. E. Klein, N. Janunts, A. Tünnermann, and T. Pertsch, *Investigation of mechanical interactions between the tips of two scanning near-field optical microscopes*, Appl. Phys. B **108**, 737 (2012).
- A. E. Klein, A. Minovich, M. Steinert, N. Janunts, A. Tünnermann, D. N. Neshev, Y. S. Kivshar, and T. Pertsch, *Controlling plasmonic hot spots by interfering Airy beams*, Opt. Lett. **37**, 3402 (2012).

-
- A. Minovich, A. E. Klein, N. Janunts, T. Pertsch, D. N. Neshev, and Y. S. Kivshar, *Generation and near-field imaging of Airy surface plasmons*, Phys. Rev. Lett. **107**, 116802 (2011).

Manuscripts in preparation

- A. E. Klein, N. Janunts, S. Schmidt, S. B. Hasan, T. Kaiser, C. Etrich, S. Falsold, C. Rockstuhl, A. Tünnermann, and T. Pertsch, *Dual-SNOM investigations of plasmonic strip waveguides*, manuscript in preparation (2014).
- S. Schmidt, A. E. Klein, T. Paul, H. Gross, B. N. Tugchin, N. Janunts, S. Diziain, A. da Costa Assafrao, T. Pertsch, H. P. Urbach, and C. Rockstuhl, *Image formation process in aperture based scanning near field optical microscopes*, manuscript in preparation (2014).
- J. Qi, T. Kaiser, A. E. Klein, M. Steinert, T. Pertsch, F. Lederer, and C. Rockstuhl, *Reinforcing resonances of optical nanoantennas with concentric ring gratings*, manuscript in preparation (2014).
- B. N. Tugchin, N. Janunts, A. E. Klein, M. Steinert, D. Sivun, M. Sison, E.-B. Kley, A. Tünnermann, and T. Pertsch, *Plasmonic tip for efficient detection and excitation by radially polarized conical surface plasmon polariton*, manuscript in preparation (2014).

International Conferences (only own presentations)

- A. Klein, Janunts, and T. N., Pertsch, *Development of a double-tip SNOM: Acoustic interaction of two SNOM tips as a tool to prevent tip collision*, oral, in *NFO-11 - The 11th International Conference on Near-field Optics, Nanophotonics & Related Techniques, Beijing, August 29 - September 2* (2010).
- A. Klein, N. Janunts, and T. Pertsch, *Double-tip scanning near-field optical microscopy - instrumentation and application to plasmonics*, oral, in *NFO-12 - The 12th International Conference on Near-Field Optics, Nanophotonics & Related Techniques, Donostia - San Sebastian, September 3-7* (2012).

- A. Klein, A. Minovich, M. Steinert, N. Janunts, D. Neshev, A. Tünnermann, Y. S. Kivshar, and T. Pertsch, *Interference of Airy surface plasmons*, oral, in *NFO-12 - The 12th International Conference on Near-Field Optics, Nanophotonics and Related Techniques, Donostia - San Sebastian, September 3-7 (2012)*.
- A. Klein, A. Minovich, N. Janunts, D. Neshev, Y. Kivshar, A. Tünnermann, and T. Pertsch, *High-intensity spot created by interference of Airy plasmons*, oral, in *International Conference on Nanoscience + Technology (ICN+T2012), Paris, July 23-27 (2012)*.
- A. E. Klein, N. Janunts, and T. Pertsch, *Preventing tip destruction in a double-tip SNOM system by mechanical interaction between both tips*, poster, in *International Conference on Nanoscience + Technology (ICN+T2012), Paris, July 23-27 (2012)*.

Conference proceedings

- A. Minovich, A. E. Klein, N. Janunts, T. Pertsch, D. N. Neshev, and Y. S. Kivshar, *Near-field observation of Airy plasmons*, in *Proceedings of the International Quantum Electronics Conference and Conference on Lasers and Electro-Optics Pacific Rim 2011*, p. J755 (2011).
- A. Minovich, A. E. Klein, N. Janunts, T. Pertsch, D. N. Neshev, and Y. S. Kivshar, *Generation and near-field imaging of Airy plasmons*, in *Quantum Electronics and Laser Science Conference*, p. QThQ6 (2011).
- A. Minovich, A. E. Klein, N. Janunts, T. Pertsch, D. N. Neshev, and Y. S. Kivshar, *Near-field mapping of Airy plasmons*, in *Lasers and Electro-Optics Europe (CLEO EUROPE/EQEC), 2011 Conference on and 12th European Quantum Electronics Conference (2011)*.
- A. Minovich, A. E. Klein, M. Steinert, N. Janunts, A. Tünnermann, F. F. Bleckmann, S. Linden, T. Pertsch, D. Neshev, and Y. Kivshar, *Non-diffracting Airy surface plasmons: Generation, manipulation, and interference*, in *Frontiers in Optics 2012/Laser Science XXVIII, OSA Technical Digest*, p. FW2F.4.

Other presentations

- A. E. Klein, N. Janunts, and T. Pertsch, *Near-field optical measurements by single and multiple fiber tips*, oral, in *Doctoral students conference for the discussion of optical concepts (DokDok)*, Naumburg, March 21-25 (2011).
- A. E. Klein, A. Minovich, M. Steinert, N. Janunts, A. Tünnermann, D. N. Neshev, Y. S. Kivshar, and T. Pertsch, *Controlling plasmonic hot-spots by interfering Airy beams*, oral, in *Doctoral students conference on optics (DokDok)*, Oppurg, October 7-11 (2012).
- A. E. Klein, N. Janunts, and T. Pertsch, *Near-field optical observation of plasmonic beams*, oral, in *ASP seminar, Abbe School of Photonics, Jena, October 21* (2011).
- A. E. Klein, A. Minovich, M. Steinert, N. Janunts, A. Tünnermann, D. N. Neshev, Y. S. Kivshar, and T. Pertsch, *Controlling plasmonic hot-spots by interfering airy beams*, oral, in *JSMC retreat, Bad Sulza, July 2-3*, (2012).
- A. E. Klein, N. Janunts, and T. Pertsch, *Scanning near-field optical microscopy: Applications in nano-optics and in biology*, oral, in *JSMC symposium, Jena, December 15-16* (2008).
- A. E. Klein, N. Janunts, and T. Pertsch, *New tip design for high-resolution SNOM and raman imaging*, oral, in *JSMC/ILRS Symposium, Jena, October 12-13* (2009).
- A. E. Klein, N. Janunts, and T. Pertsch, *Scanning near-field optical microscopy – applications in physics and in biology*, poster, in *Beutenberg Campus Workshop, Jena, June 4* (2009).
- A. E. Klein, N. Janunts, M. Kroll, and T. Pertsch, *Emission and detection patterns of fiber probes for near-field optical measurements*, poster, in *1st European Student Conference on Microbial Communication, Jena, September 13-16* (2011).
- A. E. Klein, N. Janunts, C. Schmidt, M. Liebsch, A. Minovich, D. Neshev, Y. Kivshar, and T. Pertsch, *Scanning probe techniques for optical near-field microscopy below the diffraction limit*, poster, in *JSMC Symposium, Jena, September 2-3* (2014).

Appendix D

Acknowledgements

This work would not have been possible without the support of many people who supported me in various ways during the past years. In particular I would like to thank

- Prof. Dr. Thomas Pertsch for giving me the opportunity to work in his group, for patiently discussing my work and for asking the right questions which lead me on the right track on many occasions
- again Prof. Dr. Thomas Pertsch for creating a pleasant working atmosphere and for giving me the opportunity to participate in international conferences.
- Dr. Norik Janunts who gave me advice and support throughout the work on my thesis project, for sharing his knowledge and experience, discussing uncountable ideas and hypotheses, and for the practical help in the lab
- Dr. Alexander Minovich and Dr. Dragomir Neshev for involving me in the project on Airy plasmons and for sharing their scientific ideas and visions
- Dr. Carsten Schmidt and Mattes Liebsch for the fruitful and pleasant collaboration, which significantly contributed to further explore the possibilities of the single-SNOM setup
- Dr. Christian Helgert, Stefan Fasold, and Michael Steinert for fabricating many micro- and nano structured samples, always being helpful and fast
- Sören Schmidt for the regular exchange of ideas, which broadened my view on aperture SNOM

- Christoph Etrich and Shakeeb Bin Hasan, who have helped me understand the waveguide measurements with their numerical calculations
- Prof. Dr. Carsten Rockstuhl, Prof. Dr. Ulf Peschel, Dr. Dmitry Kazantsev, and Thomas Kaiser for suggestions which helped me in understanding some of my results better
- the Nanonics team for inviting me to visit the company and for quickly responding to technical support inquiries
- the department's mechanical workshop for fabricating numerous adapters and mechanical parts for the experimental setups
- Dr. Falk Eilenberger, Matthias Zilk, Dr. Matthias Klein, Michael Steinert and Thomas Kaiser for proof-reading the thesis; Matthias Zilk for his advice on many software-related issues
- my office-mates Dr. Séverine Diziain and Bayarjargal Narantsatsralt Tugchin for always having an open ear and the willingness to discuss current matters
- all my colleagues for creating a warm working atmosphere and for sharing their knowledge and ideas
- the JSMC (Jena School for Microbial Communication) for supporting me by a three-year scholarship
- my family and my friends for their constant support and for motivating me
- my husband, who contributed to the success of this thesis in manifold ways, for his understanding, for encouraging me, and for sharing and enriching my life
- anyone I may have forgotten unintentionally

Appendix E

Ehrenwörtliche Erklärung

Ich erkläre hiermit ehrenwörtlich, dass ich die vorliegende Arbeit selbständig, ohne unzulässige Hilfe Dritter und ohne Benutzung anderer als der angegebenen Hilfsmittel und Literatur angefertigt habe. Die aus anderen Quellen direkt oder indirekt übernommenen Daten und Konzepte sind unter Angabe der Quelle gekennzeichnet.

Bei der Auswahl und Auswertung folgenden Materials haben mir die nachstehend aufgeführten Personen in der jeweils beschriebenen Weise unentgeltlich geholfen:

1. Prof. Dr. Thomas Pertsch hat das Promotionsvorhaben betreut und in diesem Rahmen die in der Arbeit dargestellten Themen sowie die Dissertationsschrift mit mir diskutiert.
2. Dr. Norik Janunts war ebenfalls als Ratgeber an allen bearbeiteten Themen beteiligt, sowie am Aufbau des Dual-SNOM Setups.
3. Die Arbeiten zu Airy-Plasmonen wurden in Zusammenarbeit mit Dr. Alexander Minovich und Dr. Dragomir Neshev durchgeführt. Von Dr. Alexander Minovich stammen die Idee zur Anregung von Airy-Plasmonen sowie deren veröffentlichte theoretische und numerische Beschreibung. Die experimentellen Ergebnisse wurden vor der Veröffentlichung gemeinsam diskutiert und interpretiert. Die meisten der veröffentlichten Abbildungen wurden von Dr. Alexander Minovich erstellt.
4. Die Arbeiten zur Abbildung von Flüstergaleriemoden in Mikroresonatoren wurden zusammen mit Dr. Carsten Schmidt und Mattes Liebsch durchgeführt, die für den experimentellen Aufbau des Setups zur Anregung der Moden in Mikroresonatoren verantwortlich waren und einen Großteil der Messungen durchgeführt haben. Von

Dr. Carsten Schmidt stammt auch die Auswertung und Interpretation der Streumessungen an Mikroresonatoren. Die Messung zur Zeitauflösung der Thermoelement-Detektion wurde von Mikhail Dobynde durchgeführt.

5. Dr. Shakeeb Bin Hasan hat mir das Comsol-Modell zur Berechnung der Leckmoden in plasmonischen Wellenleitern zur Verfügung gestellt.
6. Dr. Falk Eilenberger, Matthias Zilk, Dr. Matthias Klein, Michael Steinert und Thomas Kaiser haben jeweils Teile meiner Arbeit korrekturgelesen.
7. Dr. Christian Helgert, Stefan Fasold, Michael Steinert, Dr. Alexander Minovich und Thomas Käsebier haben die verwendeten Proben hergestellt.
8. fachliche Diskussionen mit den folgenden Personen haben außerdem wichtige Impulse zu inhaltlichen Aspekten der Arbeit gegeben: Prof. Dr. Carsten Rockstuhl, Sören Schmidt, Thomas Kaiser, Dr. Dmitry Kazantsev und Prof. Dr. Ulf Peschel.

Weitere Personen waren an der inhaltlich-materiellen Erstellung der vorliegenden Arbeit nicht beteiligt. Insbesondere habe ich hierfür nicht die entgeltliche Hilfe von Vermittlungs- bzw. Beratungsdiensten (Promotionsberater oder andere Personen) in Anspruch genommen. Niemand hat von mir unmittelbar oder mittelbar geldwerte Leistungen für Arbeiten erhalten, die im Zusammenhang mit dem Inhalt der vorgelegten Dissertation stehen.

Die Arbeit wurde bisher weder im In- noch im Ausland in gleicher oder ähnlicher Form einer anderen Prüfungsbehörde vorgelegt.

Die geltende Promotionsordnung der Physikalisch-Astronomischen Fakultät ist mir bekannt.

Ich versichere ehrenwörtlich, dass ich nach bestem Wissen die reine Wahrheit gesagt und nichts verschwiegen habe.

Jena, 15.10.2014

Angela Klein

Bibliography

- [1] G. Sines and Y. A. Sakellarakis, *Lenses in antiquity*, Am. J. Archaeol. **91**, 191 (1987).
- [2] J. M. Enoch, *Ancient lenses in art and sculpture and the objects viewed through them, dating back 4500 years*, in *Proc. SPIE*, vol. 3299, pp. 424–430 (1998).
- [3] K. Uluç, G. C. Kujoth, and M. K. Başkaya, *Operating microscopes: past, present, and future*, Neurosurg. Focus **27**, E4 (2009).
- [4] F. Frischknecht, M. Gunzer, and S. L. Shorte, *Retrospective: Birth of the cool – imaging and microbiology from Ibn al-Haytham to Jean Comandon*, Biotechnol. J. **4**, 787 (2009).
- [5] P. Hamou, *The mutation of the visible. Essay on the epistemological significance of optical instruments in the 17th century (vol. 2): Microscopes and telescopes in England, from Bacon to Hooke*, Presses Universitaires du Septentrion, Villeneuve d’Asq (2001).
- [6] J. Schickore, *The microscope and the eye: a history of reflections, 1740-1870*, University of Chicago Press, Chicago (2007).
- [7] D. Bardell, *The biologists’ forum: The invention of the microscope*, BIOS **75**, 78 (2004).
- [8] J. A. Barnett, *Beginnings of microbiology and biochemistry: the contribution of yeast research*, Microbiology **149**, 557 (2003).
- [9] S. A. Maier, Springer, New York (2007).
- [10] N. Engheta and R. W. Ziolkowski (editors), *Metamaterials: Physics and Engineering Explorations*, John Wiley & Sons, New York (2006).
- [11] S. Zouhdi, A. Sihvola, and A. P. Vinogradov (editors), *Metamaterials and Plasmonics: Fundamentals, Modelling, Applications*, NATO Science for Peace and Security Series B: Physics and Biophysics, Springer, Dordrecht (2008).
- [12] G. V. Eleftheriades and K. G. Balmain (editors), *Negative-Refraction Metamaterials: Fundamental Principles and Applications*, John Wiley & Sons, New York (2005).

- [13] W. Cai and V. Shalaev, *Optical Metamaterials: Fundamentals and Applications*, Springer, New York (2009).
- [14] K. C. Y. Huang, M.-K. Seo, T. Sarmiento, Y. Huo, J. S. Harris, and M. L. Brongersma, *Electrically driven subwavelength optical nanocircuits*, Nat. Photonics **8**, 244 (2014).
- [15] A. Kriesch, S. P. Burgos, D. Ploss, H. Pfeifer, H. A. Atwater, and U. Peschel, *Functional plasmonic nanocircuits with low insertion and propagation losses*, Nano Lett. **13**, 4539 (2013).
- [16] J. Zhang and L. Zhang, *Nanostructures for surface plasmons*, Adv. Opt. Photon. **4**, 157 (2012).
- [17] E. Ozbay, *Plasmonics: Merging photonics and electronics at nanoscale dimensions*, Science **311**, 189 (2006).
- [18] M.-H. Shih, *Plasmonics: Small and fast plasmonic modulator*, Nat. Photonics **8**, 171 (2014).
- [19] H. A. Atwater and A. Polman, *Plasmonics for improved photovoltaic devices*, Nat. Mater. **9**, 205 (2010).
- [20] E. Abbe, *Beiträge zur Theorie des Mikroskops und der mikroskopischen Wahrnehmung*, Arch. Mikroskop. Anat. **9**, 413 (1873).
- [21] B. Bailey, D. L. Farkas, D. L. Taylor, and F. Lanni, *Enhancement of axial resolution in fluorescence microscopy by standing-wave excitation*, Nature **366**, 44 (1993).
- [22] M. G. L. Gustafsson, *Surpassing the lateral resolution limit by a factor of two using structured illumination microscopy*, J. Microsc. **198**, 82 (2000).
- [23] A. Jost and R. Heintzmann, *Superresolution multidimensional imaging with structured illumination microscopy*, Annu. Rev. Mater. Res. **43**, 261 (2013).
- [24] E. Betzig, G. H. Patterson, R. Sougrat, O. W. Lindwasser, S. Olenych, J. S. Bonifacino, M. W. Davidson, J. Lippincott-Schwartz, and H. F. Hess, *Imaging intracellular fluorescent proteins at nanometer resolution*, Science **313**, 1642 (2006).
- [25] M. J. Rust, M. Bates, and X. Zhuang, *Sub-diffraction-limit imaging by stochastic optical reconstruction microscopy (STORM)*, Nat. Methods **3**, 793 (2006).
- [26] S. T. Hess, T. P. K. Girirajan, and M. D. Mason, *Ultra-high resolution imaging by fluorescence photoactivation localization microscopy*, Biophys. J. **91**, 4258 (2006).
- [27] S. W. Hell and J. Wichmann, *Breaking the diffraction resolution limit by stimulated emission: stimulated-emission-depletion fluorescence microscopy*, Optics Letters **19**, 780 (1994).

- [28] L. Novotny, *The history of near-field optics*, in E. Wolf (editor), *Progress in Optics*, vol. 50, pp. 137–184, Elsevier (2007).
- [29] B. Hecht, B. Sick, U. P. Wild, V. Deckert, R. Zenobi, O. J. F. Martin, and D. W. Pohl, *Scanning near-field optical microscopy with aperture probes: Fundamentals and applications*, *The Journal of Chemical Physics* **112**, 7761 (2000).
- [30] J. Kim and K.-B. Song, *Recent progress of nano-technology with NSOM*, *Micron* **38**, 409 (2007).
- [31] S. Mononobe, *Near-field optical fiber probes and the applications i*, in M. Ohtsu (editor), *Handbook of Nano-Optics and Nanophotonics*, pp. 281–333, Springer Berlin Heidelberg (2013).
- [32] M. A. Paesler and P. J. Moyer, *Near-field optics: theory, instrumentation, and applications*, John Wiley & Sons, New York (1996).
- [33] D. Courjon, *Near-field microscopy and near-field optics*, Imperial College Press, London (2003).
- [34] L. Novotny and B. Hecht, *Principles of Nano-Optics*, Cambridge University Press, Cambridge (2005).
- [35] M. Brehm, H. G. Frey, R. Guckenberger, R. Hillenbrand, D. Kazantsev, F. Keilmann, N. Ocelic, and T. Taubner, *Consolidating apertureless SNOM*, *Journal of the Korean Physical Society* **47**, S80 (2005).
- [36] J.-S. Bouillard, S. Vilain, W. Dickson, and A. V. Zayats, *Hyperspectral imaging with scanning near-field optical microscopy: applications in plasmonics*, *Opt. Express* **18**, 16513 (2010).
- [37] S. Vignolini, F. Intonti, F. Riboli, D. S. Wiersma, L. Balet, L. H. Li, M. Francardi, A. Gerardino, A. Fiore, and M. Gurioli, *Polarization-sensitive near-field investigation of photonic crystal microcavities*, *Appl. Phys. Lett.* **94**, 163102 (2009).
- [38] B. Le Feber, N. Rotenberg, D. M. Beggs, and L. Kuipers, *Simultaneous measurement of nanoscale electric and magnetic optical fields*, *Nat. Photonics* **8**, 43 (2014).
- [39] M. L. M. Balistreri, H. Gersen, J. P. Korterik, L. Kuipers, and N. F. v. Hulst, *Tracking femtosecond laser pulses in space and time*, *Science* **294**, 1080 (2001).
- [40] A. Nesci, R. Dändliker, and H. P. Herzig, *Quantitative amplitude and phase measurement by use of a heterodyne scanning near-field optical microscope*, *Opt. Lett.* **26**, 208 (2001).
- [41] M. Burrese, D. v. Oosten, T. Kampfrath, H. Schoenmaker, R. Heideman, A. Leinse, and L. Kuipers, *Probing the magnetic field of light at optical frequencies*, *Science* **326**, 550 (2009).

- [42] X. S. Xie and R. C. Dunn, *Probing single molecule dynamics*, Science **265**, 361 (1994).
- [43] M. Ono, K. Matsuda, T. Saiki, K. Nishi, T. Mukaiyama, and M. Kuwata-Gonokami, *Time-resolved emission from self-assembled single quantum dots using scanning near-field optical microscope*, Jpn. J. Appl. Phys. **38**, L1460 (1999).
- [44] T. Nagahara, K. Imura, and H. Okamoto, *Time-resolved scanning near-field optical microscopy with supercontinuum light pulses generated in microstructure fiber*, Rev. Sci. Instrum. **75**, 4528 (2004).
- [45] G. Binnig and H. Rohrer, *Scanning tunneling microscope*, US Patent 4.343.993 (1982).
- [46] G. Binnig, C. F. Quate, and C. Gerber, *Atomic force microscope*, Phys. Rev. Lett. **56**, 930 (1986).
- [47] E. Synge, *A suggested method for extending microscopic resolution into the ultra-microscopic region*, Philos. Mag. **6**, 356 (1928).
- [48] H. Bethe, *Theory of diffraction by small holes*, Physical Review **66**, 163 (1944).
- [49] C. Bouwkamp, *On Bethe's theory of diffraction by small holes*, Phillips Res. Rep **5**, 321 (1950).
- [50] E. A. Ash and G. Nicholls, *Super-resolution aperture scanning microscope*, Nature **237**, 510 (1972).
- [51] D. W. Pohl, W. Denk, and M. Lanz, *Optical stethoscopy: Image recording with resolution $\lambda/20$* , Appl. Phys. Lett. **44**, 651 (1984).
- [52] A. Lewis, M. Isaacson, A. Harootunian, and A. Muray, *Development of a 500 Å spatial resolution light microscope: I. Light is efficiently transmitted through $\lambda/16$ diameter apertures*, Ultramicroscopy **13**, 227 (1984).
- [53] E. Betzig, A. Lewis, A. Harootunian, M. Isaacson, and E. Kratschmer, *Near field scanning optical microscopy (NSOM): development and biophysical applications*, Biophys. J. **49**, 269 (1986).
- [54] R. Eckert, J. M. Freyland, H. Gersen, H. Heinzelmann, G. Schürmann, W. Noell, U. Stauffer, and N. F. d. Rooij, *Near-field fluorescence imaging with 32 nm resolution based on microfabricated cantilevered probes*, Appl. Phys. Lett. **77**, 3695 (2000).
- [55] A. Naber, D. Molenda, U. C. Fischer, H.-J. Maas, C. Höppener, N. Lu, and H. Fuchs, *Enhanced light confinement in a near-field optical probe with a triangular aperture*, Phys. Rev. Lett. **89**, 210801 (2002).
- [56] C. Mihalcea, W. Scholz, S. Werner, S. Münster, E. Oesterschulze, and R. Kassing, *Multipurpose sensor tips for scanning near-field microscopy*, Appl. Phys. Lett. **68**, 3531 (1996).

- [57] S. Werner, O. Rudow, C. Mihalcea, and E. Oesterschulze, *Cantilever probes with aperture tips for polarization-sensitive scanning near-field optical microscopy*, Appl. Phys. A **66**, S367 (1998).
- [58] H. Zhou, A. Midha, L. Bruchhaus, G. Mills, L. Donaldson, and J. M. R. Weaver, *Novel scanning near-field optical microscopy/atomic force microscope probes by combined micromachining and electron-beam nanolithography*, J. Vac. Sci. Technol. B **17**, 1954 (1999).
- [59] P. Grabiec, J. Radojewski, M. Zaborowski, K. Domanski, T. Schenkel, and I. W. Rangelow, *Batch fabricated scanning near field optical microscope/atomic force microscopy microprobe integrated with piezoresistive cantilever beam with highly reproducible focused ion beam micromachined aperture*, Journal of Vacuum Science & Technology B **22**, 16 (2003).
- [60] J. Wessel, *Surface-enhanced optical microscopy*, J. Opt. Soc. Am. B **2**, 1538 (1985).
- [61] U. C. Fischer and D. W. Pohl, *Observation of single-particle plasmons by near-field optical microscopy*, Phys. Rev. Lett. **62**, 458 (1989).
- [62] M. Specht, J. D. Pedarnig, W. M. Heckl, and T. W. Hänsch, *Scanning plasmon near-field microscope*, Phys. Rev. Lett. **68**, 476 (1992).
- [63] Y. Inouye and S. Kawata, *Near-field scanning optical microscope with a metallic probe tip*, Opt. Lett. **19**, 159 (1994).
- [64] P. Gleyzes, A. C. Boccara, and R. Bachelot, *Near field optical microscopy using a metallic vibrating tip*, Ultramicroscopy **57**, 318 (1995).
- [65] F. Keilmann and R. Hillenbrand, *Near-field microscopy by elastic light scattering from a tip*, Phil. Trans. R. Soc. Lond. A **362**, 787 (2004).
- [66] R. D. Grober, R. J. Schoelkopf, and D. E. Prober, *Optical antenna: Towards a unity efficiency near-field optical probe*, Applied Physics Letters **70**, 1354 (1997).
- [67] J. N. Farahani, H.-J. Eisler, D. W. Pohl, M. Pavius, P. Flückiger, P. Gasser, and B. Hecht, *Bow-tie optical antenna probes for single-emitter scanning near-field optical microscopy*, Nanotechnology **18**, 125506 (2007).
- [68] F. Huth, A. Chuvilin, M. Schnell, I. Amenabar, R. Krutokhvostov, S. Lopatin, and R. Hillenbrand, *Resonant antenna probes for tip-enhanced infrared near-field microscopy*, Nano Letters **13**, 1065 (2013).
- [69] A. Lewis and K. Lieberman, *Near-field optical imaging with a non-evanescently excited high-brightness light source of sub-wavelength dimensions*, Nature **354**, 214 (1991).

- [70] S. K. Sekatskii and V. S. Letokhov, *Single fluorescence centers on the tips of crystal needles: First observation and prospects for application in scanning one-atom fluorescence microscopy*, Appl. Phys. B **63**, 525 (1996).
- [71] J. Michaelis, C. Hettich, J. Mlynek, and V. Sandoghdar, *Optical microscopy using a single-molecule light source*, Nature **405**, 325 (2000).
- [72] S. Kühn, C. Hettich, C. Schmitt, J.-P. Poizat, and V. Sandoghdar, *Diamond colour centres as a nanoscopic light source for scanning near-field optical microscopy*, J. Microsc. **202**, 2 (2001).
- [73] J. Tisler, T. Oeckinghaus, R. J. Stöhr, R. Kolesov, R. Reuter, F. Reinhard, and J. Wrachtrup, *Single defect center scanning near-field optical microscopy on graphene*, Nano Lett. **13**, 3152 (2013).
- [74] S. Jäger, A. M. Kern, M. Hentschel, R. Jäger, K. Braun, D. Zhang, H. Giessen, and A. J. Meixner, *Au nanotip as luminescent near-field probe*, Nano Lett. **13**, 3566 (2013).
- [75] A. Bouhelier, J. Renger, M. R. Beversluis, and L. Novotny, *Plasmon-coupled tip-enhanced near-field optical microscopy*, J. Microsc. **210**, 220 (2003).
- [76] N. A. Janunts, K. S. Baghdasaryan, K. V. Nerkararyan, and B. Hecht, *Excitation and superfocusing of surface plasmon polaritons on a silver-coated optical fiber tip*, Opt. Commun. **253**, 118 (2005).
- [77] W. Ding, S. R. Andrews, and S. A. Maier, *Internal excitation and superfocusing of surface plasmon polaritons on a silver-coated optical fiber tip*, Phys. Rev. A **75**, 063822 (2007).
- [78] C. Zeh, R. Spittel, S. Unger, J. Opitz, B. Köhler, J. Kirchhof, H. Bartelt, and L. M. Eng, *Polarization mode preservation in elliptical index tailored optical fibers for apertureless scanning near-field optical microscopy*, Applied Physics Letters **97**, 103108 (2010).
- [79] J. Barthes, G. C. d. Francs, A. Bouhelier, and A. Dereux, *A coupled lossy local-mode theory description of a plasmonic tip*, New J. Phys. **14**, 083041 (2012).
- [80] B. N. Tugchin, N. Janunts, A. E. Klein, M. Steinert, D. Sivun, M. Sison, E.-B. Kley, A. Tünnermann, and T. Pertsch, *Plasmonic tip for efficient detection and excitation by radially polarized conical surface plasmon polariton*, manuscript in preparation (2014).
- [81] A. J. Babadjanyan, N. L. Margaryan, and K. V. Nerkararyan, *Superfocusing of surface polaritons in the conical structure*, J. Appl. Phys. **87**, 3785 (2000).

- [82] M. I. Stockman, *Nanofocusing of optical energy in tapered plasmonic waveguides*, Phys. Rev. Lett. **93**, 137404 (2004).
- [83] D. Gramotnev and S. Bozhevolnyi, *Plasmonics beyond the diffraction limit*, Nat. Photonics **4**, 83 (2010).
- [84] C. Ropers, C. C. Neacsu, T. Elsaesser, M. Albrecht, M. B. Raschke, and C. Lienau, *Grating-coupling of surface plasmons onto metallic tips: A nanoconfined light source*, Nano Lett. **7**, 2784 (2007).
- [85] S. Berweger, J. M. Atkin, R. L. Olmon, and M. B. Raschke, *Adiabatic tip-plasmon focusing for nano-Raman spectroscopy*, J. Phys. Chem. Lett. **1**, 3427 (2010).
- [86] S. Schmidt, B. Piglosiewicz, D. Sadiq, J. Shirdel, J. S. Lee, P. Vasa, N. Park, D.-S. Kim, and C. Lienau, *Adiabatic nanofocusing on ultrasmooth single-crystalline gold tapers creates a 10-nm-sized light source with few-cycle time resolution*, ACS Nano **6**, 6040 (2012).
- [87] V. Sandoghdar, S. Wegscheider, G. Krausch, and J. Mlynek, *Reflection scanning near-field optical microscopy with uncoated fiber tips: How good is the resolution really?*, J. Appl. Phys. **81**, 2499 (1997).
- [88] T. Saiki and K. Matsuda, *Near-field optical fiber probe optimized for illumination-collection hybrid mode operation*, Appl. Phys. Lett. **74**, 2773 (1999).
- [89] A. Kaneta, T. Izumi, K. Okamoto, Y. Kawakami, S. Fujita, Y. Narita, T. Inoue, and T. Mukai, *Spatial inhomogeneity of photoluminescence in an InGaN-based light-emitting diode structure probed by near-field optical microscopy under illumination-collection mode*, Jpn. J. Appl. Phys **40**, 110 (2001).
- [90] D. Courjon and C. Bainier, *Near field microscopy and near field optics*, Rep. Prog. Phys. **57**, 989 (1994).
- [91] E. R. Méndez, J. J. Greffet, and R. Carminati, *On the equivalence between the illumination and collection modes of the scanning near-field optical microscope*, Opt. Commun. **142**, 7 (1997).
- [92] K. Imura and H. Okamoto, *Reciprocity in scanning near-field optical microscopy: illumination and collection modes of transmission measurements*, Opt. Lett. **31**, 1474 (2006).
- [93] O. J. F. Martin, *3D simulations of the experimental signal measured in near-field optical microscopy*, J. Microsc. **194**, 235–239 (1999).
- [94] G. Kaupp, A. Herrmann, and M. Haak, *Artifacts in scanning near-field optical microscopy (SNOM) due to deficient tips*, J. Phys. Org. Chem. **12**, 797–807 (1999).

- [95] J.-J. Greffet and R. Carminati, *Image formation in near-field optics*, Prog. Surf. Sci. **56**, 133 (1997).
- [96] B. Hecht, H. Bielefeldt, Y. Inouye, D. W. Pohl, and L. Novotny, *Facts and artifacts in near-field optical microscopy*, J. Appl. Phys. **81**, 2492 (1997).
- [97] R. L. Williamson, L. J. Brereton, M. Antognozzi, and M. J. Miles, *Are artefacts in scanning near-field optical microscopy related to the misuse of shear force?*, Ultramicroscopy **71**, 165 (1998).
- [98] O. Fenwick, G. Latini, and F. Cacialli, *Modelling topographical artifacts in scanning near-field optical microscopy*, Synth. Met. **147**, 171 (2004).
- [99] D. C. Kohlgraf-Owens, S. Sukhov, and A. Dogariu, *Optical-force-induced artifacts in scanning probe microscopy*, Opt. Lett. **36**, 4758 (2011).
- [100] D. C. Kohlgraf-Owens, S. Sukhov, and A. Dogariu, *Discrimination of field components in optical probe microscopy*, Opt. Lett. **37**, 3606 (2012).
- [101] H. W. Kihm, J. Kim, S. Koo, J. Ahn, K. Ahn, K. Lee, N. Park, and D.-S. Kim, *Optical magnetic field mapping using a subwavelength aperture*, Opt. Express **21**, 5625 (2013).
- [102] P. J. Schuck, A. Weber-Bargioni, P. D. Ashby, D. F. Ogletree, A. Schwartzberg, and S. Cabrini, *Life beyond diffraction: Opening new routes to materials characterization with next-generation optical near-field approaches*, Adv. Funct. Mater. **23**, 2539–2553 (2013).
- [103] D. Ploss, A. Kriesch, H. Pfeifer, P. Banzer, and U. Peschel, *Generation and subwavelength focusing of longitudinal magnetic fields in a metallized fiber tip*, Opt. Express **22**, 13744 (2014).
- [104] A. Teulle, R. Marty, S. Viarbitskaya, A. Arbouet, E. Dujardin, C. Girard, and G. C. des Francs, *Scanning optical microscopy modeling in nanoplasmonics*, J. Opt. Soc. Am. B **29**, 2431 (2012).
- [105] N. Tsumori, M. Takahashi, Y. Sakuma, and T. Saiki, *Experimental study of near-field light collection efficiency of aperture fiber probe at near-infrared wavelengths*, Appl. Opt. **50**, 5710 (2011).
- [106] A. Drezet, M. J. Nasse, S. Huant, and J. C. Woehl, *The optical near-field of an aperture tip*, EPL (Europhysics Letters) **66**, 41 (2004).
- [107] L. Novotny, D. W. Pohl, and P. Regli, *Light propagation through nanometer-sized structures: the two-dimensional-aperture scanning near-field optical microscope*, J. Opt. Soc. Am. A **11**, 1768 (1994).

- [108] S. Schmidt, A. E. Klein, T. Paul, H. Gross, B. N. Tugchin, N. Janunts, S. Diziain, A. da Costa Assafrao, T. Pertsch, H. P. Urbach, and C. Rockstuhl, *Image formation process in aperture based scanning near field optical microscopes*, manuscript in preparation (2014).
- [109] S. Dobmann, A. Kriesch, D. Ploss, and U. Peschel, *Near-field analysis of bright and dark modes on plasmonic metasurfaces showing extraordinary suppressed transmission*, *Advanced Optical Materials* DOI:10.1002/adom.201400237 (2014).
- [110] R. F. Harrington and D. Auckland, *Electromagnetic transmission through narrow slots in thick conducting screens*, *IEEE Transactions on Antennas and Propagation* **28**, 616 (1980).
- [111] O. M. Mendez, M. Cadilhac, and R. Petit, *Diffraction of a two-dimensional electromagnetic beam wave by a thick slit pierced in a perfectly conducting screen*, *J. Opt. Soc. Am.* **73**, 328 (1983).
- [112] A. Drezet, J. C. Woehl, and S. Huant, *Diffraction by a small aperture in conical geometry: Application to metal-coated tips used in near-field scanning optical microscopy*, *Phys. Rev. E* **65**, 046611 (2002).
- [113] T. J. Antosiewicz and T. Szoplik, *Description of near- and far-field light emitted from a metal-coated tapered fiber tip*, *Opt. Express* **15**, 7845 (2007).
- [114] Y. Gorodetski, E. Lombard, A. Drezet, C. Genet, and T. W. Ebbesen, *A perfect plasmonic quarter-wave plate*, *Appl. Phys. Lett.* **101**, 201103 (2012).
- [115] M. Fleischer, *Near-field scanning optical microscopy nanoprobe*, *Nanotechnology Reviews* **1**, 313 (2012).
- [116] N. Mauser and A. Hartschuh, *Tip-enhanced near-field optical microscopy*, *Chem. Soc. Rev.* **43**, 1248 (2014).
- [117] S. Patanè, E. Cefali, S. Spadaro, R. Gardelli, M. Albani, and M. Allegrini, *Polarization-maintaining near-field optical probes*, *J. Microsc.* **229**, 377 (2008).
- [118] P. Venugopalan, Q. Zhang, X. Li, and M. Gu, *Polarization-sensitive characterization of the propagating plasmonic modes in silver nanowire waveguide on a glass substrate with a scanning near-field optical microscope*, *Opt. Express* **21**, 15247 (2013).
- [119] L. Wang and X. Xu, *High transmission nanoscale bowtie-shaped aperture probe for near-field optical imaging*, *Appl. Phys. Lett.* **90**, 261105 (2007).
- [120] M. Mivelle, I. A. Ibrahim, F. Baida, G. W. Burr, D. Nedeljkovic, D. Charraut, J.-Y. Rauch, R. Salut, and T. Grosjean, *Bowtie nano-aperture as interface between near-fields and a single-mode fiber*, *Opt. Express* **18**, 15964 (2010).

- [121] W. Bao, M. Melli, N. Caselli, F. Riboli, D. S. Wiersma, M. Staffaroni, H. Choo, D. F. Ogletree, S. Aloni, J. Bokor, S. Cabrini, F. Intonti, M. B. Salmeron, E. Yablonovitch, P. J. Schuck, and A. Weber-Bargioni, *Mapping local charge recombination heterogeneity by multidimensional nanospectroscopic imaging*, *Science* **338**, 1317 (2012).
- [122] T. Grosjean, M. Mivelle, and G. W. Burr, *Polarization-dependent extraction properties of bare fiber probes*, *Opt. Lett.* **35**, 357 (2010).
- [123] R. Esteban, R. Vogelgesang, J. Dorfmueller, A. Dmitriev, C. Rockstuhl, C. Etrich, and K. Kern, *Direct near-field optical imaging of higher order plasmonic resonances*, *Nano Lett.* **8**, 3155 (2008).
- [124] K. J. Ahn, K. G. Lee, and D. S. Kim, *Effect of dielectric interface on vector field mapping using gold nanoparticles as a local probe: Theory and experiment*, *Opt. Commun.* **281**, 4136 (2008).
- [125] H. W. Kihm, K. G. Lee, D. S. Kim, and K. J. Ahn, *Dual mode near-field scanning optical microscopy for near-field imaging of surface plasmon polariton*, *Opt. Commun.* **282**, 2442 (2009).
- [126] B. le Feber, N. Rotenberg, D. van Oosten, and L. Kuipers, *Modal symmetries at the nanoscale: a route toward a complete vectorial near-field mapping*, *Opt. Lett.* **39**, 2802 (2014).
- [127] E. Devaux, A. Dereux, E. Bourillot, J.-C. Weeber, Y. Lacroute, J.-P. Goudonnet, and C. Girard, *Local detection of the optical magnetic field in the near zone of dielectric samples*, *Phys. Rev. B* **62**, 10504 (2000).
- [128] S. Schmidt, *Image formation mechanism in scanning near field optical microscopy*, Master's thesis, Friedrich-Schiller-Universität Jena, Germany, Faculty of Physics and Astronomy (2013).
- [129] C. Chicanne, T. David, R. Quidant, J. C. Weeber, Y. Lacroute, E. Bourillot, A. Dereux, G. Colas des Francs, and C. Girard, *Imaging the local density of states of optical corrals*, *Phys. Rev. Lett.* **88**, 097402 (2002).
- [130] G. Colas des Francs, C. Girard, J.-C. Weeber, and A. Dereux, *Relationship between scanning near-field optical images and local density of photonic states*, *Chem. Phys. Lett.* **345**, 512 (2001).
- [131] A. Dereux, C. Girard, and J.-C. Weeber, *Theoretical principles of near-field optical microscopies and spectroscopies*, *The Journal of Chemical Physics* **112**, 7775 (2000).
- [132] K. Karrai and R. D. Grober, *Piezoelectric tip-sample distance control for near field optical microscopes*, *Appl. Phys. Lett.* **66**, 1842 (1995).

- [133] A. Lewis, K. Lieberman, N. Ben-Ami, G. Fish, E. Khachatryan, U. Ben-Ami, and S. Shalom, *New design and imaging concepts in NSOM*, *Ultramicroscopy* **61**, 215 (1995).
- [134] D. P. Tsai and Y. Y. Lu, *Tapping-mode tuning fork force sensing for near-field scanning optical microscopy*, *Appl. Phys. Lett.* **73**, 2724 (1998).
- [135] T. Mitsui and T. Sekiguchi, *Observation of polarization property in near-field optical imaging by a polarization-maintaining fiber probe*, *J Electron Microsc (Tokyo)* **53**, 209 (2004).
- [136] T. Grosjean, I. A. Ibrahim, and M. Mivelle, *Multichannel probes for polarization-resolved scanning near-field optical microscopy*, *Appl. Opt.* **49**, 2617 (2010).
- [137] A. Jalocha and N. F. v. Hulst, *Polarization contrast in fluorescence scanning near-field optical reflection microscopy*, *J. Opt. Soc. Am. B* **12**, 1577 (1995).
- [138] T. Mitsui, *Development of a polarization-preserving optical-fiber probe for near-field scanning optical microscopy and the influences of bending and squeezing on the polarization properties*, *Rev. Sci. Instrum.* **76**, 043703 (2005).
- [139] V. P. Adiga, P. W. Kolb, G. T. Evans, M. A. Cubillos-Moraga, D. C. Schmadel, R. Dyott, and H. D. Drew, *Development of high-throughput, polarization-maintaining, near-field probes*, *Appl. Opt.* **45**, 2597 (2006).
- [140] D. H. Dressler, A. Landau, A. Zaban, and Y. Mastai, *Sub-micrometer polarimetry of chiral surfaces using near-field scanning optical microscopy*, *Chem. Commun.* **9**, 945 (2007).
- [141] A. E. Klein, N. Janunts, M. Steinert, A. Tünnermann, and T. Pertsch, *Polarization-resolved near-field mapping of plasmonic aperture emission by a Dual-SNOM system*, *Nano Lett.* **14**, 5010 (2014).
- [142] A. Al-Qasimi, O. Korotkova, D. James, and E. Wolf, *Definitions of the degree of polarization of a light beam*, *Opt. Lett.* **32**, 1015 (2007).
- [143] C. Schulze, A. Lorenz, D. Flamm, A. Hartung, S. Schröter, H. Bartelt, and M. Duparré, *Mode resolved bend loss in few-mode optical fibers*, *Opt. Express* **21**, 3170 (2013).
- [144] Q. Wang, G. Rajan, P. Wang, and G. Farrell, *Polarization dependence of bend loss for a standard singlemode fiber*, *Opt. Express* **15**, 4909 (2007).
- [145] H. Yu, S. Wang, J. Fu, M. Qiu, Y. Li, F. Gu, and L. Tong, *Modeling bending losses of optical nanofibers or nanowires*, *Appl. Opt.* **48**, 4365 (2009).
- [146] M. Miyagi and G. L. Yip, *Field deformation and polarization change in a step-index optical fibre due to bending*, *Opt. Quantum. Electron.* **8**, 335 (1976).

- [147] P. Biagioni, D. Polli, M. Labardi, A. Pucci, G. Ruggeri, G. Cerullo, M. Finazzi, and L. Duò, *Unexpected polarization behavior at the aperture of hollow-pyramid near-field probes*, Appl. Phys. Lett. **87**, 223112 (2005).
- [148] R. L. Olmon, B. Slovick, T. W. Johnson, D. Shelton, S.-H. Oh, G. D. Boreman, and M. B. Raschke, *Optical dielectric function of gold*, Phys. Rev. B **86**, 235147 (2012).
- [149] B. Hecht, H. Bielefeldt, L. Novotny, Y. Inouye, and D. W. Pohl, *Local excitation, scattering, and interference of surface plasmons*, Phys. Rev. Lett. **77**, 1889 (1996).
- [150] N. Rotenberg, M. Spasenović, T. L. Krijger, B. le Feber, F. J. García de Abajo, and L. Kuipers, *Plasmon scattering from single subwavelength holes*, Phys. Rev. Lett. **108**, 127402 (2012).
- [151] A. E. Klein, C. Schmidt, M. Liebsch, N. Janunts, M. Dobynde, A. Tünnermann, and T. Pertsch, *Highly sensitive mode mapping of whispering-gallery modes by scanning thermocouple-probe microscopy*, Opt. Lett. **39**, 1157 (2014).
- [152] J. Kohoutek, D. Dey, A. Bonakdar, R. Gelfand, A. Sklar, O. G. Memis, and H. Mohseni, *Opto-mechanical force mapping of deep subwavelength plasmonic modes*, Nano Lett. **11**, 3378 (2011).
- [153] D. C. Kohlgraf-Owens, S. Sukhov, and A. Dogariu, *Mapping the mechanical action of light*, Phys. Rev. A **84**, 011807 (2011).
- [154] M. S. Dunaevskiy, P. A. Alekseev, A. N. Baranov, A. M. Monakhov, R. Teissier, R. Arinero, P. Girard, and A. N. Titkov, *Near field imaging of a semiconductor laser by scanning probe microscopy without a photodetector*, Appl. Phys. Lett. **103**, 053120 (2013).
- [155] P. G. Datskos, N. V. Lavrik, and S. Rajic, *Performance of uncooled microcantilever thermal detectors*, Rev. Sci. Instrum. **75**, 1134 (2004).
- [156] J.-M. Ortega, F. Glotin, R. Prazeres, J.-P. Berthet, and A. Dazzi, *Detection of pulsed far-infrared and terahertz light with an atomic force microscope*, Appl. Phys. Lett. **101**, 141117 (2012).
- [157] G. Fish, O. Bouevitch, S. Kokotov, K. Lieberman, D. Palanker, I. Turovets, and A. Lewis, *Ultrafast response micropipette-based submicrometer thermocouple*, Rev. Sci. Instrum. **66**, 3300 (1995).
- [158] N. W. Ashcroft and N. D. Mermin, *Solid State Physics*, Saunders College, Philadelphia (1976).
- [159] C. Maetzler, *MATLAB Functions for Mie Scattering and Absorption, Version 2*, IAP Research Reports 199, University of Bern, Institute of Applied Physics, Bern, Switzerland (2002).

- [160] C. Bohren and D. R. Huffman, *Absorption and Scattering of Light by Small Particles*, John Wiley & Sons, New York (1983).
- [161] E. D. Palik (editor), *Handbook of Optical Constants of Solids*, vol. 3, Academic press, Orlando (1998).
- [162] S. A. Maier, P. G. Kik, H. A. Atwater, S. Meltzer, E. Harel, B. E. Koel, and A. A. Requicha, *Local detection of electromagnetic energy transport below the diffraction limit in metal nanoparticle plasmon waveguides*, Nat. Mater. **2**, 229 (2003).
- [163] K. Joulain, R. Carminati, J.-P. Mulet, and J.-J. Greffet, *Definition and measurement of the local density of electromagnetic states close to an interface*, Phys. Rev. B **68**, 245405 (2003).
- [164] J.-C. Weeber, Y. Lacroute, and A. Dereux, *Optical near-field distributions of surface plasmon waveguide modes*, Phys. Rev. B **68**, 115401 (2003).
- [165] R. Zia, J. A. Schuller, and M. L. Brongersma, *Near-field characterization of guided polariton propagation and cutoff in surface plasmon waveguides*, Phys. Rev. B **74**, 165415 (2006).
- [166] E. Verhagen, A. Polman, L. Kuipers et al., *Nanofocusing in laterally tapered plasmonic waveguides*, Opt. Express **16**, 45 (2008).
- [167] J. Berthelot, F. Tantussi, P. Rai, G. C. des Francs, J.-C. Weeber, A. Dereux, F. Fuso, M. Allegrini, and A. Bouhelier, *Determinant role of the edges in defining surface plasmon propagation in stripe waveguides and tapered concentrators*, J. Opt. Soc. Am. B **29**, 226 (2012).
- [168] R. Dallapiccola, C. Dubois, A. Gopinath, F. Stellacci, and L. D. Negro, *Near-field excitation and near-field detection of propagating surface plasmon polaritons on au waveguide structures*, Appl. Phys. Lett. **94**, 243118 (2009).
- [169] X. Ren, A. Liu, C. Zou, L. Wang, Y. Cai, F. Sun, G. Guo, and G. Guo, *Interference of surface plasmon polaritons from a "point" source*, Appl. Phys. Lett. **98**, 201113 (2011).
- [170] R. Fujimoto, A. Kaneta, K. Okamoto, M. Funato, and Y. Kawakami, *Interference of the surface plasmon polaritons with an ag waveguide probed by dual-probe scanning near-field optical microscopy*, Appl. Surf. Sci. **258**, 7372 (2012).
- [171] A. Kaneta, T. Hashimoto, K. Nishimura, M. Funato, and Y. Kawakami, *Visualization of the local carrier dynamics in an InGaN quantum well using dual-probe scanning near-field optical microscopy*, Appl. Phys. Express **3**, 102102 (2010).

- [172] A. Kaneta, R. Fujimoto, T. Hashimoto, K. Nishimura, M. Funato, and Y. Kawakami, *Instrumentation for dual-probe scanning near-field optical microscopy*, Rev. Sci. Instrum. **83**, 083709 (2012).
- [173] D. K. Gramotnev and S. I. Bozhevolnyi, *Nanofocusing of electromagnetic radiation*, Nat. Photonics **8**, 13 (2014).
- [174] A. G. T. Ruiter, J. A. Veerman, K. O. van der Werf, and N. F. van Hulst, *Dynamic behavior of tuning fork shear-force feedback*, Appl. Phys. Lett. **71**, 28 (1997).
- [175] A. E. Klein, N. Janunts, A. Tünnermann, and T. Pertsch, *Investigation of mechanical interactions between the tips of two scanning near-field optical microscopes*, Appl. Phys. B **108**, 737 (2012).
- [176] J. C. Gutiérrez-Vega, M. D. Iturbe-Castillo, and S. Chávez-Cerda, *Alternative formulation for invariant optical fields: Mathieu beams*, Opt. Lett. **25**, 1493 (2000).
- [177] J. Durnin, *Exact solutions for nondiffracting beams. I. The scalar theory*, J. Opt. Soc. Am. A **4**, 651 (1987).
- [178] J. Durnin, J. J. Miceli, and J. H. Eberly, *Diffraction-free beams*, Phys. Rev. Lett. **58**, 1499 (1987).
- [179] Z. Chen, M. Segev, and D. N. Christodoulides, *Optical spatial solitons: historical overview and recent advances*, Rep. Prog. Phys. **75**, 086401 (2012).
- [180] M. Mazilu, D. Stevenson, F. Gunn-Moore, and K. Dholakia, *Light beats the spread: "non-diffracting" beams*, Laser & Photon. Rev. **4**, 529 (2010).
- [181] P. Aleahmad, M.-A. Miri, M. S. Mills, I. Kaminer, M. Segev, and D. N. Christodoulides, *Fully vectorial accelerating diffraction-free helmholtz beams*, Phys. Rev. Lett. **109**, 203902 (2012).
- [182] G. A. Siviloglou and D. N. Christodoulides, *Accelerating finite energy Airy beams*, Opt. Lett. **32**, 979 (2007).
- [183] G. A. Siviloglou, J. Broky, A. Dogariu, and D. N. Christodoulides, *Observation of accelerating Airy beams*, Phys. Rev. Lett. **99**, 213901 (2007).
- [184] E. Greenfield, M. Segev, W. Walasik, and O. Raz, *Accelerating light beams along arbitrary convex trajectories*, Phys. Rev. Lett. **106**, 213902 (2011).
- [185] I. Kaminer, R. Bekenstein, J. Nemirovsky, and M. Segev, *Nondiffracting accelerating wave packets of Maxwell's equations*, Phys. Rev. Lett. **108**, 163901 (2012).
- [186] P. Zhang, Y. Hu, T. Li, D. Cannan, X. Yin, R. Morandotti, Z. Chen, and X. Zhang, *Nonparaxial Mathieu and Weber accelerating beams*, Phys. Rev. Lett. **109**, 193901 (2012).

- [187] A. Salandrino and D. N. Christodoulides, *Airy plasmon: A nondiffracting surface wave*, Opt. Lett. **35**, 2082 (2010).
- [188] M. V. Berry and N. L. Balazs, *Nonspreading wave packets*, Am. J. Phys. **47**, 264 (1979).
- [189] A. Minovich, A. E. Klein, N. Janunts, T. Pertsch, D. N. Neshev, and Y. S. Kivshar, *Generation and near-field imaging of Airy surface plasmons*, Phys. Rev. Lett. **107**, 116802 (2011).
- [190] L. Li, T. Li, S. M. Wang, C. Zhang, and S. N. Zhu, *Plasmonic Airy beam generated by in-plane diffraction*, Phys. Rev. Lett. **107**, 126804 (2011).
- [191] P. Zhang, S. Wang, Y. Liu, X. Yin, C. Lu, Z. Chen, and X. Zhang, *Plasmonic Airy beams with dynamically controlled trajectories*, Opt. Lett. **36**, 3191 (2011).
- [192] A. E. Klein, A. Minovich, M. Steinert, N. Janunts, A. Tünnermann, D. N. Neshev, Y. S. Kivshar, and T. Pertsch, *Controlling plasmonic hot spots by interfering Airy beams*, Opt. Lett. **37**, 3402 (2012).
- [193] A. Minovich, A. E. Klein, D. N. Neshev, T. Pertsch, Y. S. Kivshar, and D. N. Christodoulides, *Airy plasmons: non-diffracting optical surface waves*, Laser & Photonics Reviews **8**, 221 (2014).
- [194] L. Li, T. Li, S. M. Wang, and S. N. Zhu, *Collimated plasmon beam: Nondiffracting versus linearly focused*, Phys. Rev. Lett. **110**, 046807 (2013).
- [195] J. Lin, J. Dellinger, P. Genevet, B. Cluzel, F. de Fornel, and F. Capasso, *Cosine-Gauss plasmon beam: A localized long-range nondiffracting surface wave*, Phys. Rev. Lett. **109**, 093904 (2012).
- [196] C. J. Regan, L. G. d. Peralta, and A. A. Bernussi, *Two-dimensional Bessel-like surface plasmon-polariton beams*, J. Appl. Phys. **112**, 103107 (2012).
- [197] E. Kretschmann and H. Raether, *Radiative decay of nonradiative surface plasmons excited by light*, Z. Naturforsch. A **23**, 2135 (1968).
- [198] A. Otto, *Excitation of nonradiative surface plasma waves in silver by the method of frustrated total reflection*, Z. Physik **216**, 398 (1968).
- [199] R. H. Ritchie, E. T. Arakawa, J. J. Cowan, and R. N. Hamm, *Surface-plasmon resonance effect in grating diffraction*, Phys. Rev. Lett. **21**, 1530 (1968).
- [200] A. V. Novitsky and D. V. Novitsky, *Nonparaxial Airy beams: role of evanescent waves*, Opt. Lett. **34**, 3430 (2009).

- [201] W. Liu, D. N. Neshev, I. V. Shadrivov, A. E. Miroshnichenko, and Y. S. Kivshar, *Plasmonic Airy beam manipulation in linear optical potentials*, Opt. Lett. **36**, 1164 (2011).
- [202] F. Bleckmann, A. Minovich, J. Frohnhaus, D. N. Neshev, and S. Linden, *Manipulation of Airy surface plasmon beams*, Opt. Lett. **38**, 1443 (2013).
- [203] A. Mathis, F. Courvoisier, L. Froehly, L. Furfaro, M. Jacquot, P. A. Lacourt, and J. M. Dudley, *Micromachining along a curve: Femtosecond laser micromachining of curved profiles in diamond and silicon using accelerating beams*, Appl. Phys. Lett. **101**, 071110 (2012).
- [204] J. Baumgartl, M. Mazilu, and K. Dholakia, *Optically mediated particle clearing using Airy wavepackets*, Nat. Photonics **2**, 675 (2008).
- [205] P. Zhang, J. Prakash, Z. Zhang, M. S. Mills, N. K. Efremidis, D. N. Christodoulides, and Z. Chen, *Trapping and guiding microparticles with morphing autofocusing Airy beams*, Opt. Lett. **36**, 2883 (2011).
- [206] N. K. Efremidis and D. N. Christodoulides, *Abruptly autofocusing waves*, Opt. Lett. **35**, 4045 (2010).
- [207] D. G. Papazoglou, N. K. Efremidis, D. N. Christodoulides, and S. Tzortzakis, *Observation of abruptly autofocusing waves*, Opt. Lett. **36**, 1842 (2011).
- [208] M. Righini, A. Zelenina, C. Girard, and R. Quidant, *Parallel and selective trapping in a patterned plasmonic landscape*, Nat. Phys. **3**, 477 (2007).
- [209] T. S. Kao, S. D. Jenkins, J. Ruostekoski, and N. I. Zheludev, *Coherent control of nanoscale light localization in metamaterial: Creating and positioning isolated subwavelength energy hot spots*, Phys. Rev. Lett. **106**, 085501 (2011).
- [210] B. Gjonaj, J. Aulbach, P. M. Johnson, A. P. Mosk, L. Kuipers, and A. Lagendijk, *Active spatial control of plasmonic fields*, Nat. Photonics **5**, 360 (2011).
- [211] B. Gjonaj, J. Aulbach, P. M. Johnson, A. P. Mosk, L. Kuipers, and A. Lagendijk, *Focusing and scanning microscopy with propagating surface plasmons*, Phys. Rev. Lett. **110**, 266804 (2013).
- [212] K. J. Vahala, *Optical microcavities*, Nature **424**, 839 (2003).
- [213] J. Ward and O. Benson, *WGM microresonators: sensing, lasing and fundamental optics with microspheres*, Laser & Photonics Reviews **5**, 553 (2011).
- [214] A. Chiasera, Y. Dumeige, P. Féron, M. Ferrari, Y. Jestin, G. Nunzi Conti, S. Pelli, S. Soria, and G. Righini, *Spherical whispering-gallery-mode microresonators*, Laser & Photonics Reviews **4**, 457 (2010).

- [215] M. Himmelhaus and A. Francois, *In-vitro sensing of biomechanical forces in live cells by a whispering gallery mode biosensor*, *Biosensors and Bioelectronics* **25**, 418 (2009).
- [216] M. Charlebois, A. Paquet, L. S. Verret, K. Boissinot, M. Boissinot, M. G. Bergeron, and C. N. Allen, *Toward automatic label-free whispering gallery modes biodetection with a quantum dot-coated microsphere population*, *Nanoscale Res. Lett.* **5**, 524 (2010).
- [217] V. Michaud-Belleau, J. Roy, S. Potvin, J.-R. Carrier, L.-S. Verret, M. Charlebois, J. Genest, and C. N. Allen, *Whispering gallery mode sensing with a dual frequency comb probe*, *Opt. Express* **20**, 3066 (2012).
- [218] D. W. Vernooy, A. Furusawa, N. P. Georgiades, V. S. Ilchenko, and H. J. Kimble, *Cavity QED with high-Q whispering gallery modes*, *Phys. Rev. A* **57**, R2293 (1998).
- [219] W. von Klitzing, R. Long, V. S. Ilchenko, J. Hare, and V. Lefèvre-Seguin, *Frequency tuning of the whispering-gallery modes of silica microspheres for cavity quantum electrodynamics and spectroscopy*, *Opt. Lett.* **26**, 166 (2001).
- [220] Y. Louyer, D. Meschede, and A. Rauschenbeutel, *Tunable whispering-gallery-mode resonators for cavity quantum electrodynamics*, *Phys. Rev. A* **72**, 031801 (2005).
- [221] D. O'Shea, C. Junge, M. Pöllinger, A. Vogler, and A. Rauschenbeutel, *All-optical switching and strong coupling using tunable whispering-gallery-mode microresonators*, *Appl. Phys. B* **105**, 129 (2011).
- [222] S. L. McCall, A. F. J. Levi, R. E. Slusher, S. J. Pearton, and R. A. Logan, *Whispering-gallery mode microdisk lasers*, *Appl. Phys. Lett.* **60**, 289 (1992).
- [223] L. He, a. K. Özdemir, J. Zhu, W. Kim, and L. Yang, *Detecting single viruses and nanoparticles using whispering gallery microlasers*, *Nat. Nanotechnol.* **6**, 428 (2011).
- [224] Q. J. Wang, C. Yan, N. Yu, J. Unterhinninghofen, J. Wiersig, C. Pflügl, L. Diehl, T. Edamura, M. Yamanishi, H. Kan, and F. Capasso, *Whispering-gallery mode resonators for highly unidirectional laser action*, *Proceedings of the National Academy of Sciences* **107**, 22407 (2010).
- [225] T. J. Kippenberg, R. Holzwarth, and S. A. Diddams, *Microresonator-based optical frequency combs*, *Science* **332**, 555 (2011).
- [226] V. S. Ilchenko, A. S. Savchenkov, W. Liang, A. Matsko, J. Byrd, D. Eliyahu, D. Seidel, and L. Maleki, *Optical combs and photonic RF oscillators with whispering-gallery mode microresonators*, in *Frontiers in Optics 2011/Laser Science XXVII*, OSA Technical Digest, p. FThW5, Optical Society of America (2011).
- [227] C. Schmidt, A. Chipouline, T. Käsebier, E.-B. Kley, A. Tünnermann, T. Pertsch, V. Shuvayev, and L. I. Deych, *Observation of optical coupling in microdisk resonators*, *Phys. Rev. A* **80**, 043841 (2009).

- [228] T. Carmon, H. G. L. Schwefel, L. Yang, M. Oxborrow, A. D. Stone, and K. J. Vahala, *Static envelope patterns in composite resonances generated by level crossing in optical toroidal microcavities*, Phys. Rev. Lett. **100**, 103905 (2008).
- [229] C. Schmidt, *Mode dynamics in coupled disk optical microresonators*, Ph.D. thesis, Friedrich-Schiller-Universität Jena (2013).
- [230] C. Schmidt, M. Liebsch, A. Klein, N. Janunts, A. Chipouline, T. Käsebier, C. Etrich, F. Lederer, E.-B. Kley, A. Tünnermann, and T. Pertsch, *Near-field mapping of optical eigenstates in coupled disk microresonators*, Phys. Rev. A **85**, 033827 (2012).
- [231] J. C. Knight, N. Dubreuil, V. Sandoghdar, J. Hare, V. Lefèvre-Seguin, J. M. Raimond, and S. Haroche, *Mapping whispering-gallery modes in microspheres with a near-field probe*, Opt. Lett. **20**, 1515 (1995).
- [232] M. L. M. Balistreri, D. W. Klunder, F. C. Blom, A. Driessen, H. W. J. M. Hoekstra, J. P. Korterik, L. Kuipers, and N. F. van Hulst, *Visualizing the whispering gallery modes in a cylindrical optical microcavity*, Opt. Lett. **24**, 1829 (1999).
- [233] S. Götzinger, S. Demmerer, O. Benson, and V. Sandoghdar, *Mapping and manipulating whispering gallery modes of a microsphere resonator with a near-field probe*, J. Microsc. **202**, 117 (2001).
- [234] S. Blaize, F. Gesuele, I. Stefanon, A. Bruyant, G. Léron del, P. Royer, B. Martin, A. Morand, P. Benech, and J.-M. Fedeli, *Real-space observation of spectral degeneracy breaking in a waveguide-coupled disk microresonator*, Opt. Lett. **35**, 3168 (2010).
- [235] J. Knight, G. Cheung, F. Jacques, and T. Birks, *Phase-matched excitation of whispering-gallery-mode resonances by a fiber taper*, Opt. Lett. **22**, 1129 (1997).
- [236] J. T. Robinson, S. F. Preble, and M. Lipson, *Imaging highly confined modes in sub-micron scale silicon waveguides using transmission-based near-field scanning optical microscopy*, Opt. Express **14**, 10588 (2006).
- [237] W. C. L. Hopman, K. O. van der Werf, A. J. F. Hollink, W. Bogaerts, V. Subramaniam, and R. M. de Ridder, *Nano-mechanical tuning and imaging of a photonic crystal micro-cavity resonance*, Opt. Express **14**, 8745 (2006).
- [238] D. C. Kohlgraf-Owens, S. Sukhov, L. Greusard, Y. De Wilde, and A. Dogariu, *Optically induced forces in scanning probe microscopy*, Nanophotonics **3**, 105–116 (2014).
- [239] C. Schmidt, A. Chipouline, T. Käsebier, E.-B. Kley, A. Tünnermann, and T. Pertsch, *Temperature induced nonlinearity in coupled microresonators*, Appl. Phys. B **104**, 503 (2011).

- [240] S. Bozhevolnyi (editor), *Plasmonic Nanoguides and Circuits*, Pan Stanford Publishing, Singapore (2009).
- [241] Z. Han and S. I. Bozhevolnyi, *Radiation guiding with surface plasmon polaritons*, Rep. Prog. Phys. **76**, 016402 (2013).
- [242] C. Rewitz, G. Razinskas, P. Geisler, E. Krauss, S. Goetz, M. Pawłowska, B. Hecht, and T. Brixner, *Coherent control of plasmon propagation in a nanocircuit*, Physical Review Applied **1**, 014007 (2014).
- [243] F. Liu, R. Wan, Y. Li, Y. Huang, Y. Miura, D. Ohnishi, and J. Peng, *Extremely high efficient coupling between long range surface plasmon polariton and dielectric waveguide mode*, Appl. Phys. Lett. **95**, 091104 (2009).
- [244] R. M. Briggs, J. Grandidier, S. P. Burgos, E. Feigenbaum, and H. A. Atwater, *Efficient coupling between dielectric-loaded plasmonic and silicon photonic waveguides*, Nano Lett. **10**, 4851 (2010).
- [245] J. R. Krenn and J.-C. Weeber, *Surface plasmon polaritons in metal stripes and wires.*, Philos. T. Roy. Soc. A **362**, 739 (2004).
- [246] R. F. Service, *Ever-smaller lasers pave the way for data highways made of light*, Science **328**, 810 (2010).
- [247] M. Khajavikhan, A. Simic, M. Katz, J. H. Lee, B. Slutsky, A. Mizrahi, V. Lomakin, and Y. Fainman, *Thresholdless nanoscale coaxial lasers*, Nature **482**, 204 (2012).
- [248] R. Zia, M. D. Selker, and M. L. Brongersma, *Leaky and bound modes of surface plasmon waveguides*, Phys. Rev. B **71**, 165431 (2005).
- [249] H. Taha, R. S. Marks, L. A. Gheber, I. Rousso, J. Newman, C. Sukenik, and A. Lewis, *Protein printing with an atomic force sensing nanofountainpen*, Appl. Phys. Lett. **83**, 1041 (2003).
- [250] H. Taha, A. Lewis, and C. Sukenik, *Controlled deposition of gold nanowires on semiconducting and nonconducting surfaces*, Nano Lett. **7**, 1883 (2007).
- [251] M. Sokuler and L. A. Gheber, *Nano fountain pen manufacture of polymer lenses for nano-biochip applications*, Nano Lett. **6**, 848 (2006).
- [252] J. Berthelot, S. S. Aćimović, M. L. Juan, M. P. Kreuzer, J. Renger, and R. Quidant, *Three-dimensional manipulation with scanning near-field optical nanotweezers*, Nat. Nanotechnol. **9**, 295 (2014).